Physics Theses & Dissertations

Physics

Winter 2000

Experimental Investigation of Long-Lived "ZEKE" Rydberg States in Ultracold Argon

Gambhir Ranjit
Old Dominion University

EXPERIMENTAL INVESTIGATION OF LONG-LIVED "ZEKE" RYDBERG STATES IN ULTRACOLD ARGON

by

Gambhir Ranjit
B.Sc. 1998, Tri-chandra College, Nepal
M.Sc. Physics, 2000, Tribhuvan University, Nepal
M.S. Physics, May 2006, Old Dominion University

A Dissertation Submitted to the Faculty of
Old Dominion University in Partial Fulfillment of the
Requirement for the Degree of

DOCTOR OF PHILOSOPHY

PHYSICS

OLD DOMINION UNIVERSITY
December 2010

Approved by:

Charles I. Sukenik (Director)

Leposava Vuskovic (Member)

Ian Balitsky (Member)

Alex Godunov (Member)

Kenneth Brown (Member)

ABSTRACT

EXPERIMENTAL INVESTIGATION OF LONG-LIVED "ZEKE" RYDBERG STATES IN ULTRACOLD ARGON

Gambhir Ranjit

Old Dominion University, 2010

Director: Dr. Charles I. Sukenik

There is considerable interest in the dynamics of ultracold plasmas and ultracold Rydberg gases. Ultracold plasmas are typically formed by photo-excitation of ultracold atoms to an energy region near (both above and below) an ionization threshold. Excitation to bound, highly-excited Rydberg states can lead to formation of a plasma via several processes, including collisions between Rydberg atoms. Three-body recombination in an ultracold plasma can also result in the production of ultracold Rydberg atoms. Understanding the dynamics of ultracold Rydberg gases is therefore important for understanding the dynamics of ultracold plasmas. In this dissertation, we have investigated the formation and survival of a particular class of Rydberg atoms. These atoms are known as ZEKE state Rydberg atoms, where the term ZEKE is derived from "Zero Kinetic Energy." ZEKE Rydberg states are high angular momentum and high angular momentum projection excited states which can be formed by laser excitation in the presence of electric fields. Without the electric fields, these states would be optically dark. We have investigated ZEKE Rydberg states in ultracold argon in an energy region just below the second ionization threshold of the atoms in our magneto-optical trap. Here, low angular momentum states decay very quickly (< 1 ns) by auto-ionization through a core spin flip due to the Rydberg electron-core interaction. This interaction has been significantly reduced due to the dilution of low l and m states as a result of l and m mixing during excitation. Hence, ZEKE Rydberg states live orders of magnitude longer than low angular momentum states. We are reporting on our experimental investigation of these states in the ultracold regime and prospects for future studies in which external control of these states may be used to control ultracold plasma dynamics.

iii

To my parents and my wife...

ACKNOWLEDGEMENTS

I would like to thank my advisor Dr. Charles. I. Sukenik for believing in me and giving me the opportunity to work in his AMO research group despite my having null previous experimental background. This work is not possible without his profound experimental and theoretical expertise in the field of atomic physics. I am very much impressed with his sense of humor all the time, including during difficult situations in the lab, to keep our motivation high and the lab-atmosphere lively. His true guidance and knowledge has provided me with an education not limited to the field of atomic physics. I deeply admire his patience and moral support.

I would like to thank my dissertation committee members: Dr. Leposava Vuskovic, Dr. Ian Balitsky, Dr. Alex Godunov and Dr. Kenneth Brown. I would like to acknowledge Dr. Svetozar Popovic for the friendly and helpful discussions on the results and the analysis.

I would like to thank Dr. Gail Dodge for her support and kind advice all the time. I really appreciated the late Bob Evans for being such a good friend and providing support in the teaching labs. Also, I would like to thank Annette Guzman-Smith and Delicia Malin for their assistance during my studentship at ODU.

I am really indebted to Dr. Mike K. Shaffer for being a senior lab member and imparting his experimental knowledge and excellence to make things work in the lab. I will always be thankful to Dr. Eman Ahmed for being such a wonderful friend who made me believe "where there is a will there is a way," Great job, Eman. I would like to thank Dr. Hauke C. Busch for helping me build the detector and accelerate my research project. My thanks extend to Ivan Koralt for his contribution in making the commercial dye laser circulator unit work.

And, I would like to thank Maha Khaled Omar for helping me with the alignment and installation of the ion optics in the science chamber, and tolerating my frequent mood swings depending upon the mood swings of my apparatus in the lab. I want to thank Jack Mills for helping me every possible way and for providing computational software for data analysis.

I would also like to thank Saori Pastore for being the best friend in spite of us having so many differences. And, I would like to thank Michael Mayer, Bill Ford, Aye Lu Win and Raja for always being there whenever I am in need of any help. And, I would like to thank Krishna Prasad Adhikari, Meghraj Niroula, Suman Koirala for

being good friends in and out of the department and I would like to acknowledge Marija Raskovic, Jan Drake, Steven Wild, Mladen Dordevic Donika Plyku, Dr. Rocio Olave and Dr. Salim Balik for their continuous friendship.

I would like to specially thank Mr. Walton Hooks and the late Vickie Hooks for such friendly treatment to make me and my wife, Ramina feel like being at home all the time. You will always remain in my heart, Vickie.

Finally, I would like to thank Jefferson Lab for the support during my research and I would like to acknowledge Dr. Swapan Chattopadhyay and Dr. Gwen Williams for being my mentors at Jefferson Lab.

TABLE OF CONTENTS

LIST OF TABLES

LIST OF FIGURES

CHAPTER I

INTRODUCTION

The realization of the first magneto-optical trap (MOT), combining the underlying theory of laser cooling and trapping in the presence of a magnetic field enabled significant advances in modern spectroscopy [1], frequency standards, and the experimental verification of Bose-Einstein Condensation (BEC) [2]. The manipulation of atoms [3] plays an important role in the development of many aspects of atom-optics experiments.

The idea of manipulation of atoms using light forces was first conceived in 1975 by Hänsh and Schawlow [4]. In 1976, the idea was demonstrated by Letokhov, Minogin and Pavlik[5]. In 1985, Phillips *et al.* trapped atoms in a magnetic trap [6] while Chu *et al.* trapped atoms in a focused laser beam [7] as proposed by Ashkin [8] in 1978. It took several years to realize Bose-Einstein Condensation, which was made possible by using the method of evaporative cooling. In 1995, Eric Cornell, Carl Wieman and co-workers at JILA produced a rubidium BEC [2]. In the mean time, Wolfgang Ketterle and co workers at MIT made the first sodium BEC in a magnetic trap [9]. Consequently, they were awarded the Nobel Prize in 2001 for their achievements.

In the last decade, other applications have found prominence in the field of ultracold atomic and molecular physics. For example, one area of considerable interest is in the production of ultracold molecules. This can now be done either by starting with warm molecules and cooling them or by starting with cold atoms and assembling them into a cold molecule. Another area of growing interest is ultracold plasmas and ultracold Rydberg gases. Plasmas are macroscopically neutral systems of fully or partially ionized gas which consist of ions and free electrons bound together by long range Coulomb forces. The formation of conventional plasmas is usually due to collisions between high-energy particles, and hence they are fairly hot, ranging in temperature from 10^{16} K in the magnetosphere of a pulsar to 300 K in the earth's ionosphere. These two entities "ultracold gas" and "plasma" were combined to expand the frontiers of atomic physics for the first time in 1999 at NIST by Steven Rolston and co-workers to form the first ultracold plasma (UCP) [10]. Because these plasmas are usually quasi-neutral, they are sometimes known as ultracold neutral plasma (UCNP). UCPs are formed by photo-ionizing ultracold atoms in a MOT. The first

UCP was achieved in a xenon MOT [10]. Ultracold plasmas are now routinely formed by photoionization of ultracold atoms (a few milli-Kelvin temperatures or less) near the ionization threshold, typically using nanoseconds pulsed dye lasers. Once formed, the plasma exhibits a rich set of dynamics including electron-ion recombination. The various dynamical events ranging from the thermalization of the plasma components to the expansion under electron pressure and complete disappearance of the plasma have been investigated. These processes typically take place within a few hundred microseconds following the plasma creation. The thermal energies of the plasma components are strongly dependent on the excess energy $\Delta E = h\nu - I_p$, the difference between the energy of the photo-ionizing photon ($h\nu$) and the ionization potential, I_p. In theory, one could tune a laser to be right at the ionization limit; in practice, the finite linewidth of the pulsed laser limits how close to the zero thermal energy mark one can achieve. Due to the very small mass ratio of electrons to ions, the electrons carry away most of the excess energy. The temperature of the electrons can be tuned by adjusting the laser frequency, while ions have a tendency to remain near the temperature of the ultracold neutral atoms. The plasma is characterized by the Coulomb coupling parameter given by [10]

$$\Gamma_\alpha = \frac{e^2}{4\pi\epsilon_0 a} \frac{1}{K_B T_\alpha} \tag{1}$$

where $a = (4\pi n/3)^{-1/3}$ is the Wigner-Seitz radius, n is the density, T is the temperature and α denotes the electron or ion. Plasmas, in general, span a very large phase space of temperatures and densities. If $\Gamma > 1$, the plasma becomes strongly coupled as the Coulomb interaction energy among charged particle exceeds the thermal energy. Hence, it provides a test bed for the study of strongly coupled plasmas like those presumably found in Jovian planets and white dwarfs. Until recently, most plasmas studied in the lab have been far from the strong coupling regime. For very high Γ there occurs an ordering effect of Coulomb crystallization [11]. However, there always exists some heating mechanism. The disordered induced heating (DIH) of ions that takes place on the timescale of the inverse of the ionic plasma frequency $\omega^{-1} = \sqrt{m_i/4\pi e^2 n_i}$ decreases the degree of correlation in the plasma [12]. The energetic electrons leave the plasma cloud creating a charge imbalance with net positive charge. The remaining electrons are trapped in the ionic potential well. The resulting quasi-neutral plasma then expands under the electron pressure explained by a hydrodynamic model [13]. There occurs a rapid expansion at the low energies and high

densities which are attributed to the presence of the three-body collision involving an ion and two electrons resulting in "three-body recombination" [14, 15, 16] in which the ion and one of the electrons recombine to form a highly excited Rydberg atom. The binding energy of the Rydberg electron is carried by the second electron. This excess energy serves to drive and expansion of the plasma faster, since the electronic cloud exerts an outward pressure on the ionic cloud. The three-body recombination rate scales as the square of the electron density n_e^2 due to the involvement of two electrons in the collision process and also scales as $T^{-9/2}$ where, T is the electron temperature.

The plasma expands at the expense of the oscillating electrons, cooling them adiabatically and the three-body mechanism drops [14] as the plasma expands and the density decreases. Rydberg atoms formed can undergo spontaneous evolution into an ultracold plasma due to the ionizing collisions between hot and cold Rydberg atoms, blackbody photoionization and the collision between the electrons and the Rydberg atoms [17]. Hence, the system of an ultracold gas can evolve back and forth between Rydberg atoms and and an ultracold plasma [18].

Rydberg atoms are highly excited atoms with one electron weekly bound with relatively high principal quantum number $n >> 1$. These Rydberg atoms have exaggerated properties; in particular their long lifetime, which scales as n^3, their susceptibility to external fields due to their size (the radius of charge distribution of the Rydberg electron) which scales as n^2 and large geometrical and collision cross-section that scales as n^4. These have been investigated in great detail [19]. Interest in these atoms has been renewed following the technique of laser cooling and trapping. One of the major interests is the study of electric multipole (dipole-dipole) interaction of Rydberg atoms that influences the dynamics of excitation of a Rydberg gas system, also known as dipole blockade which provides the basis for a quantum computing scheme [20, 21, 22].

Under certain conditions, the non-ionizing interactions also induce state-mixing collisions in cold Rydberg gases which governs the evolution of the cold Rydberg atoms into long-lived states [23]. The underlying phenomena for such evolution into long-lived states have been identified as the l and m -changing collisions between the free electrons or ions and the low l and m-Rydberg atoms [24]. Such long-lived states are not restricted to cold atoms, though. These long-lived states are called Zero Kinetic Energy or ZEKE states, the term derived from ZEKE spectroscopy. ZEKE

spectroscopy is the high resolution spectroscopy which is a successive development of Threshold photoelectron spectroscopy (TPES), and relies only on the electrons or ions produced through delayed pulsed field ionization to get rid of the hot electrons or ions. The resolution is only limited by the bandwidth of the excitation lasers [25, 26]. These long-lived Rydberg states, which appear in molecules exist within a narrow range below each of the rotational, vibrational and electronic states near threshold [27] and below an electronic ionization threshold in atoms. These states exhibit a very long lifetime which violates the usual scaling of n^3 and were first discovered in NO [28]. ZEKE states can be created by collisions or even by laser excitation. When atoms are excited to a very high Rydberg state where a small Stark field (stray of intentional) breaks the spherical symmetry of the system, the degeneracy of the orbital angular momentum quantum state l is also broken. Thus, l does not remain a good quantum number in a uniform dc-field. The non-hydrogenic low-l states with quantum defect $(\delta_l \neq 0)$ are energetically separated from the hydrogenic high-l states which undergo a linear Stark effect. The low-l states are non-degenerate and undergo quadratic and possibly higher order Stark effects. The l-mixing occurs when the low-l state approaches the outermost component of the fanning of the high-l state. Due to the l-mixing, the dilution of low-l state enhances the lifetimes. The complete mixing of l-states enhances the lifetime by the factor of n. Further, dilution of the low-l component is realized for inhomogeneous fields as the result of the broken cylindrical symmetry as well, if present. The orbital magnetic quantum number does not remain a good quantum number then. Hence, the mixing between complete m states enhances the lifetime by another factor of n. Under these conditions of complete l and m mixing the lifetime is enhanced by the factor of n^2. Hence, the lifetimes of the highest l states scale as n^5 and the statistical mixture of the lm states within the same electronic state scales as $n^{4.5}$ [19].

The research presented here mainly investigates the formation of long-lived Rydberg states below the second ionization threshold in argon (which corresponds to the ionization limit for the $P_{1/2}$ ionic core). We measure the formation and survival of these high angular momentum states in the ultracold regime, specifically through laser excitation in a magneto-optical trap. The goal of this research is to understand the dynamics of ZEKE Rydberg state formation in an ultracold environment, to explore the dynamics of ultracold ZEKE-state interactions, and to apply these results to the study and control of ultracold plasmas.

This dissertation is organized as follows. We start our discussion with the underlying theory for the MOT of argon atoms and some properties of Rydberg atoms, and autoionizing states in the presence of an electric field in Chapter II. The experimental layout for the cooling and trapping of metastable argon is discussed in the first part of Chapter III followed by the different schemes of photoexcitations of the atoms to different Rydberg levels and the detection techniques used to probe the evolution dynamics as a function of time. In Chapter IV we present our data and a discussion of the important physics of our results. We conclude with a brief discussion of the future outlook for the experiments in Chapter V.

CHAPTER II

THEORY

II.1 INTRODUCTION

A simple model developed for studying the fundamental aspects of the interaction between an atom and the radiation field considers the interaction between a two level system and a single mode radiation field as shown in Fig. 1(a). This simple model has been very successful in providing insight into the forces on atoms corresponding to the momentum exchange between light and the atom. In reality, atoms contain many more than two levels, but fortunately, the essential physics of the system can often be understood in terms of a modest extension of the two level model. As we will show below, the interaction of light with an atom can be expressed in terms of two distinct types of forces as discussed in Sec. II.1.1. The light-matter interaction can be used to cool and confine atoms. Sometimes it is this cooling and confining ("trapping") process which is itself of interest, while other times- as here- the cold, trapped atoms provide the starting point for exploring atomic structure and dynamics. The basic mechanism of bringing atoms from room temperature to close to absolute zero is known as Doppler cooling and is outlined in Sec. II.1.2. The limits imposed due to the stochastic nature of the light absorption and re-emission process yield a Doppler limit to temperature as explained in Sec. II.1.3. This limit can be circumvented by considering the multi-level nature of real atoms which gives rise to the Sysiphus or polarization gradient cooling mechanism resulting in a temperature lower than that predicted by Doppler cooling. Sub-Doppler cooling methods will be discussed in Sec. II.2.1 and the three dimensional spatial confinement of atoms in the MOT will be discussed in Sec. II.2.3.

The experiments described in this dissertation involve the time-evolution of highly-excited atomic states known as Rydberg states, created in a sample of ultracold, trapped argon atoms. In Sec. II.3 we describe some of the properties of argon, followed in Sec. II.4 by a description of the important characteristics of Rydberg states. Both the ionization of ultracold atoms and the excitation of such atoms to highly-excited Rydberg states can result in the formation of an ultracold plasma. As a result, we next discuss how ultracold plasmas can be formed by excitation of ultracold atoms to either Rydberg states or to a region in energy just above the

ionization threshold. Finally, we conclude the chapter with a discussion of "ZEKE" (Zero Kinetic Energy) Rydberg states, the study of which is the main component of this dissertation.

II.1.1 Light forces

The interaction between light and an atom results in two kinds of forces on the atom (i) absorptive forces and (ii) dispersive forces depending upon the nature of interaction. The absorptive forces are dissipative in nature and hence useful for cooling while the dispersive (or reactive) force is conservative and hence cannot be used to cool atoms.

The total Hamiltonian H_{total} for atom + field system under the dipole approximation is given by

$$H_{total} = H_{atom} + V \tag{2}$$

where

$$V = -\vec{d} \cdot \vec{E} = -\vec{d} \cdot \hat{e}\, E_0(\vec{r}) cos(\omega_L t - \vec{k} \cdot \vec{r})) \tag{3}$$

with H_{atom} is an unperturbed atomic Hamiltonian and the laser field given by

$$\vec{E} = \hat{e} E_0(\vec{r})(cos\omega_L t - \vec{k} \cdot \vec{r})) \tag{4}$$

where $\hat{e}$ is the polarization of the light field.

The atom in the light field possesses a dipole moment $\vec{d}$ which is purely non-diagonal in the basis $\{|e\rangle, |g\rangle\}$ (excited and ground states respectively) which may be written as [29],

$$\vec{d} = \vec{d}_{ge}(|e\rangle\langle g|) + |g\rangle\langle e|) \tag{5}$$

with

$$\vec{d}_{eg} = \langle e|\vec{d}|g\rangle = \langle g|\vec{d}|e\rangle \tag{6}$$

$$\hbar\Omega = -\vec{d}_{eg} \cdot \hat{e}E_0 \tag{7}$$

where Ω is the Rabi frequency, representing the coupling between the laser field and the atomic dipole.

$$V = \frac{\hbar\Omega(\vec{r})}{2} \left(e^{-i\vec{k}\cdot\vec{r}} e^{i\omega_L t} + e^{i\vec{k}\cdot\vec{r}} e^{-i\omega_L t} \right) (|e\rangle\langle g| + |g\rangle\langle e|) \tag{8}$$
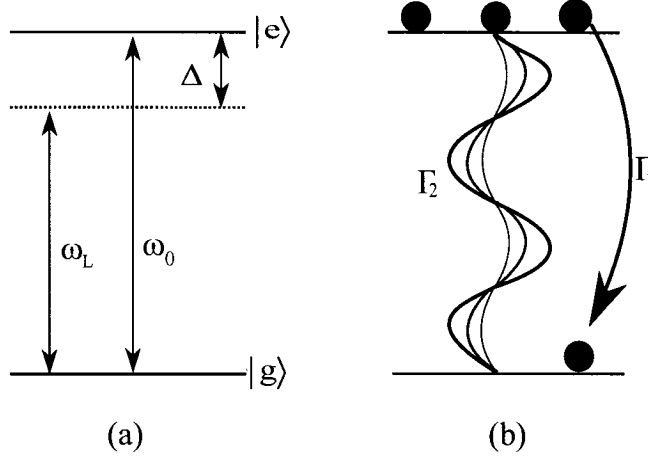
FIG. 1: (a) Two-level atom energy level diagram and (b) Relaxation rates Γ_1 and Γ_2 for the two level atom. Γ_1 is the population transfer rate and Γ_2 gives the relaxation of coherence.

where the terms $e^{-i\omega_L t}$ and $e^{i\omega_L t}$ describe the absorption and emission processes, respectively. We can usually neglect the terms $e^{i\omega_L t}|e\rangle\langle g|$ and $e^{-i\omega_L t}|g\rangle\langle e|$ which are non-resonant, thereby making what is known as the rotating wave approximation which reduces Eq. (8) to:

$$V = \frac{\hbar\Omega(r)}{2}\left(e^{i(\vec{k}\cdot\vec{r}-\omega_L t)}|e\rangle\langle g| + e^{-i(\vec{k}\cdot\vec{r}-\omega_L t)}|g\rangle\langle e|\right) \tag{9}$$

The mean radiative force on the atom can be derived as an expression identical to the classical expression for the force on a particle with a dipole moment

$$\langle\vec{F}\rangle = -\langle\nabla V\rangle \tag{10}$$

$$\nabla V(\vec{r},t) = \frac{\hbar}{2}\left(|e\rangle\langle g|e^{-i\omega_L t}\nabla\left[\Omega(\vec{r})e^{i\vec{k}\cdot\vec{r}}\right] + |g\rangle\langle e|e^{i\omega_L t}\nabla\left[\Omega(\vec{r})e^{-i\vec{k}\cdot\vec{r}}\right]\right) \tag{11}$$

$$\nabla\left[\Omega(\vec{r})e^{-i\vec{k}\cdot\vec{r}}\right] = \Omega(\vec{r})(-i\vec{k})e^{-i\vec{k}\cdot\vec{r}} + e^{-i\vec{k}\cdot\vec{r}}\nabla\Omega(\vec{r}) \tag{12}$$

$$\nabla\left[\Omega(\vec{r})e^{i\vec{k}\cdot\vec{r}}\right] = \Omega(\vec{r})(i\vec{k})e^{i\vec{k}\cdot\vec{r}} + e^{i\vec{k}\cdot\vec{r}}\nabla\Omega(\vec{r}) \tag{13}$$

$$\nabla V(\vec{r},t) = \frac{\hbar}{2}\left[e^{-i(\vec{k}\cdot\vec{r}-\omega_L t)}|g\rangle\langle e|\left(-i\vec{k}\Omega(\vec{r}) + \nabla\Omega(\vec{r})\right)\right.$$
$$\left. + e^{i(\vec{k}\cdot\vec{r}-\omega_L t)}|e\rangle\langle g|\left(i\vec{k}\Omega(\vec{r}) + \nabla\Omega(\vec{r})\right)\right] \tag{14}$$

Introducing the density matrix for the two-level system in the basis $\{|e\rangle, |g\rangle\}$:

$$\rho = \begin{pmatrix} \rho_{ee} & \rho_{eg} \\ \rho_{ge} & \rho_{gg} \end{pmatrix} \tag{15}$$

where the diagonal elements give the populations of the $|e\rangle$ and $|g\rangle$ states respectively. The off-diagonal elements are the coherence terms which gives the coupling strength between two states due to the interaction of the two-level system with the light fields.

$$Tr(\rho \nabla V) = \frac{\hbar \Omega}{2} \left\{ e^{-i(\vec{k}\cdot\vec{r} - \omega_L t)} \left[-i\vec{k} + \frac{\nabla \Omega}{\Omega} \right] \rho_{eg} \right.$$
$$\left. + e^{i(\vec{k}\cdot\vec{r} - \omega_L t)} \left[i\vec{k} + \frac{\nabla \Omega}{\Omega} \right] \rho_{ge} \right\} \tag{16}$$

$$Tr(\rho \nabla V) = \hbar \Omega \left[\frac{\rho_{ge} e^{i(\vec{k}\cdot\vec{r} - \omega_L t)} + \rho_{eg} e^{-i(\vec{k}\cdot\vec{r} - \omega_L t)}}{2} \frac{\nabla \Omega}{\Omega} \right.$$
$$\left. + \frac{\rho_{ge} e^{i(\vec{k}\cdot\vec{r} - \omega_L t)} - \rho_{eg} e^{-i(\vec{k}\cdot\vec{r} - \omega_L t)}}{2} i\vec{k} \right] \tag{17}$$

where $\langle \nabla V \rangle = Tr(\rho \nabla V)$, and for an atom at rest $\vec{r} = 0$.
Thus, the mean radiative forces becomes

$$\langle \vec{F} \rangle = -\hbar \Omega \left[u(t) \frac{\nabla \Omega}{\Omega} - v(t)\vec{k} \right] \tag{18}$$

with

$$u(t) = \frac{\rho_{ge} e^{-i\omega_L t} + \rho_{eg} e^{i\omega_L t}}{2} \tag{19}$$

$$v(t) = \frac{\rho_{ge} e^{-i\omega_L t} - \rho_{eg} e^{i\omega_L t}}{2i} \tag{20}$$

and $\Omega(0) = \Omega$.

The dynamics of the system can be described by the evolution of the density matrix ρ which obeys the Liouville-von Neumann equation:

$$i\hbar \frac{d\rho}{dt} = [H_{total}, \rho] + i\hbar L_D(\rho) \tag{21}$$

with L_D is the Liouville operator which takes into account for dissipative process like relaxation and dephasing due to spontaneous emission as shown in Fig. 1(b). For the two-level atom in the basis $|g\rangle$, $|e\rangle$, the Liouville operator L_D becomes

$$L_D = \Gamma \begin{pmatrix} \rho_{ee} & \rho_{ge}/2 \\ -\rho_{ge}/2 & \rho_{gg} \end{pmatrix} \tag{22}$$

with $\Gamma_1 = \Gamma$ and $\Gamma_2 = \Gamma/2$ where Γ is the lifetime of the excited state.

The diagonal elements give the rate of change of the populations of the two states (relaxation) and the off-diagonal elements give the rate of change in coupling (dephasing of coherence) between two states as a result of the dissipative process (spontaneous emission). Now, using the rotating-wave approximation (RWA) and the introduction of new variables defined as such

$$
\begin{aligned}
\hat{\rho}_{eg} &= \rho_{eg} e^{i\omega_L t} \\
\hat{\rho}_{ge} &= \rho_{ge} e^{-i\omega_L t} \\
\hat{\rho}_{gg} &= \rho_{gg} \\
\hat{\rho}_{ee} &= \rho_{ee}
\end{aligned}
\tag{23}
$$

leads to the Bloch equations. The equations of motion for the populations are,

$$\frac{d\hat{\rho}_{ee}}{dt} = -\Gamma \hat{\rho}_{ee} + i\frac{\Omega}{2}\left(\hat{\rho}_{eg} - \hat{\rho}_{ge}\right) \tag{24}$$

$$\frac{d\hat{\rho}_{gg}}{dt} = \Gamma \hat{\rho}_{ee} - i\frac{\Omega}{2}\left(\hat{\rho}_{eg} - \hat{\rho}_{ge}\right) \tag{25}$$

Similarly, the equations of motion for the coherences are:

$$\frac{d\hat{\rho}_{ge}}{dt} = -\left(\frac{\Gamma}{2}\hat{\rho}_{ge} + i\delta_L\right)\hat{\rho}_{ge} - i\frac{\Omega}{2}\left(\hat{\rho}_{ee} - \hat{\rho}_{gg}\right) \tag{26}$$

$$\frac{d\hat{\rho}_{eg}}{dt} = -\left(\frac{\Gamma}{2}\hat{\rho}_{ge} - i\delta_L\right)\hat{\rho}_{eg} + i\frac{\Omega}{2}\left(\hat{\rho}_{ee} - \hat{\rho}_{gg}\right) \tag{27}$$

$$\tag{28}$$

with $\delta_L = \omega_L - \omega_0$ is the detuning of the light of frequency ω_L from the atomic resonance frequency ω_0. The above Eq. (24) and Eq. (25) yields $d(\hat{\rho}_{ee} + \hat{\rho}_{gg})/dt = 0$. This implies the total number of electrons is conserved. Finally, we define other new variables, u, v, w:

$$u = \frac{1}{2}\left(\hat{\rho}_{ge} + \hat{\rho}_{eg}\right) \tag{29}$$

$$v = \frac{1}{2i}\left(\hat{\rho}_{ge} - \hat{\rho}_{eg}\right) \tag{30}$$

$$w = \frac{1}{2}\left(\hat{\rho}_{ee} - \hat{\rho}_{gg}\right) \tag{31}$$

and the set of equations reduces the familiar Optical Bloch Equations (OBE):

$$\dot{u} = -\frac{\Gamma}{2}u + \delta v \tag{32}$$

$$\dot{v} = -\delta u - \frac{\Gamma}{2}v - \Omega w \tag{33}$$

$$\dot{w} = \Omega v - \Gamma w - \frac{\Gamma}{2} \tag{34}$$

In steady state,

$$\begin{pmatrix} u_{st} \\ v_{st} \\ w_{st} \end{pmatrix} = \begin{pmatrix} \frac{\delta}{\Omega}\frac{s}{(1+s)} \\ \frac{\Gamma}{2\Omega}\frac{s}{(1+s)} \\ \frac{-1}{2(1+s)} \end{pmatrix} \tag{35}$$

where s is the saturation parameter defined as

$$s = \frac{\Omega^2/2}{\delta^2 + \frac{\Gamma^2}{4}} \equiv \frac{s_0}{1 + (2\delta/\Gamma)^2} \tag{36}$$

where $s_0 \equiv 2\Omega^2/\Gamma^2 = I/I_s$ gives the saturation parameter at resonance and the saturation intensity is

$$I_s = \frac{\pi hc}{3\lambda^3\tau} \tag{37}$$

For the low intensity $s \ll 1$, we get $w \simeq 1$ implying the population is mostly in the ground state. In the steady state, the absorption rate equals the emission rate $(w = \rho_{gg} - \rho_{ee} \rightarrow 0)$. The excited state population is given by [30]

$$\rho_{ee} = \frac{1-w}{2} = \frac{s}{2(1+s)} = \frac{s_0/2}{1 + s_0 + (2\delta/\Gamma)^2} \tag{38}$$

whereas in the limit $s >> 1$

$$\rho_{ee} = \frac{1}{2}(1+w) = \frac{s}{2(1+s)} \simeq \frac{1}{2} \tag{39}$$

Finally, we define the average value of $\vec{d}$

$$\langle d \rangle = Tr(\rho \vec{d}) \tag{40}$$

$$= \vec{d}_{ge}\,(\rho_{eg} + \rho_{ge})$$

$$= \vec{d}_{ge}\,\left(\hat{\rho}_{eg}e^{-i\omega_L t} + \hat{\rho}_{ge}e^{i\omega_L t}\right) \tag{41}$$

using Eq. (29) and Eq. (30)

$$\langle \vec{d} \rangle = \vec{d}_{ge}\,(u(t)\cos\omega_L t - v(t)\sin\omega_L t) \tag{42}$$

We can see that u and v describe the in-phase and quadrature components of the light field with respect to $\langle \vec{d} \rangle$. Thus, in the steady state, the in-phase and the quadrature components of the forces are written as

$$\vec{F} = \vec{F}_{react} + \vec{F}_{dissip}$$

The light force proportional to the in-phase component of the mean dipole moment and the amplitude gradient is called reactive or dipole force. This is conservative in nature.

$$\vec{F}_{react} = -\hbar u_{st}\nabla\Omega \tag{43}$$

The dipole force is zero at resonance ($\delta = 0$), and for $|\delta| \gg \Gamma$ (for an intensity such that ($|\delta| \gg \Omega$). Using From Eq. (43) together with Eq. (35) the dipole force reduces to

$$\vec{F}_{react} = -\nabla\frac{\hbar\Omega^2}{4\delta} = -\nabla U_{dipole} \tag{44}$$

where

$$U_{dipole} \simeq \frac{\hbar\Omega^2}{4\delta} \equiv \frac{\hbar\Gamma}{8}\frac{\Gamma}{\delta}\frac{I}{I_0} \tag{45}$$

The light force proportional to the quadrature of the mean dipole moment and to the phase gradient is called the dissipative force or scattering force.

$$\vec{F}_{dissip} = \hbar\Omega v_{st}\vec{k} \tag{46}$$

Eq. (34) in steady state becomes

$$\Omega v_{st} - \Gamma w_{st} - \Gamma/2 = 0 \tag{47}$$

$$\Omega v_{st} = \Gamma \left(\tfrac{1}{2} + w_{st} \right) \tag{48}$$

$$\Omega v_{st} = \Gamma \rho_{ee} \tag{49}$$

Eq. (46) and Eq. (49) give

$$\vec{F}_{dissip} = \hbar \vec{k} \Gamma \rho_{ee} \tag{50}$$

using Eq. (38), Eq. (50) becomes

$$\vec{F}_{dissip} = \frac{\hbar \vec{k} s_0 \Gamma/2}{1 + s_0 + (2\delta/\Gamma)^2} \tag{51}$$

The dissipative force arises from the absorption followed by the spontaneous emission of photons. A photon carries energy and has momentum. Whenever the energy of the incident photon matches the energy difference between the ground and the excited state of the atom $\hbar \omega_L = E_e - E_g = \hbar \omega_0$, the atom absorbs the photon. Absorption of a photon leads to the transfer of momentum from the optical field to the atom. In a single absorption, therefore, the atom gains the momentum equal to the momentum of photon $p_i = \hbar k_i$ in the direction of the photon, and the electron is excited to the quasi-stable excited state. The electron decays to the stable ground state after the lifetime of the excited state, spontaneously emitting the photon. The atom gets the recoil kick during the spontaneous emission as shown in the Fig. 2(a). The net change in the momentum of the atom becomes $\langle \Delta \vec{p} \rangle = \langle \hbar \vec{k}_i - \hbar \vec{k}_f \rangle = \hbar \vec{k}_i$. Therefore, the associated recoil velocity, recoil energy and maximum acceleration for an atom of mass M respectively becomes $v_{rec} = k/M$, $E_{rec} = \hbar^2 k^2/2M$ and $a_{max} = F_{max}/M = \hbar k \Gamma/2M$.

The spontaneous fluorescence is in a random direction; the ensemble average results in a zero net contribution to the change in momentum during spontaneous fluorescence. On the average, the net force experienced by the atom becomes

$$\vec{F}_{dissip} = \frac{d\vec{p}}{dt} = \hbar \vec{k} \mathcal{R}_{scat} \tag{52}$$

where $\mathcal{R}_{scat}$ is the scattering rate equal to $\Gamma \rho_{ee}$, with Γ the linewidth of the excited state and ρ_{ee} is the excited state fraction.
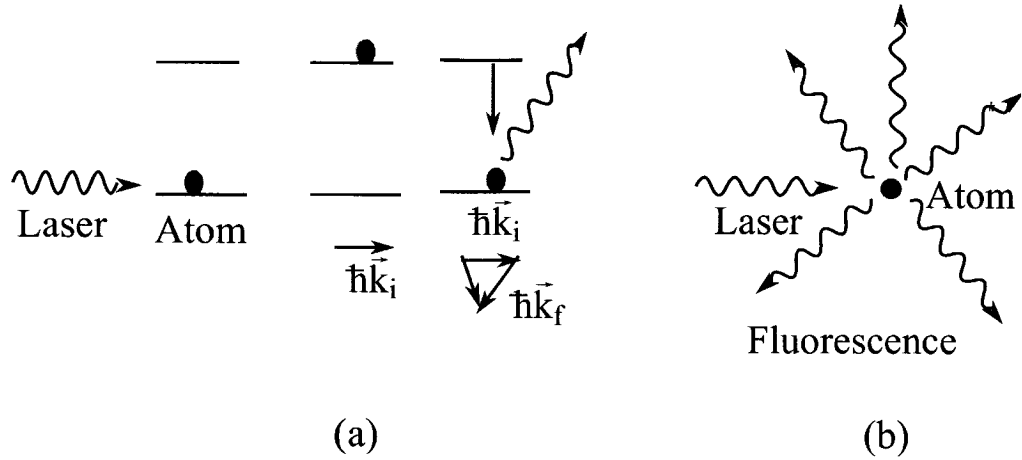
FIG. 2: The absorption of a photon followed by the spontaneous emission in all possible random directions.

II.1.2 Atoms in motion and Doppler cooling

Cooling of a system of atoms refers to reducing the average motion of the constituent atoms in the ensemble. The relative motion between the atoms and the light source alters the frequency of the light as seen by the atom as a consequence of the Doppler effect. This fact can be exploited to make the radiation pressure force velocity dependent. The resulting shift in the frequency is given by $\omega_D = -\vec{k} \cdot \vec{v}$ as in Fig. 3.

The inclusion of the doppler shift in the scattering force due to the counter-propagating beam leads to

$$\vec{F} = \frac{\hbar \vec{k} \Gamma}{2} \frac{s_0}{1 + s_0 + [2(\delta + |\omega_D|)/\Gamma^2]} \tag{53}$$

Fig. (3) depicts a motionless atom in between counter-propagating, red-detuned monochromatic laser beams. The atom sees both the beams having the same frequency and scatters the same. Hence, the atom experiences no net light force. Once the atom starts to move along the direction of one of the beams, the atom sees the counter-propagating beam has higher frequency, closer to the resonance. Hence the atom scatters more from this beam than the other, causing an imbalance in the light force. The co-propagating beam appears to have lower frequency in the atomic
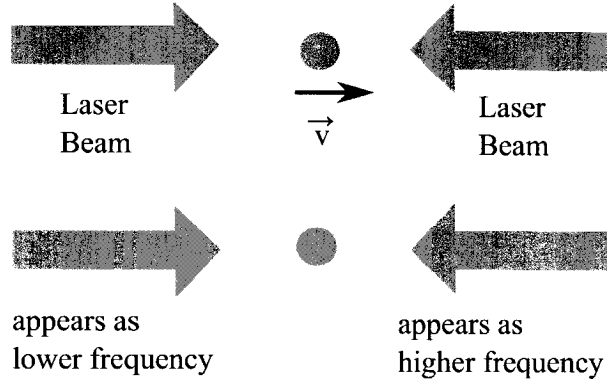
FIG. 3: Doppler shift in the frequency due to the atomic motion.

frame of reference making it even farther detuned from resonance and hence scattering from this beam decreases. Therefore, the atom always experiences the resultant force against its motion [4] as shown in Fig. 3. Fig. 4(a) illustrates the atomic response to the oncoming beam. At resonance, the atom responds more to the beam (ie, the atom experiences more light force) and it becomes less and less responsive as the frequency of the beam is detuned from the resonance. The variation of the forces due to the two beams is as shown in the Fig. 4(b). The resultant light force on the atom can be denoted as:

$$\vec{F}_{OM} = \vec{F}_+ + \vec{F}_- \tag{54}$$

where

$$\vec{F}_\pm = \pm \frac{\hbar \vec{k} \Gamma}{2} \frac{s_0}{1 + s_0 + [2(\delta \mp |\omega_D|)/\Gamma]^2} \tag{55}$$

The sum of two light forces, with the semiclassical assumption that $|\omega_D| << \delta$ gives in the limit of $s_0 << 1$,

$$\vec{F}_{OM} = \frac{8\hbar \delta k^2}{\Gamma} \frac{s_0}{1 + (2\delta/\Gamma)^2} \cdot \vec{v} = -\alpha \vec{v} \tag{56}$$

with the damping coefficient α equal to

$$\alpha = -\frac{8\hbar \delta k^2}{\Gamma} \frac{s_0}{[1 + (2\delta/\Gamma)^2]^2} \tag{57}$$

and with $\delta = -\Gamma/2$ for maximum damping for a given small velocity v.
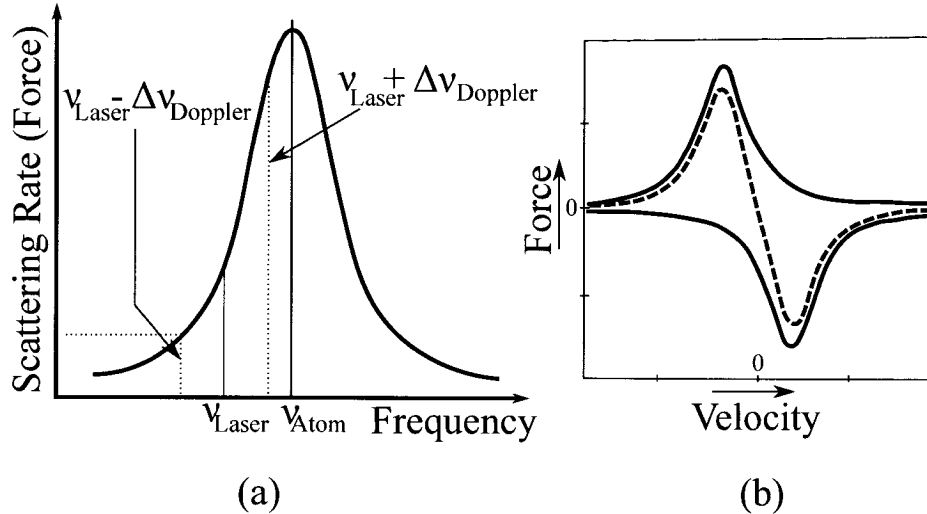
FIG. 4: Doppler shift in the frequency due to the atomic motion, (b) velocity dependence of the optical damping forces for 1-D optical molasses. The solid line is the resultant of the two forces from each beam.

Hence, an atom traveling at low velocities in the presence of a low intensity field experiences a damping force which is linear with the velocity. Such a force is dissipative in nature, like a frictional or viscous force.

II.1.3 Doppler cooling limits

The viscous force considered above is the mean force, averaged over several fluorescence cycles. The randomness of radiative processes introduces fluctuations in the atomic motion [31]. The atom cannot cool down to exactly $v = 0$. The Doppler friction responsible for the cooling is accompanied by the recoil due to the fluorescence emission in a random direction and at random times. The number of fluorescence cycles in a given interval is random. Hence, the momentum absorbed during the interval is random as well. The force on the atom from a single laser beam is $\vec{F} = \vec{F}_{abs} + \delta\vec{F}_{abs} + \vec{F}_{spont} + \delta\vec{F}_{spont}$ [32] with $\langle\vec{F}_{abs}\rangle = \vec{F}_{scatt}$ and $\langle\vec{F}_{spont}\rangle = 0$. Over many spontaneous emission processes the expectation value for the momentum is zero. However, the expectation value for p^2 is non-zero. The discrete step size of random recoil momentum $\hbar k$ constitutes a heating mechanism which can be modeled by the random walk in momentum space (analogous to the Brownian motion of microscopic particles in air) as in Fig. 5. A random walk of $\mathcal{N}$ steps gives the mean
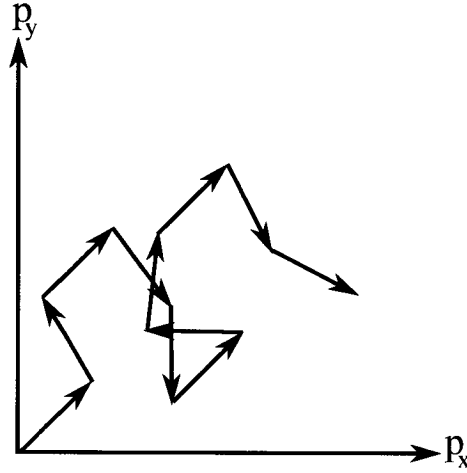
FIG. 5: Two dimensional random walk of the momentum in momentum space with a step of $\hbar k$ as a result of the spontaneous fluorescence and of the photons in random directions.

square distance traveled equal to $\sqrt{\mathcal{N}} \times$ the square of step length. For an atom in two counter-propagating beams, the radiation forces cancel but the effect of the fluctuations is cumulative. The diffusive increase in the momentum squared due to $\langle \delta \vec{F}_{spont} \rangle + \langle \delta \vec{F}_{abs} \rangle$ can be written as

$$\langle p^2 \rangle = (\hbar k)^2 N_{scatt} \tag{58}$$

where N_{scatt} is the number of photon recoil events that increases the energy of the atom given by $N_{scatt} = 2(2\mathcal{R}_{scatt}t)$. The factor 2 is for absorption from six counter propagating beams and the other factor 2 is for the spontaneous emission [32].

In the approximation of $s_0 \ll 1$ and small velocity $|\omega_D| \ll \delta$ the rate of change of $\langle p^2 \rangle$ gives,

$$\frac{d\langle p^2 \rangle}{dt} = 4(\hbar k)^2 \Gamma \rho_{ee} = 2(\hbar k)^2 \Gamma \frac{s_0}{1 + (2\delta/\Gamma)^2} = 2D \tag{59}$$

where D is the momentum diffusion coefficient defined as

$$D = (\hbar k)^2 \Gamma \frac{s_0}{1 + (2\delta/\Gamma)^2} \tag{60}$$

$$\frac{dE_{heat}}{dt} = \frac{1}{2m}\frac{dp^2}{dt} = \frac{2(\hbar k)^2}{m}\frac{\Gamma}{2}\rho_{ee} = \frac{D}{m} \tag{61}$$

$$\frac{dE_{heat}}{dt} = \frac{(\hbar k)^2 \Gamma}{m} \frac{s_0}{1 + (2\delta/\Gamma)^2} = \frac{D}{m} \tag{62}$$

The rate of change of average kinetic energy as a result of the viscous force can be written as

$$\frac{dE_{cool}}{dt} = F_{OM}v = -\alpha v^2 \tag{63}$$

where F_{OM} is the viscous force derived in Eqs. 56 and 57. The velocity of the atom is denoted as v. The competition between doppler cooling and heating associated with the momentum diffusion due to the fluctuations of the forces leads to the equilibrium temperature.

$$\frac{dE_{heat}}{dt} = \frac{dE_{cool}}{dt}$$
$$mv^2 = \frac{D}{|\alpha|} \tag{64}$$

using the equipartition theorem, $\frac{1}{2}mv_{rms}^2 = k_B T$. Eq. (64) becomes

$$K_B T = \frac{\hbar \Gamma}{4} \frac{1 + (2\delta/\Gamma)^2}{2|\delta|/\Gamma} \tag{65}$$

which gives the Doppler limit temperature at $\delta = -\Gamma/2$

$$T_D = \frac{\hbar \Gamma}{2K_B} \tag{66}$$

This is the minimum temperature possible due to Doppler cooling alone.

II.2 MULTILEVEL ATOMS AND BEYOND DOPPLER LIMIT

Sodium atoms in an optical molasses were found by Bill Phillips and coworkers to have temperatures well below the Doppler limit predicted by theory. Sodium is an alkali metal atom and has hyperfine structure in its ground state. This multi-level structure, it was found, allows new processes that helps in cooling beyond the Doppler limit. The phenomenon that allows the atoms to cool down below the Doppler limit, also called Sysiphus cooling is explained in Sec. II.2.1.

II.2.1 Sysiphus or polarization gradient cooling

The mechanism leading to the temperatures lower than the Doppler limit is called "polarization gradient cooling" or "Sisyphus cooling." The basis of Sisyphus cooling makes use of the polarization gradient of the light. For the configuration of a pair of counter propagating linearly, but orthogonally polarized beams called "lin⊥lin" introduced by Dalibard and Cohen-Tannoudji and by Ungar and his coworkers, the relative phase of the two beams changes in space, and the resulting field has a space dependent polarization. The polarization is linear for the relative phase difference of 0 or π and circular for the phase difference of $\pi/2$ and $3\pi/2$, see Figs. 6(b) and 6(c) [32]. Hence, the polarization gradient is periodic with the period of $\lambda/2$ (where λ is the wavelength of the beam). At position with σ^- polarization the atom is pumped $|\frac{1}{2}, \frac{1}{2}\rangle \to |\frac{3}{2}, \frac{-1}{2}\rangle$ and it decays $|\frac{3}{2}, \frac{-1}{2}\rangle \to |\frac{1}{2}, \frac{-1}{2}\rangle$ because this transition has more probability because of large Clebsch-Gordan coefficients. The emitted photon is bluer than the absorbed one and the energy is dissipated. The cycles of absorption and spontaneous emission in σ^- light results in the optical pumping from $|\frac{1}{2}, \frac{1}{2}\rangle \to |\frac{1}{2}, \frac{-1}{2}\rangle$. The optical pumping due to σ^+ follows the same principle to cause the optical pumping from $|\frac{1}{2}, \frac{-1}{2}\rangle \to |\frac{1}{2}, \frac{1}{2}\rangle$ which has lower energy. Now, the atom has to move up the hill at the expense of its own kinetic energy to overcome the potential hill. At the top of the hill one of the two cycles takes place for optical pumping depending upon the helicity of the beam at that point. Such a process resembles the story of Sysiphus in Greek myth who pushes the stone to the top of the hill then he finds the stone at the bottom of the valley again. The process continues and the kinetic energy of the atoms decreases until the kinetic energy of the atom equals the potential hill.

In the case of the two counter propagating beams with opposite helicity, the polarization gradient consists of a spatially rotating linear polarization, and there is no such light shifts. Therefore, there is no Sisyphus cooling. However, as the atom moves along the beam direction, it sees a rotating polarization vector. This induces alignment of the sub-states that changes the radiation pressure balance such as to slow down the motion of the atom.
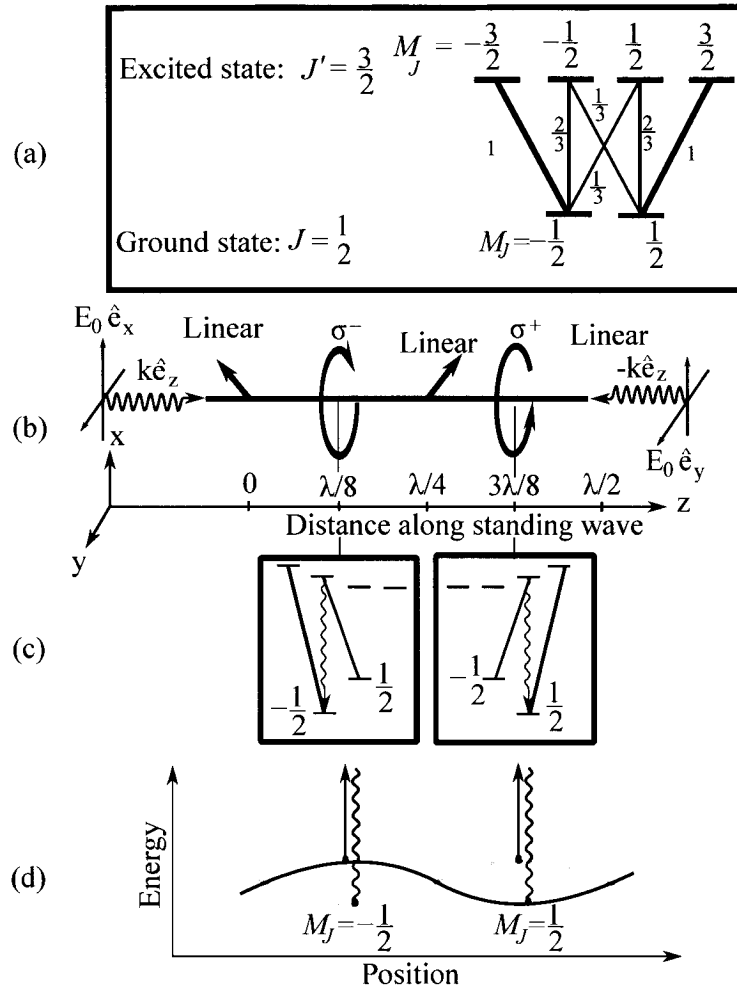
FIG. 6: (a) The Zeeman sublevels of the ground state $J = 1/2$ and excited state $J = 3/2$ with the relative strength of each transition, (b) the polarization gradient that results from the superposition of two orthogonal linearly polarized beams, (c) the energies of the states at the positions of σ^+ and σ^- polarization with the unperturbed energy level indicated by the dotted line, (d) the spatial dependence of the light shifts of the ground-state sublevels of $J = 1/2$ and $J = -1/2$ with the transitions $J = 1/2 \to J = -1/2$ at σ^- followed by spontaneous fluorescence to $J = -1/2$ and the transitions $J = -1/2 \to J = 1/2$ at σ^+ followed by spontaneous fluorescence to $J = 1/2$.

II.2.2 The recoil limit

The polarization gradient cooling has a limit imposed due to the random momentum "kick" imparted to an atom by a single spontaneously emitted photon which is known as the recoil limit. The expression for the recoil limit can be derived using the equipartition theorem as

$$K_B T_R \sim \frac{\hbar^2 k^2}{M}$$
$$T_R \sim \frac{\hbar^2 k^2}{K_B M} \tag{67}$$

II.2.3 Spatial dependent force and magneto-optical trap

The Doppler force given by Eq. (56) is a function of the velocity and independent of the spatial coordinates. Such a force can only cool the atoms but it is not sufficient for the spatial localization of the atoms and therefore atoms cannot be trapped. Ashkin and Gordon [8] demonstrated that the scattering force provided by the configuration of the six counter-propagating laser beams cannot trap atoms. However, a stable trap is possible by using some external field to exploit the internal structure of the atom to make the force spatially dependent [33]. J. Dalibard conceived the idea of using the magnetic field gradient in making a spatially dependent force which was generalized to 3-dimensions [34] and became the basis of Laser Cooling and Trapping through realization of the MOT.

The presence of the magnetic field breaks the degeneracy of m_J levels due to the Zeeman effect and the shift in the level is given by,

$$\Delta E = g_J m_J \mu_B B \tag{68}$$

with g_J and μ_B the Landé g factor and Bohr magneton, respectively. In the presence of the magnetic field gradients Eq. (68), the shift in energy level becomes position dependent as $\Delta E = \beta x$, with $\beta = g_J m_J \mu_B G$ where $\vec{B} = G\vec{x}$ with $G = \frac{\partial B}{\partial x}$ as the field gradient and x is the coordinate with respect to the center.

The simplified one-dimensional model with a transition in a two level system with $J = 0$ as a ground state and $J = 1$ as an excited state is used to understand the optical trapping scheme as shown in Fig. 7. The atom is placed in between two counter-propagating beams of opposite helicity and equal red-detuning with respect to the transition between a pair of $J = 0$ and degenerate $J = 1$ levels. Therefore,
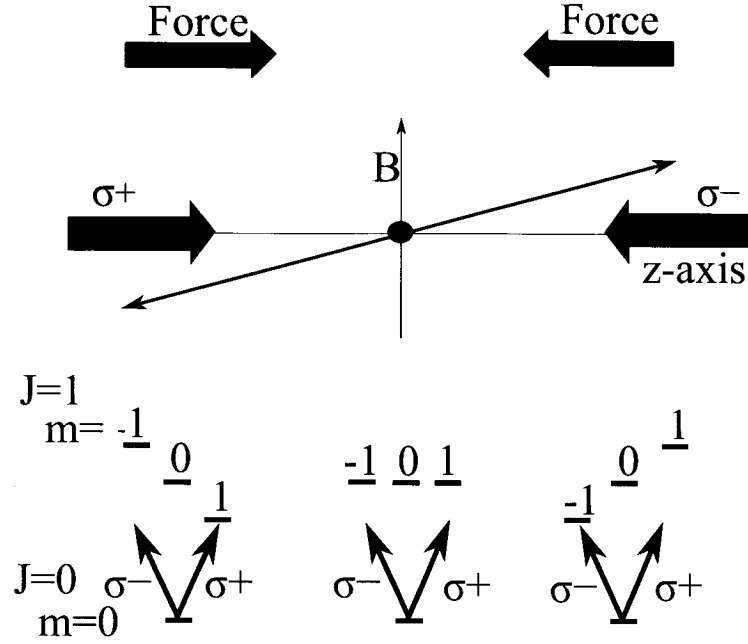
FIG. 7: Simplified schematic for one-dimensional Magneto-Optical Trap.

the atom experiences equal forces from the both beams irrespective of the position of the atom. The application of the magnetic field gradient splits the degeneracy of the excited $J = 1$ level into three $m_J = -1$, 0, 1 levels. If the atom is located to the right of the center (the position of $B = 0$), the splittings of $J = 1$ levels are such that $J = 0 \rightarrow J = 1$ with $m_J = -1$ transition is closer to the laser frequency whereas the $J = 0 \rightarrow J = 1$ with $m_J = 1$ moves far from the light frequency. Hence, the atom preferentially scatters the left circularly polarized photons $(\sigma-)$ more than the right circularly polarized photons $(\sigma+)$ creating the net force that pushes the atom towards the center. The same principle holds true for the atom located on the left. Thus, this forces confine the atoms in space. The total force in Eq. (55) including the Zeeman shift for the configuration shown in Fig. 7 is

$$\vec{F}_{MOT} = \hbar \vec{k} \frac{\Gamma}{2} \left[\frac{s_0}{1 + s_0 + (2(\delta - \xi)/\Gamma)^2} - \frac{s_0}{1 + s_0 + (2(\delta + \xi)/\Gamma)^2} \right] \tag{69}$$

where

$$\xi = \omega_D + \beta x \tag{70}$$
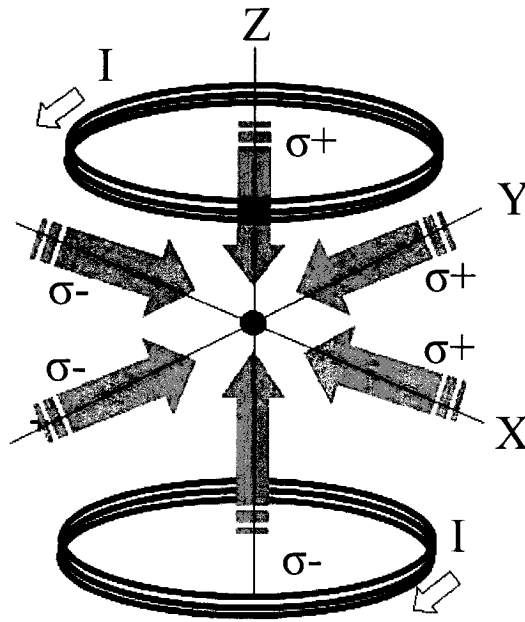
FIG. 8: The schematic of three dimensional laser cooling and trapping using a pair of anti-Helmholtz coils and six counter propagating beams of opposite helicity.

The principle of localization of the atoms in one dimension is illustrated in Sec. II.2.3. The same argument can be extended to three dimension in order to cool and trap the atoms in real three dimensional space. The magnetic field gradient in three dimensions is achieved by making a magnetic quadrupole field. This is done by a pair of circular coils in the anti-Helmoltz configuration, see Fig. 8. The typical gradients are 10 G/cm.

II.3 SPECTRA OF ARGON

Spectroscopy of the rare gases has been a subject of interest for both experimental and theoretical groups all over the world. The interesting aspects arise from the fact that they have a closed outermost shell hence, are largely inert in nature, chemically stable and have high ionization energy. A partial energy level diagram is shown in Fig. 10. The s-shell is closed for helium $1s^2$ and the other elements in the group have their p-shell completely filled, yielding the configurations mp^6, where $m = 2$, 3, 4, 5 and 6 for neon, argon, krypton, xenon and radon respectively, see Fig. 9. The total angular momentum J, the orbital angular momentum L, and the total spin for the

FIG. 9: The rare gases belong to Group 18 in the periodic table [35].

closed shells are all zero. So, the ground state for these elements is represented as $^1S_0$. The coupling scheme describes the interaction of electrons in atoms. It shows the scheme of the vector addition of orbital l_i and s_i momenta of the atomic electrons into total angular momentum J. For light atoms (small Z) the electrostatic interaction V_{es} among the electrons is dominant over the spin-orbit interaction V_{so}. In this case it is appropriate to couple the orbital angular momenta l_i of the electrons to form the total orbital angular momentum L and spin angular momenta s_i to give the total spin angular momentum S. Then couple L and S to form the total angular momentum J. The coupling scheme of the angular momenta is designated as

$$L = \sum_N l_i \quad ; \quad S = \sum_N s_i \tag{71}$$

where J can take the values

$$|L - S| \leq J \leq L + S \tag{72}$$

The state in the LS-coupling scheme is denoted as

$$2S+1L_J \tag{73}$$

where $2S + 1$ gives the multiplicity of the state.

With increasing atomic number Z (for large Z), the opposite situation occurs with $V_{es} << V_{so}$, and the jj-coupling scheme is used. The angular momentum coupling scheme designated as

$$|l_i - s_i| \leq j_i \leq (l_i + s_i) \quad ; \quad J = \sum_N j_i \tag{74}$$

The state in the jj-coupling scheme is denoted as

$$[(l_1, \ s_1)j_1, (l_2, \ s_2)j_2]_J \tag{75}$$

When the electrostatic interaction becomes comparable to the spin-orbit interaction $(V_{es} \approx V_{so})$, the states are described by the intermediate coupling scheme called jl-coupling [36] and [37]. When one electron is on average at a large distance from the atomic core, the spin-orbit interaction of the electrons of the atomic core is larger than the electrostatic interaction of these electrons jl coupling is used. In this scheme, the atomic core electrons follows an LS-coupling scheme. The individual $l_{i(core)}$ of the core electrons are coupled to form the total orbital angular momentum of the core electrons, and the individual $s_{i(core)}$ of the core electrons are coupled to form the total spin angular momentum of the core electrons designated as

$$L_{core} = \sum_{icore} l_{i(core)} \quad ; \quad S_{core} = \sum_{icore} s_{i(core)} \tag{76}$$

$$|L_{core} - S_{core}| \leq j_{core} \leq (L_{core} + S_{core}) \tag{77}$$

Then, the total angular momentum of the core electrons is coupled to the orbital angular momentum of the excited electron l_{exc} to give K,

$$|j_{core} - l_{exc}| \leq K \leq (j_{core} + l_{exc}) \tag{78}$$

and finally the angular momentum K is coupled with the spin angular momentum s_{exc} to give the total angular momentum J

$$|K - s_{exc}| \leq J \leq (K + s_{exc}) \tag{79}$$
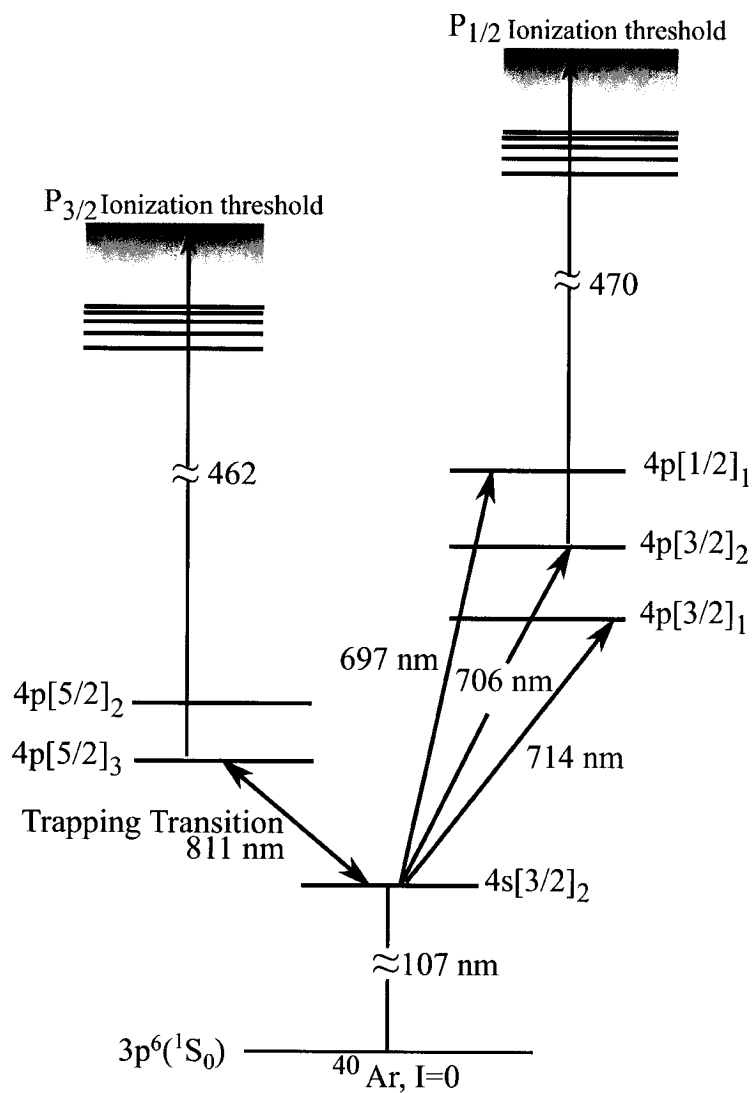
FIG. 10: Partial energy levels of ^{40}Ar.

In jl- coupling the term is designated as

$$nl\ ^{2s_{exc}+1}[K]_J \tag{80}$$

The work presented in this thesis deals with the various traits of argon. Argon is the third element in the group 18 shown in Fig. 9. The electronic ground state has a $(1s)^2(2s)^2(2p)^6(3s)^2(3p)^6\ ^1S_0$ configuration. The first excited manifold is $(1s)^2(2s)^2(2p)6(3s)^2(3p)^54s$, abbreviated in the following as $(3p)^54s$. The total L_{core} and S_{core} does not remain zero anymore and there occurs various spin-orbit configurations of the core. However, $L_{core} = 1$ and $S_{core} = 1/2$ for argon giving rise to the two states of ionic core corresponding to two different values of the total angular momentum of the core $j_{core} = |L_{core} \pm S_{core}| = |1 \pm 1/2|$ gives $j_{core} = 3/2$ or $1/2$. The first ionization potential corresponding to $3p^5\ ^2P_{3/2}$ ionic state is 127109.9 cm^{-1}. The excited state spin orbit state $^2P_{1/2}$ lies ~ 1431 cm^{-1} above the first ionization potential.

Therefore, there are two different series of the excited states converging to two ionization thresholds, each corresponding to one of the two spin-orbit configurations of the core $j_{core} = 3/2$ and $j_{core} = 1/2$ respectively. The core is denoted as $(1s)^2(2s)^2(2p)^6(3s)^2(3p)^5\ (^2P^0_{3/2})$ or simply $^2P^0_{3/2}$ and $^2P^0_{1/2}$ where the left superscript indicates the multiplicity of the ionic core, the right superscript 0 indicate the core is odd parity of ungerade and the subscript denotes j_{core}. The orbital angular momentum of the excited electron is labeled as l_{exc} and l'_{exc} for the ionic cores of $^2P^0_{3/2}$ and $^2P^0_{1/2}$ respectively. We often ignore expressing the parity for convenience and use $^2P_{3/2}$ and $^2P_{1/2}$ to express the ionic cores instead. Single photon excitation from the ground state is not feasible with available lasers. The process of excitation is explained in detail in Chapter III, the trapping of argon is achieved by the excitation to the meta-stable state $3s^23p^5(^2P^0_{3/2})4s$ or $^2[3/2]^0_2$ by using a radio frequency (rf) discharge. Optical transitions originating from the metastable state are possible with commercially available lasers like a Ti-Sapphire laser, solid state laser, dye lasers, etc. The cooling and trapping involves the transitions $3s^23p^5(^2P^0_{3/2})4s$ or $^2[3/2]^0_2 \leftrightarrow 3s^23p^5(^2P^0_{3/2})4p$ or $^2[5/2]_3$ with the laser beam of wavelength $\lambda \simeq 810nm$. Finally, we note that even isotopes of the the rare gases do not have nuclear spin and hence do not have hyperfine structure.

TABLE I: Hartree's atomic units

Physical Quantity	Atomic Units	SI Units
Electron charge e	1	1.602×10^{-19}Coulomb
Electron mass m_e	1	9.109×10^{-31}kg
Reduced Planck constant $\hbar$	1	1.0545×10^{-34}J
Fime structure constant	$e^2/\hbar c = 1/137$	$1/137$
Speed of light c	$1/\alpha = 137$	299792458 m/s
Bohr radius a_0	$\hbar^2/(m_e e^2) \equiv 1$ Bohr	5.29×10^{-11}m
Potential energy of an electron $1a_0$ from a proton $(= 2R_y)$	$e^2/a_0 \equiv 1$Hartree	$e^2/4\pi/\epsilon_0 a_0 = 4.359 \times 10^{-18}$J
Atomic unit of time	$\hbar^3/(m_e e^4) = 1$	2.419×10^{-17}sec
Frequency	1	4.134×10^{16}Hz
Electric field on electron a_0 from proton	1	5.142×10^{11} V/m
Electric dipole moment of electron a_0 from proton	$ea_0 = 1$	8.5×10^{-30}Coulomb-m
Standard a.u of B-field	1	2.5×10^5 Tesla
Bohr magneton μ_b	$e\hbar/(2m_e c) = 1/274$	$e\hbar/(2m_e) = 9.2 \times 10^{-24}$ J/Tesla

II.4 RYDBERG ATOMS

Rydberg never saw a Rydberg atom. An atom in which a single electron is excited to a state with a large principal quantum number, n, exhibits properties quite different than those where electrons are excited to low lying states. Some of their properties and their dependence on n are listed in Table II. The average separation between the excited Rydberg electron and the core (nucleus and the remaining electrons) is large, so any species of Rydberg atoms possess the gross properties similar to those of the hydrogen atom. The binding energy of the electron decreases rapidly as n increases, so at very high n very little energy is required to ionize it and such a process is called field ionization if done using a field. At high-n, the excited electron is very far from the core ion and the Coulombic field experienced by the electron is very small, so even a very weak externally applied electric field on the order of $mVcm^{-1}$ can strongly perturb the electron and cause a large Stark shift to the energy levels of the atom.

II.4.1 Hartree's atomic units

For convenience, it is common in atomic physics theory to work in "atomic units." This thesis follows the Hartree atomic units. This system of measures is based on atomic parameters. This convention assumes $e = m_e = \hbar = a_0 = 1$ where e, m_e, are the charge and the mass of the electron respectively. The unit of angular momentum is $\hbar = h/2\pi$ with h, Planck's constant and a_0 is the Bohr radius. The atomic units for different useful physical quantities in this thesis have been outline in Table. I

II.4.2 General properties of Rydberg atoms

The name Rydberg state is derived from their spectrum which follows nearly, but not quiet Rydberg's energy formula for hydrogen. Rydberg states have a number of striking properties, including nearly macro-dimension size and large polarizabilities, long lifetimes and nearly classical behavior. The first signature of Rydberg atoms was observed in 1885 when Balmer related the line position of atomic hydrogen to Balmer's formula for the wavelength in the visible range [19].

$$\lambda = \frac{bn^2}{n^2 - 1} \tag{81}$$

TABLE II: Some properties of Rydberg atoms

Property	n-dependence
Binding energy	n^{-2}
Energy between adjacent states	n^{-3}
Orbital radius	n^2
Geometric Cross section	n^4
Dipole moment $\langle nd|er|nf \rangle$	n^2
Polarizability	n^7
Radiative lifetime	n^3
Fine-structure interval	n^{-3}

where $b = 3645.6\ \overset{\circ}{A}$. Rewriting Balmer's formula in terms of wavenumber instead of wavelength yields [38]

$$\nu = \left(\frac{1}{4b}\right)\left(\frac{1}{4} - \frac{1}{n^2}\right) \tag{82}$$

This expression describes the series of transitions originating from $n = 2$ and going to high lying levels. In 1890 Rydberg expressed the wavenumbers of different observed lines in other atoms, notably alkali atoms with the single formula

$$\nu_l = \nu_{\infty l} - \frac{R_y}{(n - \delta_l)^2} \quad \text{for} \quad l = \text{s, p, d,} ... \tag{83}$$

with the constants $\nu_{\infty l}$ as the series limit and δ_l is known as the quantum defect for the series (the series with the same orbital angular momentum quantum number, l) and will be discussed in a later section. R_y is the universal Rydberg constant $R_y = 109721.6\ cm^{-1}$. The physical significance of high principal quantum number n came to light after Bohr proposed the Hydrogen atom model composed of a single electron moving classically in a circular orbit around the nucleus. Such an atom contains the properties of Rydberg atoms and gives the relation between the orbital radius and the principal quantum number, n

$$r = \frac{n^2 \hbar}{Ze^2 mk} = a_0 n^2 \quad \text{with} \quad a_0 = 0.53 \overset{\circ}{A} \tag{84}$$

The above expression illustrates that the size of the atom increases as the square of the principal quantum number n which implies the high n states have very large

orbits. And, a comparison between the Bohr relation for energy and the Rydberg formula yields

$$R_y = \frac{k^2 Z^2 e^4 m}{2\hbar^2} \qquad (85)$$

II.4.3 Classical view of the Rydberg electron trajectory

The classical view of the Rydberg atom provides the fundamental ideas for understanding the very long lifetime of the "ZEKE" states investigated in this dissertation. For simplicity, we can consider the simplest atomic system, a Hydrogen atom, which has a single electron bound to the nucleus by the Coulomb potential, $V(r) = -1/r$ where r is the distance between the center of the force (nucleus) and the electron. The atomic Hamiltonian for the Coulomb system in atomic units (a.u.) can be written as

$$H_0 = \frac{\vec{p}^{\,2}}{2} - \frac{1}{|\vec{r}|} \qquad (86)$$

where $\vec{p}$ is the linear momentum of the electron. The total energy E and the angular momentum $\vec{L} = \vec{r} \times \vec{p}$ are conserved since the Coulomb potential is spherically symmetric. The motion of the electron is confined to the single orbital plane normal to the fixed vector $\mathbf{L}$. The bound solutions for the above Hamiltonian can be characterized classically as the Kepler's orbit, like the planets around the sun without perturbation, or little perturbation due to other planets. There exists an additional constant of motion that commutes with the Hamiltonian, H known as the Lenz vector or Laplace-Runge-Lenz vector [39], whose absolute value gives the eccentricity of the trajectory and specifies the orientation of the orbit on the plane.

$$\vec{A} = \vec{p} \times \vec{L} - \hat{r} \qquad (87)$$

The vector $\vec{p} \times \vec{L}$ lies in the plane perpendicular to $\vec{p}$ which is tangential to the orbit and perpendicular to $\vec{L}$, which itself is perpendicular to the place of the orbit. The position vector $\vec{r}$ lies in the same plane. Thus, $\vec{A}$ must lie in the orbital plane. For convenience, the counter-clockwise motion of the electron is constrained in the orbit on the xy-plane with x-axis along the major axis and y-axis along the minor axis. The components of $\vec{A}$ along three orthogonal directions are respectively

$$A_x = p_y L - x/r \quad , \quad A_y = -p_x L - y/r \text{ and } A_z = 0 \qquad (88)$$
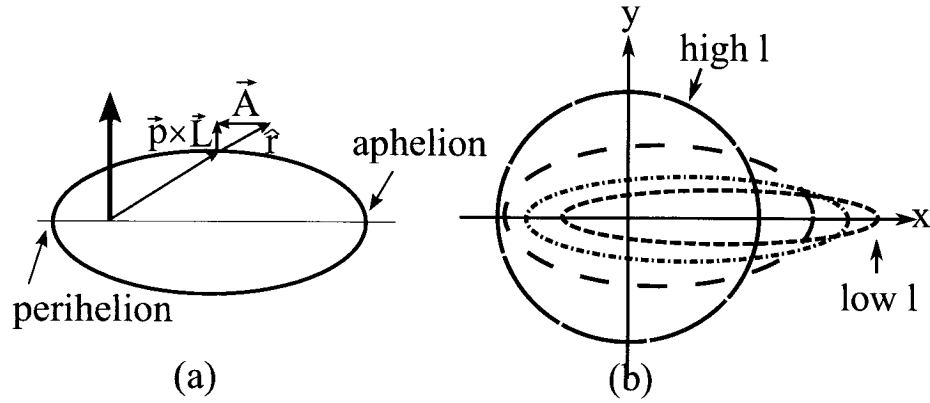
FIG. 11: The classical Rydberg orbits for same energy but different angular momentum.

where $L = L_z$. When the orbiting particle crosses the x-axis, $y = 0$, $p_x = 0$ so $A_y = 0$. Since, $\dot{A} \equiv 0$ at all times, $\vec{A} = A_x \hat{i}$. Therefore, $\vec{A}$ lies along the major axis of the orbit and always directed towards the perihelion of the ellipse as in Fig. 11(a).

Taking the scalar product

$$\vec{A} \cdot \vec{r} = Ar \cos\varphi = L^2 - r \tag{89}$$

Replacing $L^2 \equiv l^2$

$$\frac{l^2}{r} = (1 + A\cos\varphi) \tag{90}$$

and comparing with the equation for a conic section

$$\frac{1}{r} = \frac{1 + \epsilon\cos\varphi}{a(1 - \epsilon^2)} \tag{91}$$

gives $\epsilon = A$ and $\vec{A} \cdot \vec{A}$ leads to

$$A^2 = 2El^2 + 1 \tag{92}$$

which gives

$$\epsilon = \sqrt{1 - \frac{l^2}{n^2}} \tag{93}$$

In atomic units, $E = -1/(2n^2)$. The above Eq. (93) means the orbits are more elliptical for small l, $\epsilon \simeq 1$ (the orbit is essentially a straight line between the nucleus and the outer turning point). The orbits become more and more circular as
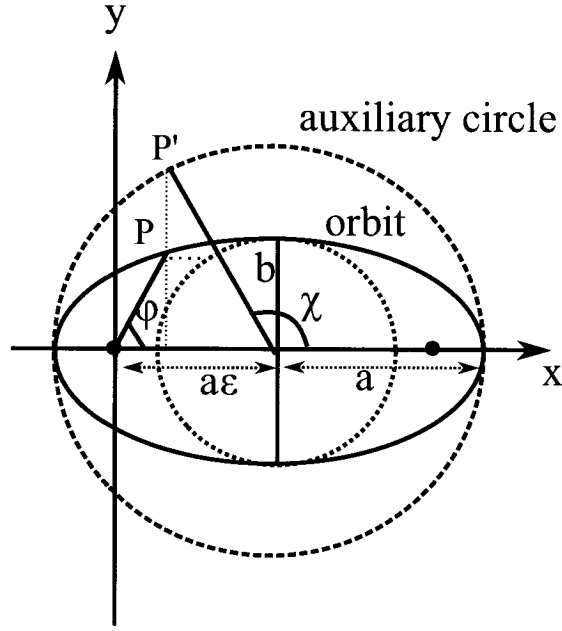
FIG. 12: The relation between eccentric anomaly ξ and true anomaly φ for an elliptical orbit.

l increases, $\epsilon \simeq 0$ as shown in the Fig. 11(b). The position of the orbiting electron at any time can be expressed as

$$x = a(cos\chi + \epsilon) \tag{94}$$

$$y = b\sin\chi, \quad y = a\sqrt{1 - \epsilon^2}\sin\chi \tag{95}$$

with χ is defined as the eccentric anomaly which varies between 0 and 2π over one complete orbital motion. The instantaneous time of the electron can be defined as (assuming the motion starts form aphelion with $\chi = 0$ shown in Fig. 12).

$$t = a^{3/2}(\chi + \epsilon\sin\chi) \tag{96}$$

This gives the Kepler orbital period

$$T = 2\pi a^{3/2} = 2\pi\frac{1}{\sqrt{(2|E|)^3}} = 2\pi n^3 \tag{97}$$

T depends only on the energy of the electron which in turn depends on the major axis a and is independent of the eccentricity ϵ. Therefore, the orbits for a given
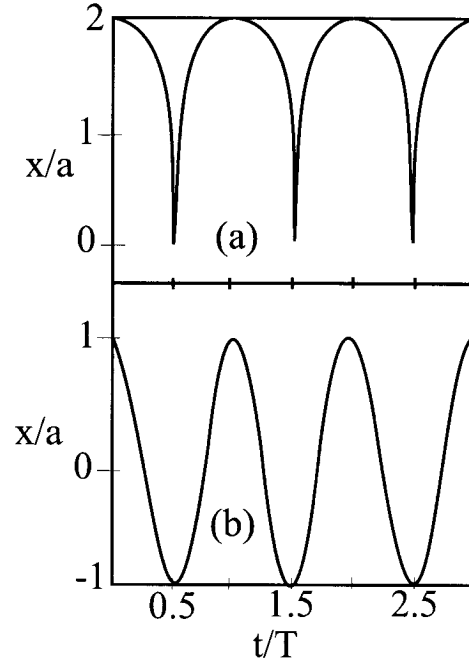
FIG. 13: The plot of scaled x/a versus scaled t/T for (a) low l ($\epsilon \sim 1$) and (b) a high l ($\epsilon \sim 0$).

energy with different l values or eccentricity also have the same orbital period. It also expresses the fact that the Keplerian orbital time scales as n^3. The plot of the scaled x position (x/a) as a function of the scaled time (t/T) is shown in Fig. 13. It also illustrates that for low l ($\epsilon \sim 1$), the electron spends more time far from the core and on one side of the nucleus where the electrons move more slowly and their average charge distribution is therefore more skewed but the electron spends about equal time on both sides of the nucleus for large l with $\epsilon \sim 0$. This suggests the permanent dipole moment associated with the hydrogen atom for small l and the magnitude of the dipole moment decreases with increasing l. Eq. (90) is, therefore, the equation of the Keplerian orbit with A replaced by the eccentricity ϵ given by Eq. (93).
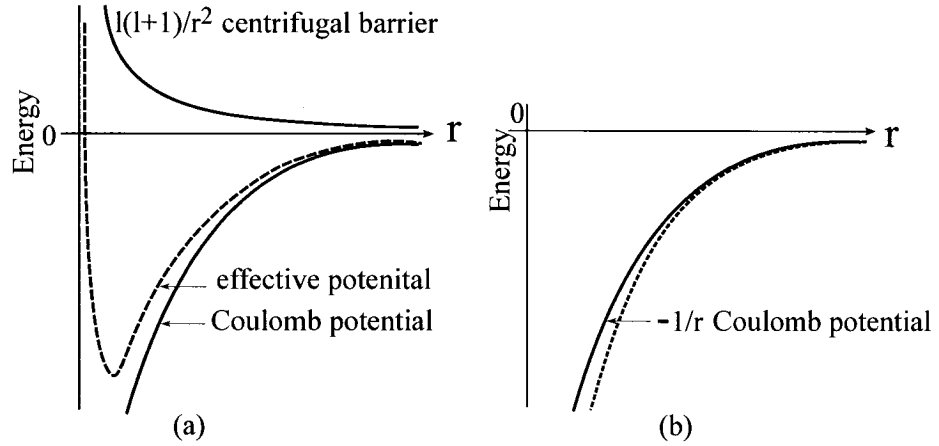
FIG. 14: (a) The potential form for a electron in the Hydrogen atom and (b) the effective potential for a single electron in multi-electron atom.

II.4.4 Quantum defect

Consider a Rydberg electron in a multi-electron atom ($Z > 1$) with orbital angular momentum quantum number l which sees a pure Coulomb potential,

$$V(r) = I_P - \frac{1}{r} + \frac{l(l+1)}{2r^2} \tag{98}$$

with I_P as the ionization limit.

The solution for the radial part of the Schrodinger equation gives the energy eigenvalues, with the term value given by

$$E_n = I_P - \frac{1}{2(n - \delta_l)^2} \tag{99}$$

as shown in Fig. 15.

In multi-level atoms, where the electron has low angular momentum, the excited electron does not always see a pure Coulomb potential because of the presence of the core electrons. The quantum defect parameterizes the interaction of the excited electron with the core. There are two types of interactions, (i) core polarization and (ii) core penetration. It depends explicitly on the orbital angular momentum as shown in Fig. 16. The Rydberg electron experiences an almost hydrogenic Coulomb potential for $r \gg r_{core}$ for a core comprising the nucleus with Z protons shielded by $Z - 1$ electrons. Therefore, the binding energy is nearly hydrogenic. The closest
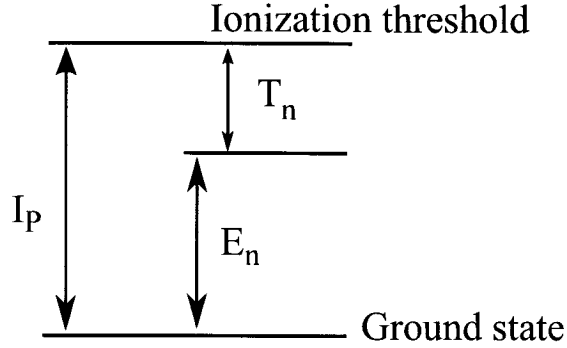
FIG. 15: Term energy

approach between the Rydberg electron and the core depends on the orbital angular momentum of the orbiting electron. For low angular momentum the electron approaches the ionic core close enough such that it can cause core polarization and for very low angular momentum the Rydberg electron even penetrates the core electrons. The Rydberg electron then can feel greater attraction inasmuch as it sees a more positively charged ionic core $Z > 1$. The potential therefore, deviates for small r as in Fig. 14b. In order to take into account the hydrogenic Coulomb potential for $r >> r_{core}$ and a potential substantially different from the pure Coulomb potential for $r \leq r_{core}$, we introduce an entity known as a quantum defect which subsumes the many body effects in the core region.

The potential experienced by the excited electron moving in non-penetrating orbits may be expressed as [40], [19] and [41]

$$V(r) = -\frac{1}{r} + V_{pol} \tag{100}$$

The polarization energy V_{pol} is expressed as

$$V_{pol} = -\frac{\alpha_d}{2}\langle r^{-4}\rangle - \frac{\alpha_q}{2}\langle r^{-6}\rangle \tag{101}$$

with α_d and α_q are the dipole and quadrupole polarizabilities of the ionic core. With the substitution of the values of $\langle r^4 \rangle$ and $\langle r^6 \rangle$ [42] in Eq. (101), we get

$$E_{pol} \cong -\frac{3\alpha_d}{4n^3 l^5} + \frac{35\alpha_q}{16n^3 l^9} \tag{102}$$

The energy for a Rydberg atom for $\delta_l << n$ becomes

$$E_{nl} = -\frac{R_y}{(n-\delta)^2} = \frac{R_y}{n^2} + \frac{2R_y\delta_l}{n^3} \tag{103}$$
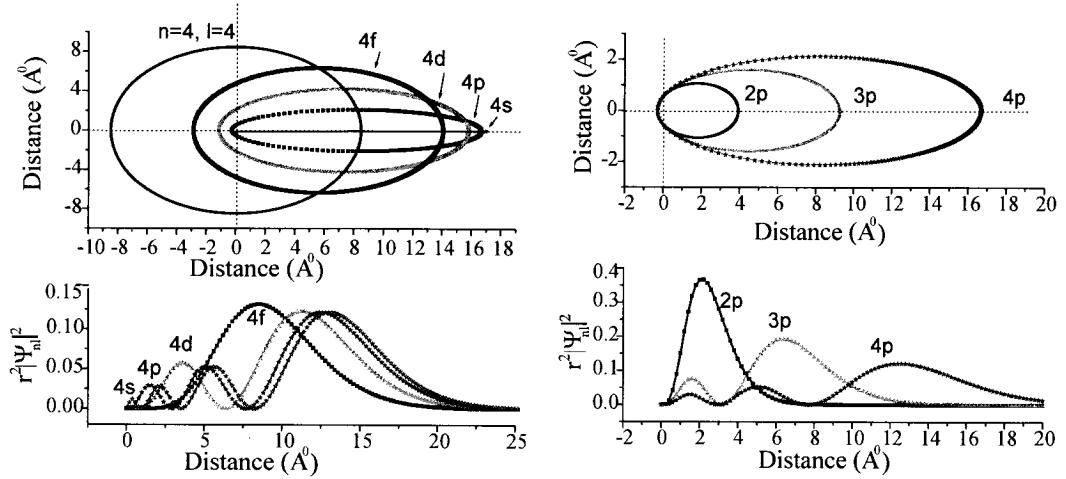
FIG. 16: The classical Rydberg orbits for same n but different l with quantum mehcnically unallowed $l = 4$ is shown for reference along with the quantum treatment below on the left and the classical Rydberg orbits for the same orbital angular momentum but different energy levels and the quantum treatment below on the right.

Then on comparison with Eq. (102) the quantum defect becomes $\delta_l \cong \frac{3\alpha_d}{4l^5} + \frac{35\alpha_q}{16l^9}$ which is a small deviation in energy from hydrogen like behavior due to the interaction of the Rydberg electron with the structured core. Hence, the quantum defect is a function of the orbital momentum l.

II.4.5 Rydberg atoms in an electric field

The study of the effect of an electric field on the highly excited Rydberg atoms has been performed by several groups. The study has been mainly focused on understanding the field ionization properties of high highly excited atoms. In these experiments, the atoms are selectively excited and a pulsed ionization or extraction field is applied at various delays after the photo-excitation. The detected ions or electrons are analyzed as a function of the strength of the field. The interpretation requires the introduction of the dynamic and transient effect depending on the process of the field applied. The wide study on the effect of the constant electric field on the atom during photo-excitation has been done in order to gain more understanding of the behavior of the atoms in the fields.
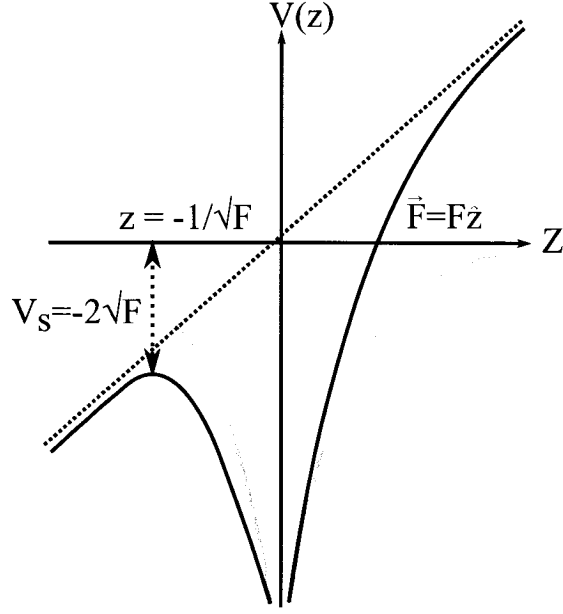
FIG. 17: The resultant potential experienced by an electron in a uniform static electric field applied in the $-z$ direction.

II.4.6 Hydrogen atom in an electric field

The effective potential experienced by an electron in a uniform static electric field applied in the z-direction (z is the quantization axis) is

$$V(r) = -\frac{1}{r} - Fz \tag{104}$$

where F represents the electric field strength. For mathematical convenience, we can assume the atom in a one dimensional potential given by Eq. (104) with core effects and spin neglected [43],

$$V(z) = -\frac{1}{z} - Fz \tag{105}$$

The matrix element in the unperturbed spherical eigenbasis is

$$\langle nlm|Fz|n'l'm'\rangle = (-1)^{l-m}\sqrt{2l+1}\begin{pmatrix} l & 1 & l' \\ -m & 0 & m' \end{pmatrix}\langle nl\|r\|n'l'\rangle \tag{106}$$

where the last term in the parentheses is the Wigner 3-j symbol. The matrix element is non-vanishing for $m' = m$ and $\langle nl\|r\|n'l'\rangle$ (i.e., the states must have opposite parity
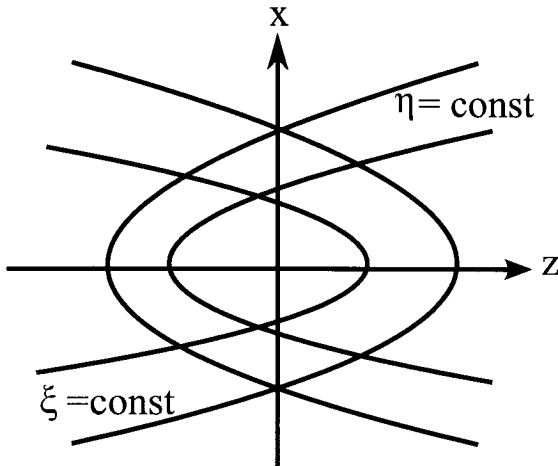
FIG. 18: Parabolic $\xi = const.$ and $\eta = const.$ with z-axis as axis of rotation.

such that and $l' = l \pm l$). Hence, m remains a good quantum number but l is not a good quantum number. Thus, the field lifts the degeneracy of lm states of n.

The external field deforms the Coulomb potential and results in a saddle point located at $z = 1/\sqrt{F}$ and the potential at this point is $V_s = -2\sqrt{F}$ as shown in Fig. 17. According to this saddle-point model, the states with the energy $E_n = -\frac{1}{2n^2}$ smaller than V_s are stable and those states with $E_n \geq -2\sqrt{F}$ (ie, the states lying above the saddle-point) ionize.

Now, if we ignore the Stark shift and equate the energy value at the saddle point with the binding energy we get,

$$-2\sqrt{F} = -\frac{1}{2n^{*2}}$$
$$F = \frac{1}{16n^{*4}} \tag{107}$$

where $n^* = n - \delta_l$ is the the effective quantum number. Eq. (107) corresponds to the classical threshold field required for the ionization. This model provides a crude estimate for the onset of ionization. The two factors namely, Stark shifts and the spatial distributions of electron wave functions deviates this rule. The explanation on the latter case follows with the localization of electrons on the high and low potential sides of the deformed potential which is shown in Fig. 19. The extreme red-shifted state is confined in the region close to the saddle point and the energy of such a state

in the field is given by

$$E(n, F) = -\frac{1}{2n^2} - \frac{3}{2}n(n-1)F \tag{108}$$

since, $n - 1 \approx n$ and equating with Eq. (107) yields the mimimum field for the ionization of the extreme red state,

$$F = \frac{1}{9n^{*4}} \tag{109}$$

And, at these fields, the blue states still remian stable.

The static electric field breaks the spherical symmetry of the Coulomb field, and the angular momentum l does not remain a good quantum number, since the angular momentum does not commute with the total Hamiltonian.

$$\hat{H} = \hat{H}_0 + \hat{H}_s \tag{110}$$

where $\hat{H}_0$ is the atomic Hamiltonian, $P^2/2m + V(r)$ and $\hat{H}_s$ is the Stark energy.

$$[\hat{H}_s, \hat{L}^2] \neq 0 \quad, \quad [\hat{H}_s, \hat{L}_z] = 0 \tag{111}$$

The Schrödinger equation is solvable by separation of the variables in spherical coordinates for the pure Coulomb potential. However, the introduction of a uniform electric field along the z-axis destroys the spherical symmetry of the potential. However, in parabolic coordinates ξ, η, φ it is still possible to decouple the Schrödinger equation into an ordinary differential equation even in the presence of a static external electric field. The parabolic coordinates ξ, η, φ are related to Cartesian coordinates as indicated in Fig. 18

$$x = \sqrt{\xi\eta}\cos\varphi, \quad y = \sqrt{\xi\eta}\sin\varphi, \quad z = \frac{1}{2}(\xi - \eta) \tag{112}$$

The electric field applied in the z direction does not disturb the rotational symmetry around the z-axis, hence,

$$\xi = r(1 + \cos\cos\theta) = r + z, \quad \eta = r(1 - \cos\theta) = r - z, \quad \varphi = \varphi \tag{113}$$

with

$$d\vec{r} = \frac{(\xi + \eta)}{4}d\xi d\eta d\varphi$$

where $r = \sqrt{x^2 + y^2 + z^2}$, θ, φ are the spherical coordinates.

The Coulomb potential in parabolic coordinates becomes $V(\xi, \eta) = -\frac{2}{\xi + \eta}$. In terms of these coordinates, the laplacian takes the form

$$\Delta = \frac{4}{\xi + \eta} \frac{\partial}{\partial \xi} \left(\xi \frac{\partial}{\partial \xi} \right) + \frac{4}{\xi + \eta} \frac{\partial}{\partial \eta} \left(\eta \frac{\partial}{\partial \eta} \right) + \frac{1}{\xi \eta} \frac{\partial^2}{\partial \varphi^2} \tag{114}$$

The Hamiltonian operator for the nonrelativistic isolated hydrogen atom in the static electric field is

$$\hat{H} = -\frac{1}{2} \Delta - \frac{1}{r} + Fz \tag{115}$$

and the Schrödinger equation becomes

$$\left(-\frac{1}{2} \right) \frac{4}{\xi + \eta} \left[\frac{\partial}{\partial \xi} \xi \frac{\partial \psi}{\partial \xi} + \frac{\partial}{\partial \eta} \eta \frac{\partial \psi}{\partial \eta} + \frac{\xi + \eta}{4 \xi \eta} \frac{\partial^2 \psi}{\partial \varphi^2} \right] - \frac{2 \psi}{\xi + \eta} + \frac{F(\xi - \eta) \psi}{2} = E \psi \tag{116}$$

The factorization of the solutions of the Schrödinger equation as $\psi(\xi, \eta, \varphi)$ into $f(\xi) g(\eta) W(\varphi)$. Since the equation in φ is identical to that in the spherical coordinate system, Eq. (116) becomes

$$\left[\frac{\partial}{\partial \xi} \xi \frac{\partial}{\partial \xi} + \left(\frac{|E| \xi}{2} - \frac{m^2}{4 \xi} - \frac{F \xi^2}{4} + Z_1 \right) \right] f(\xi) = 0 \tag{117}$$

and

$$\left[\frac{\partial}{\partial \eta} \eta \frac{\partial}{\partial \eta} + \left(\frac{|E| \eta}{2} - \frac{m^2}{4 \xi} + \frac{F \eta^2}{4} + Z_2 \right) \right] g(\eta) = 0 \tag{118}$$

where the eigenvalues Z_1 and Z_2 are the constants that satisfy $Z_1 + Z_2 = Z$ with $Z = 1$ for the hydrogen atom. First, it will be very convenient to solve the problems for the hydrogenic levels in the field by solving it in zero field in parabolic coordinates and then using perturbation theory [19]. Using $F = 0$, $x = \epsilon \xi$ and $\epsilon^2 = 2|E|$ and assuming the solution of the form

$$f(\xi) = e^{-\xi/2} \xi^{|m|/2} L(\xi) \tag{119}$$

the Eq. (117) becomes

$$x L''(x) + [|m| + 1 - x] L'(x) + \left[\frac{Z_1}{\epsilon} - \frac{|m| + 1}{2} \right] L(x) = 0 \tag{120}$$

which is identical to the radial part of the Schrödinger equation of the form

$$x L''(x) + [2(L + 1) - x] L'(x) + \left[\frac{Z}{\epsilon} - (L + 1) \right] L(x) = 0 \tag{121}$$

with the solution given by the associated Laguerre polynomials,

$$L_q^j(x) = L_{N+L}^{2L+1}(x) \tag{122}$$

The normalized radial wavefunction is given by

$$R(x) = C_{NL} \exp{-x/2} x^L L_{N+L}^{2L+1}(x) \tag{123}$$

where

$$C_{NL} = -\left[\frac{4Z^3}{N^4} \frac{(N-L-1)!}{((N+L)!)^3)}\right]^{1/2} \tag{124}$$

is the normalization constant.

$$L(x) = L_{n_1+M}^M(x) \tag{125}$$

where

$$n_1 = \frac{Z_1}{\epsilon} - \frac{1}{2}(|m|+1) \tag{126}$$

Similarly, the Eq. (118) gives

$$n_2 = \frac{Z_2}{\epsilon} - \frac{1}{2}(|m|+1) \tag{127}$$

Eqns.(126) and (127) lead to

$$n_1 + n_2 + |m| + 1 = \frac{Z_1 + Z_2}{\epsilon} = n \tag{128}$$

For a given n, the number $|m|$ can take values 0, 1, 2, $\cdots (n-1)$. For each $|m|$ the number n_1 and n_2 can take values, 0, 2, $\cdots$, $n - |m| - 1$. and the corresponding unnormalized wavefuction $\psi(\xi, \eta, \varphi)$ can be expressed as

$$\psi_{n_1 n_2 nm} = N exp\left[-\frac{\epsilon(\xi+\eta)}{2}\right](\xi\eta)^{|m|/2} L_{n_1+|m|}^{|m|}(\epsilon\xi) L_{n_2+|m|}^{|m|}(\epsilon\eta) \exp{im\varphi} \tag{129}$$

The resulting eigenenergies depend on the principal quantum number n, the magnetic quantum number m, and two new quantum numbers n_1 and n_2 that give the number of the nodes in the wavefuntions $f(\xi)$ and $g(\eta)$. In the presence of the electric field $F \neq 0$, perturbation theory has been used extensively to find the solution. The separation parameters Z_1 and Z_2 are expanded in the successive powers of the field F.

$$Z_1 = Z_1^{(0)} + FZ_1^{(1)} + F^2 Z_1^{(2)} + \cdots$$
$$Z_2 = Z_2^{(0)} + FZ_2^{(1)} + F^2 Z_2^{(2)} + \cdots \tag{130}$$
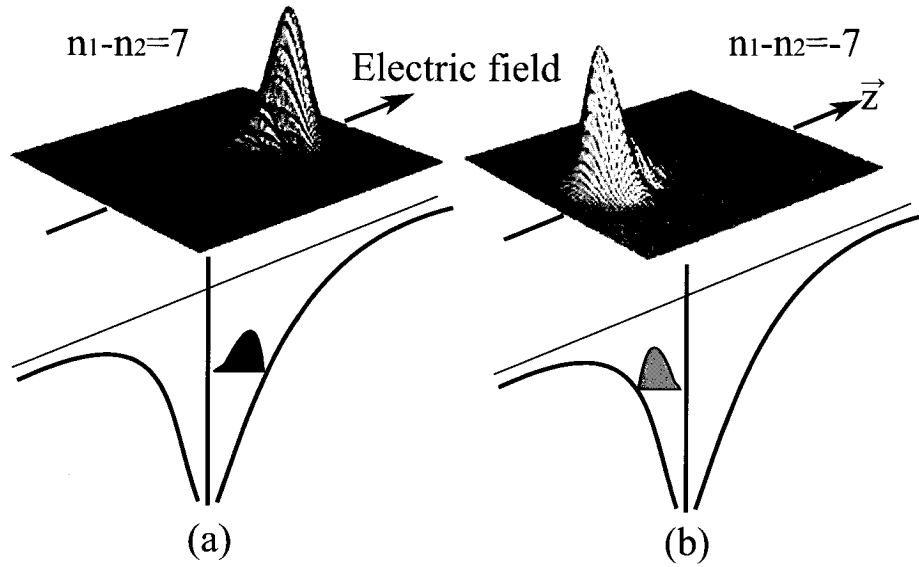
FIG. 19: The charge distribution for Hydrogen with parabolic quantum numbers $n = 8$, $m = 0$ are shown for (a) $n_1 - n_2 = 7$ and (b) $n_1 - n_2 = -7$ [44].

Eqns. (117) and (118) can be used to determine the separation constants Z_1 and Z_2 as a function of binding energy E and the field F with the constraint on the separation constants as $Z_1 + Z_2 = 1$. The correction terms to the first, second and third order have been respectively obtained by Schrödinger [45], Epistein [46] and, Doi et. al. [47]. The degenerate energy levels of the zero-field hydrogenic system fans out into $n - m$ levels in the presence of a uniform static external electric field. To second order, the Stark energy for a given n_1, n_2, m state is given by

$$E(n, F) = E^{(0)} + E^{(1)} + E^{(2)} \tag{131}$$

$$E(n, F) = -\frac{1}{2n^2} + \frac{3}{2}n(n_1 - n_2)F$$
$$- \frac{1}{16}n^4 \left[17n^2 - 3(n_1 - n_2)^2 + 9m^2 + 19 \right] F^2 \tag{132}$$

The first order correction term can be considered as the energy shifts associated with the permanent dipole in a static electric field given by,

$$E^{(1)} = \frac{3}{2}n(n_1 - n_2)F$$
$$= \frac{3}{2}nkF \tag{133}$$

where $k = (n_1 - n_2)$ is the state index and is sometimes referred to as the electric quantum number. The permanent dipole moment is given by $\frac{3}{2}n(n_1 - n_2)$ and the second order correction in energy depends on $|m|$. It can be written in terms of Runge-Lenz vector [39]. The dipole moment points towards the perihelion, in the direction of $\vec{A}$.

$$\langle \vec{d} \rangle = \langle r \cos\varphi \rangle (\vec{A}/|\vec{A}|) \tag{134}$$

$$|\langle d \rangle| = \frac{1}{T}\int_0^T r\cos\varphi \, dt = \frac{1}{T}\int_0^T r\cos\varphi \frac{dt}{d\varphi}d\varphi \tag{135}$$

using the conservation of angular momentum, $r^2 d\varphi/dt = l$, the magnitude of the dipole moment becomes

$$\frac{1}{T}\int_{-\pi}^{\pi} \frac{r^3\cos\varphi}{l}d\varphi = \frac{l^5}{2\pi n^3}\int_{-\pi}^{\pi}\frac{\cos\varphi}{(1+\epsilon\cos\varphi)^3}d\varphi$$

$$= \frac{3}{2}n^2\epsilon = \frac{3}{2}n^2\sqrt{1 - \frac{l^2}{n^2}} \tag{136}$$

$$\langle \vec{d} \rangle = \frac{3}{2}n^2\vec{A} \tag{137}$$

where $\vec{d}$ is the electric dipole moment and the potential energy of the dipole in the electric field is given by

$$\Delta E = -\vec{d}\cdot\vec{F} = -\frac{3}{2}n^2 A_z F \tag{138}$$

with the field $\vec{F}$ is in the z-direction and the field is small so it does not distort the Keplerian orbit significantly.

The charge distributions for the hydrogen atom with the parabolic quantum numbers $n = 8$, $m = 0$ and $n_1 - n_2 = 7$ and $n_1 - n_2 = -7$ are shown in the Fig. 19. The direction of the dipole moment is parallel to the direction of the electric field for the red state with $n_1 - n_2 = -7$. The electronic charge distribution is localized at the saddle-point whereas the blue state has the charge distribution localized to the other side with high potential barrier.

II.5 ULTRACOLD NEUTRAL PLASMAS

We now turn our attention to a discussion of ultracold neutral plasmas. In order to fully understand the dynamics of ultracold plasmas, it is important to understand the interactions between electrons, ions, and ultracold Rydberg atoms. Plasmas are ubiquitous and their temperature ranges from $10^{16}K$ in the magnetosphere of a pulsar to $300K$ in the earth's ionosphere [10]. A plasma is a system of ionized particles which can exhibit collective behavior. The collective behavior arises due to the electric and magnetic fields as the result of the motion of charged particles. A usual requirement for a plasma is that the Debye length needs to be smaller than the system size ($\lambda_D \ll \sigma$), where σ is the size of the system. The Debye length is the fundamental parameter in plasma. It is the distance over which the distribution of charged particles of the plasma shields any external electric fields or the field due to individual plasma particles; it is given by

$$\lambda_D = \sqrt{\frac{\epsilon K_B T_e}{n_e e^2}} \tag{139}$$

Plasmas with a temperature as low as a few mK have been created in the lab after photoionization of ultracold atoms or photo-excitation to high-n Rydberg states located a few wavenumbers in energy below the ionization threshold of the ultracold atoms. The Coulomb coupling parameter is another important parameter of a plasma and is defined as the ratio of Coulomb interaction energy to the thermal energy:

$$\Gamma_\alpha = \frac{e^2}{4\pi\epsilon_0 a} \frac{1}{K_B T_\alpha} \tag{140}$$

where $a = (3/4\pi n)$ is the Wigner-Seitz radius, n is the density of component (α) of plasma and ϵ_0 is the permittivity of vacuum. The plasma becomes strongly coupled for $\Gamma_\alpha \geq 1$ (if the interaction energy is larger than the thermal energy) and then the usual hydrodynamic equations of motion and collective mode dispersion relations are no longer valid. Strongly coupled plasmas can exhibit short and long range coupling among its constituents. Typical examples of such strongly coupled plasma ocuring naturally are in white dwarf, neutron stars and the inside of Jovian planets.

The generation of strongly coupled plasma in the laboratory is challenging. It is obvious from Eq. (140) that a high density and/or low temperature is required. A simple model consists of the photoionization of the atoms in the MOT with the photon energy ($h\nu > I_P$). The ion and electron obey energy conservation and the
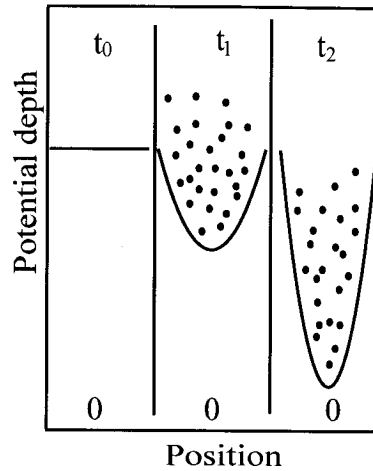
FIG. 20: The potential energy as seen by the electrons due to the gaussian distribution of ions after the photoionization in plasma.

excess photon energy is

$$\Delta E \equiv h\nu - I_p = \frac{p_i^2}{2m_i} + \frac{p_e^2}{2m_e} \tag{141}$$

where I_p is the ionization threshold. Most of the excess energy is carried away by the electrons because of the very small electron to ion mass ratio $(m_e/m_i \ll 1)$,

$$
\begin{aligned}
E_e &= \frac{m_i}{M}\Delta E \\
&\approx \Delta E
\end{aligned}
\tag{142}
$$

Now according to a Maxwell-Boltzmann distribution,

$$T_e = \frac{2}{3}\left(\frac{\Delta E}{K_B}\right) = \frac{2}{3}\left(\frac{E_e}{K_B}\right) \tag{143}$$

where T_e is the temperature of the electron. Within the few nanoseconds after photoionization the thermalization of electron takes places while the ions are essentially immobile. The distribution of the ions is approximately described by a Gaussian profile, associated with the initial distribution of neutral atoms in the MOT,

$$n_i = n_0 e^{-(r/\sigma)^2} \tag{144}$$

A few electrons, with a relatively large thermal energy compared to the ions, escape the plasma soon after photo-ionization. The remaining electrons are then
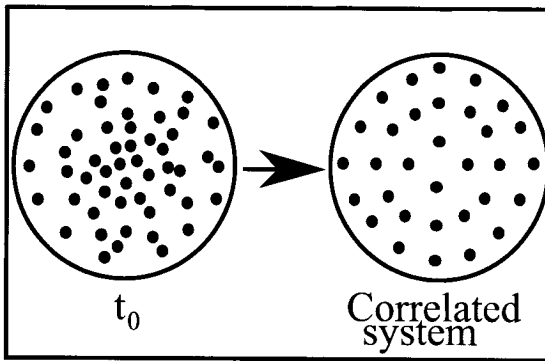
FIG. 21: The spatially uncorrelated systems of ions after photoionization and transformation to the correlated state with minimum potential energy of the system.

trapped by the potential of the residual ions, leaving the number of ions and electrons approximately the same in the inner region of the plasma. What remains is a quasi-neutral plasma.

$$U_0 = \sqrt{\frac{2}{\pi}} \frac{e^2}{4\pi\epsilon_0\sigma} \tag{145}$$

The more electrons which escape, the deeper the trapping potential and the remaining electrons are finally trapped with an electron energy as shown in the Fig. 20

$$E_e \leq N_i U_0 \tag{146}$$

with the total number of ions N_i.

II.5.1 Ion dynamics

A charged particle in the presence of the other charged particle oscillates about its equilibrium position [48] in an ultracold or strongly coupled regime. Ultracold ions are created with negligible kinetic energy, they assume the distribution of the neutral atoms from which they were formed and hence are initially spatially uncorrelated. As a result, they possesses a higher Coulomb potential energy compared to the regular lattice of the ground state of the system [49]. As the ions equilibrate and correlations develop, the potential energy is converted to kinetic energy. The process is called disorder-induced heating (DIH), or correlation heating as shown in Fig. 21. The ion
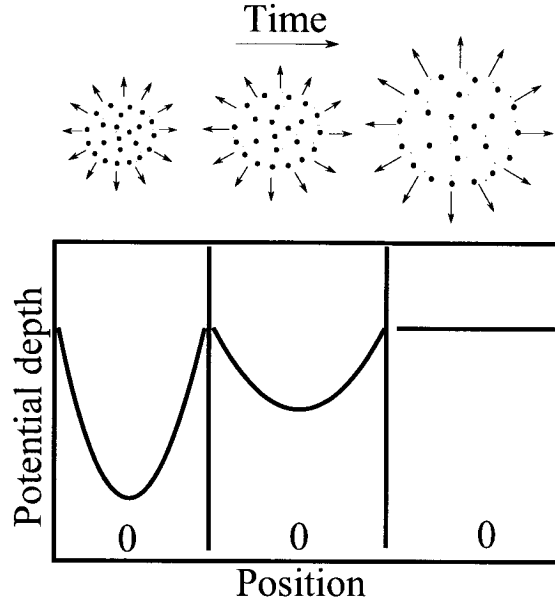
FIG. 22: The expansion of ultracold quasi-neutral plasma due to thermal energy of the electrons.

heating occurs in the time scale of the inverse ionic plasma frequency which is on the order of a few 100 nanoseconds,

$$\omega_i^{-1} = \sqrt{\frac{m_i \epsilon_0}{n_i e^2}} \tag{147}$$

II.5.2 Plasma expansion

The ultracold neutral plasma expands radially due to the thermal pressure of the electrons. The electrons oscillate with a frequency $\omega_e = (1/2\pi)\sqrt{e^2 n_e/\epsilon m_e}$ which is a function of the density of the electrons. The electrons have high kinetic energy, they have a tendency to move away from the plasma cloud and they are restored by the Coulomb force due to the ions in the cloud. In the process, the ions experience a radial recoil force in the outward direction which is manifested by the radially outward expansion of the plasma as shown in Fig. 22. This results in a decrease in potential well depth and more electrons can escape the expanding cloud.

Within a few tens of microseconds after photoionization, the thermal energy of ions becomes negligible compared to their expansion energy. Then the ion expands at the expense of the electrons thermal energy.

II.5.3 Ultracold plasmas and ultracold Rydberg gases

Dense Rydberg gases are closely related to ultracold plasmas as these systems can spontaneously evolve from one to the other. Even if initially only ions are produced in the plasma, collisions between the ion and two electrons can result in the formation of a highly-excited, bound (Rydberg) atom. The binding energy is taken up by the third electron. This process is known as "three-body recombination" (TBR) and plays a very important role in the time evolution of ultracold plasmas. In TBR we have, $(e^- + e^- + A^+ \longrightarrow e^- + A^*)$. Of course, these newly formed Rydberg atoms can interact with electrons, black-body radiation and other ultracold Rydberg atoms. As a result, and depending on the interaction, they may be re-ionized or they may change state. State changing collisions can include placing the Rydberg electron in an even more tightly bound state.

Along these same lines, if the initial excitation by the laser is not to above the ionization threshold but rather to below it, then an ensemble of ultracold Rydberg atoms will be formed. By the same processes noted above, these atoms can be ionized and hence if the density is high enough, or some other "seeding mechanism" is in place, this collection of ultracold Rydberg atoms can spontaneously evolve into an ultracold plasma [18]. Rydberg atoms are large and can interact strongly via dipole-dipole or van der Waals interactions. These interactions can lead to collisions which result in ionization. Even if a small fraction of highly excited Rydberg atoms quickly ionize, the resulting net positive potential of the cloud forms a trap for the electrons. The trapped electrons vibrate significantly within the cloud and undergo electron-Rydberg collisions which can result in a state change $(e^- + A^*(n,l) \longrightarrow e^- + A^*(n',l'))$ or ionization.

A number of groups have used various techniques to probe the ultracold plasma dynamics. For ions with a convenient optical transition (for example Ca^+ or Sr^+) optical imaging techniques have been used. More commonly, it is ion or electron detection which is used to probe the plasma, especially after application of radio frequency fields (for example to excite plasma oscillations) or pulsed fields for ionization (which is a state-selective read out method). It should be noted that another way to probe the system is through spectroscopy of the Rydberg atoms. Here, the observed Stark shift, especially as a function of time, can be used to characterize the electric fields present in the plasma / Rydberg gas mixture.

II.6   AUTO-IONIZING STATES IN ARGON AND THE CREATION OF ZEKE STATES

The process of photo-excitation can only excite an initially low angular momentum electron to states with high n but low l like s, p or d states. If these states lie in an auto-ionizing continuum, they have a greater probability to decay, autoionize or predissociate than higher angular momentum states because they interact with the core.

An example of autoionizing states is atomic states with at least two excited electrons such that the decaying of one electron can provide enough energy for the other excited electron to ionize. Another example is a discrete state which lies above an ionization continuum. Autoionization resonances are due to coupling between the continuum and resonant Rydberg states. In argon the autoionizing states are Rydberg states converging to an ionization limit that lies above the lower ionization threshold. Autoionization involves the nonradiative process that results in the formation of a state of the ion that lies lower than the Rydberg series limit of the autoionizing state and the ejected electron which carries the excess energy. Depending on whether the system is atomic or molecular, the excess energy in the ejected electron can come from the conversion of

- rotational energy

- vibrational energy

- spin-orbit energy

- electronic energy

The first two types of interaction are peculiar to molecules and the last two appear in molecules and atoms. In the case of argon, the autoionizing states are the Rydberg states converging to the $^2P_{1/2}$ ionization limit and lying above the ionization threshold of $^2P_{3/2}$ ionic core state and are subject to radiationless decay into the $^2P_{3/2}$ continuum via the scattering process that involves relaxation of the spin-orbit state of the ionic core. The core looses spin-orbit energy and the electron is liberated. The autoionizing Rydberg series of a rare gases have been the subject of intense investigation. The dipole-allowed transitions from the excited states in the experiment to be reported here, the $(^2P^0_{1/2})4p^2[3/2]_2$ to Rydberg region below the ionization threshold

for $^2P_{1/2}$ spin-orbit configuration, has most of the intensity in the nd' series coupled to the ionization continuum of the $^2P_{1/2}$ spin-orbit configuration of the core [50]. The lifetimes for these nd' series in Ar, Kr and Xe scale as $\tau_n = 1/\Gamma_n \approx 2\pi n^3$ a.u, close to the Kepler period of the Rydberg electron. They are $\tau_n(s)/n^3 = 1.7 \times 10^{-16}$, 1.8×10^{-16} and 1.5×10^{-16} in Ar, Kr and Xe respectively. The optically accessible states for $n \approx 90$ in Ar have lifetimes of $3 - 50$ ns. However, the states a few tens of wavenumbers below the ionization threshold have been found in experiments to have lifetimes of the order of tens of microseconds, defying the n^3 scaling of Rydberg state lifetimes predicted by the theory.

The discovery of these long lifetime Rydberg states was unexpected, but the underlying explanation was quickly proposed by Chupka [24] who also explained the breakdown of n^3 scaling at high n. The dipole allowed single photon transitions can excite the atom from the ground state or low lying state with low l and low m to arbitrarily high n with low l and low m. The quantum numbers n, l and m are good quantum numbers only for a purely spherical Coulomb potential. Stray electric fields, however, are ubiquitous and an intentional field can be applied too . The Stark effect due to small homogeneous electric field mixes the states of different l and same m according to the selection rule $\Delta l = \pm 1$. In the presence of an inhomogeneous electric field due to the space charge formed during the process of photo-excitation and the fast autoionization, the spherical *and* cylindrical symmetry can be broken. If cylindrical symmetry is broken, m does not remain a good quantum number either. The further dilution of the low l occurs due to the mixing between the optically accessible state of low m to the "dark" higher m states. These states with high $l \geq 3$ do not interact with the core. The dynamical reason is that they are prevented from such coupling due to the large centrifugal barrier, eccentricity $\epsilon \approx 0$ (circular orbits). This dilution of the optical accessible low l states leads to the increase in the lifetime by the factor of n. The further mixing of the m states increases the lifetime by the factor of n. Since the complete degeneracy of the hydrogenic state is n^2, in the limit of complete mixing, the lifetime scales as $\approx n^5$ [51].

II.6.1 Classical theory of l-mixing

The orbital angular momentum l is not conserved in the presence of external stray or applied electric fields. In order to find the effect of the external electric field on the Keplerian orbit of the electron we write the equation of motion for $\vec{L}$ and $\vec{A}$ and
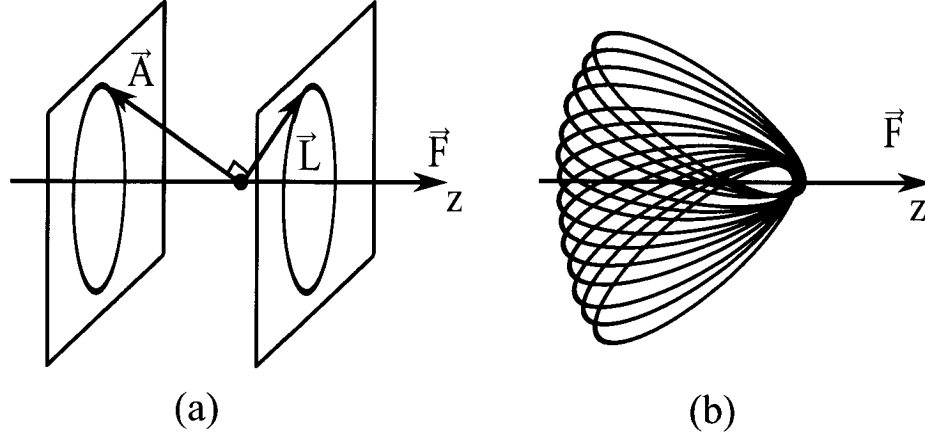
FIG. 23: (a) The precession of the Lenz vector $\vec{A}$ and orbital angular momentum vector $\vec{L}$ on the respective planes perpendicular to the direction of the external electric field and (b) the corresponding precession of the electrons orbit analogous to precession of perehillion of the planets.

average them over a Kepler period.

$$\langle \dot{\vec{A}} \rangle = \frac{3}{2}(\langle \vec{L} \rangle \times \vec{F})$$

$$\langle \dot{\vec{L}} \rangle = = \frac{3n^2}{2}(\langle \vec{A} \rangle \times \vec{F})$$

(148)

The dynamical quantities are averaged over the Keplerian period to remove the small changes due to the fluctuations of the inner electrons parameters in multi-electron atoms. The coupled equations for $\dot{\vec{A}}$ and $\dot{\vec{L}}$ can be uncoupled as

$$\langle \ddot{\vec{A}} \rangle = \frac{3}{2}[(\langle \dot{\vec{L}} \rangle \times \vec{F}) + (\langle \vec{L} \rangle \times \dot{\vec{F}})]$$

$$= \frac{3}{2}(\langle \dot{\vec{L}} \rangle \times \vec{F})$$

(149)

and Eq. (149) is solved for a uniform static electric field $\vec{F} = F\hat{k}$. We have $\dot{\vec{A}}_z = 0$

$$\langle \ddot{\vec{A}} \rangle = \left(\frac{3}{2}n\right)^2 F^2 \langle \vec{A} \rangle$$

(150)

$$\langle \ddot{\vec{A}} \rangle = \left(\frac{3}{2}n\right)^2 F^2(\langle A_x \rangle \hat{i} + \langle A_y \rangle \hat{j})$$

(151)

The x- and y- components of $\langle \vec{A} \rangle_i$ are therefore

$$\langle \ddot{A}_i \rangle = -(\frac{3}{2}nF)^2 \langle A_i \rangle \tag{152}$$

where $i = x$ or y.

The analytic solution to Eq. (152) is

$$\langle A_x \rangle = \langle A_{x0} \rangle \cos(\omega_s t) \text{ and } \langle A_y \rangle = \langle A_{y0} \rangle \sin(\omega_s t) \tag{153}$$

with $\langle A_y \rangle (t = 0) = 0$ and $\langle A_{x0} \rangle$ and $\langle A_{y0} \rangle$ are constants, $\omega_s = \frac{3}{2}nF$ is the Stark frequency in a.u. and F is the external field in a.u. ($1 \, a.u \simeq 5.14 \times 10^9 V/cm$). This also allows us to interpret the orbital deformation in the trajectory as it satisfies

$$\frac{\langle A_x \rangle^2}{\langle A_{x0} \rangle^2} + \frac{\langle A_y \rangle^2}{\langle A_{y0} \rangle^2} = 1 \tag{154}$$

Hence, the locus of the tip of the Lenz vector $\langle \vec{A} \rangle$ describes the ellipse on the plane perpendicular to the applied electric field $\vec{F}$ and the precessional frequency is given by the Stark frequency. The similar relations can be derived for the orbital angular momentum vector $\langle \vec{L} \rangle$. However, they still meet the requirement $\langle \vec{A} \rangle \cdot \langle \vec{L} \rangle = 0$ with $\langle \vec{A} \rangle$ always in the plane of the orbit and $\langle \vec{L} \rangle$, perpendicular to the plane of orbit. It also traces an ellipse synchronously with the Lenz vector $\langle \vec{A} \rangle$ with the same direction of precession as shown in Fig. 23.

These solutions to $\langle \vec{A} \rangle$ and $\langle \vec{L} \rangle$ implies the precession of the orbital plane about the external applied field along with the pulsation in the eccentricity of the orbit with frequency equal to $2\omega_s$. Thus, the orbital angular momentum l oscillates between the minimum and the maximal value (which depends on m_l and can be as high as $(n-1)$) in a periodic motion (which to the first order, is harmonic with the frequency $3nF$ in a.u). However note that the z-component of $\vec{A}$ and $\vec{L}$ remains constant. For small field, the Stark frequency is usually much smaller than the Kepler frequency $\omega_K \sim 2\pi n^3$. Therefore, the electron revolves around a Kepler orbit several times before the angular momentum of the electron is modified significantly by the external field. On the scale of the orbital period, the core-interaction time is instantaneous as the velocity of the electron is highest near the core. Only those electrons with the initial values of the position close to the core and heading towards it will manifest close interaction with the core. For the other initial positions on the electron orbit, the close encounter between the electron and the core depends on the orbital frequency of the electron and the frequency of the oscillation of l.

The closest approach of the electron to the core is $n^2(1 - l(l + 1)/n^2)^{1/2}$ which can be well approximated to $l(l + 1)/2$ a.u.. Thus, l of the electron does not need to be very high in order to avoid the coupling with the ionic core. A simple formulation can assume the coupling to be effective for $l < l_0$, where $l_0 \ll n$. The fraction of the time during which $l < l_0$ is l_0/n,

$$T_{l < l_0} = \frac{l_0}{n} \frac{1}{3n^2 F} \tag{155}$$

The assumption that the oscillation of the orbital angular momentum l is faster than the orbital motion has been made. The electron returns to the core with the frequency n^{-3} in a.u. The number of close encounters between the electron and the ionic core is

$$\frac{l_0}{3n^5 F} / \text{oscillation of } 1 = \omega \frac{l_0}{3n^5} F = \frac{l_0}{n^4} / \text{unit time} \tag{156}$$

Thus, the frequency of the close coupling between the electron and the ionic core is reduced by the factor l_0/n [52] as compared to the field free case.

II.6.2 Quantal treatment of l-mixing

In the presence of the uniform field, the total Hamiltonian $\hat{H} = \hat{H}_0 + Fz$ is not diagonal in the eigenbasis of spherical polar coordinates. The diagonal elements give the eigenenergies whereas the non-diagonal elements $\langle n', l', m' | Fz | n, l, m \rangle$ gives the coupling between two states due to the perturbation Fz. These elements can be written as the product of the radial and angular part $F \langle n', l' | r | n, l \rangle \langle l', m' | cos\theta | l, m \rangle$. This implies the selection rules

$$\Delta m = 0, \quad \Delta l = \pm 1, \quad \Delta n = 0, \pm 1, \pm 2, \cdots \tag{157}$$

The diagonalization of the total Hamiltonian results in the Stark states. In Eq. (132) we have the first and second order corrections to the energy levels in the presence of the uniform electric field F. The first correction can be written as

$$\langle n n_1 n_2 m | \vec{F} \cdot r\hat{z} | n' n_1' n_2' m' \rangle = \frac{3}{2} n(n_1 - n_2) F \tag{158}$$

For small fields the second order correction in the eigenenergy is negligible as compared to the first order correction which is given by Eq.(158). The perturbation leads to the linear splitting of degenerate levels $|n, l, m\rangle$ as shown in Fig. 24. The relation among the quantum number in the parabolic coordinate system n_1, n_2, n
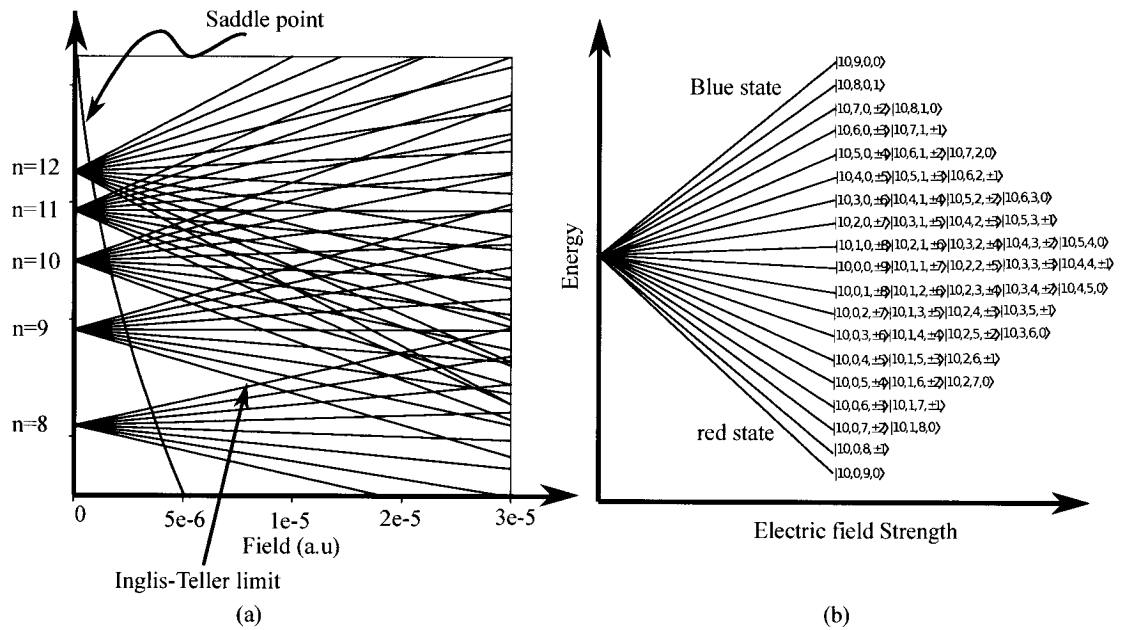
FIG. 24: (a) Stark structure and field ionization properties of different states of Hydrogen atom. The Zero field manifolds are characterized by the principal quantum number n ranging from $n = 8$ to $n = 14$. The electric field is shown in $a.u$ where 1 a.u $\simeq 5.14 \times 10^9$ V/cm [19], (b) the splitting of the degenerate hydrogenic state $n = 10$ in the presence of the electric field and the corresponding parabolic/Stark states $|n, n_1, n_2, |m|\rangle$.

and m is $n_1 + n_2 + |m| + 1 = n$. The quantum numbers n and m have the same physical meaning in both coordinate system. These eigenstates in these two system are related via unitary transformation,

$$|n, n_1, n_2, m\rangle = \sum_{l=|m|}^{n-1} (-1)^{(l-n+m+n_1-n_2)/2+l}\sqrt{2l+1} \begin{pmatrix} \frac{n-1}{2} & \frac{n-1}{2} & l \\ \frac{n_1-n_2+m}{2} & \frac{n_2-n_1+m}{2} & -m \end{pmatrix} |n, l, m\rangle \tag{159}$$

The term in the bracket is the Wigner 3-j symbol [19].

II.6.3 Avoided crossings and m-mixing

The separation between the Stark levels increases with the field as seen in the Fig. 24. At a certain field, the red state of the next higher manifold, n and the blue state of the lower manifold, $n - 1$ possess the same energy. This point is called the Inglis-Teller limit and is given by

$$F \cong \frac{1}{3n^5} \tag{160}$$

In the case of the hydrogen atom, the Stark states from the different n manifolds can cross. However, in the non-hydrogenic multi-electron atom the potential experienced by the excited electron is different than the pure Coulomb potential $1/r$ at short range. This effect makes the non-hydrogenic atoms to behave quantitatively different in two aspects. The total Hamiltonian can be defined as

$$\hat{H} = -\frac{\nabla^2}{2} + \frac{1}{r} + V_d(r) + Fz \tag{161}$$

(i) Owing to the core polarization and penetration of low l states, the effect of an electric field is substantially different. These new interactions break the dynamical symmetry. The Hamiltonian in the parabolic basis or the spherical basis does not remain diagonal any longer. The off-diagonal elements gives the coupling between the states of different n and l leading to the avoided crossings. The energy gap at the avoided crossing between the states $|n, n_1, n_2, m\rangle$ and $|n', n_1', n_2', m\rangle$ is given as

$$\omega_0 = 2|\langle n, n_1, n_2, m|V_d|n', n_1', n_2', m\rangle| \tag{162}$$

and the diagonal elements give the shift in the energy levels from their hydrogen
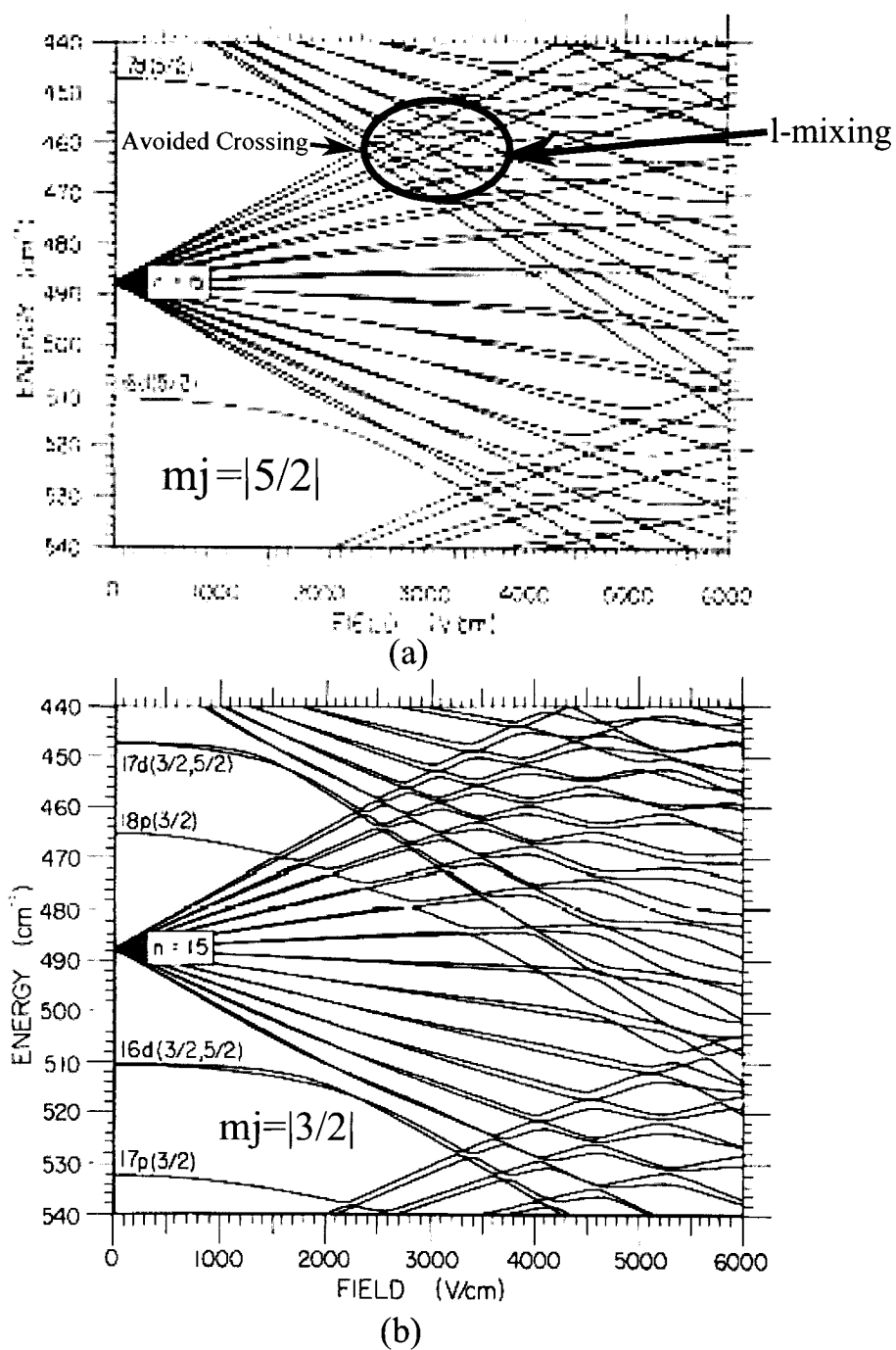
FIG. 25: Stark structure of rubidium. The quantum defect for p and d states is large, so these levels are well separated from the hydrogenic manifold. (a) The Stark map for the state $m_j = |5/2|$ and (b) $m_j = |3/2|$ (Fig. excerpt from [53]).

atom analogues.

$$\langle n, n_1, n_2, m | H | n, , n_1, n_2, m \rangle = \frac{1}{2n^2} + \frac{3}{2}n(n_1 - n_2)F$$
$$+ O(F^2) + \langle n, n_1, n_2, m | V_d | n, , n_1, n_2, m \rangle \tag{163}$$

with the non-diagonal part transformed

$$\langle n, n_1, n_2, m | V_d | n', n_1', n_2', m \rangle = \sum l \langle n, n_1, n_2, m | n, l, m \rangle \left(\frac{-\delta_l}{\sqrt{n'^3 n^3}} \right) \times$$
$$\langle n', l, m | n', n_1', n_2, m \rangle \tag{164}$$

where we use the relation

$$\langle n, l, m | V_d | n', l, m \rangle = \frac{-\delta_l}{\sqrt{n'^3 n^3}} \tag{165}$$

from the generalization of the matrix element

$$\langle n, l, m | V_d | n, l, m \rangle = \frac{-\delta_l}{n^3} \tag{166}$$

where $V_d = V_{pol} + V_{pen}$ is the difference in the potential from the pure $1/r$ potential in the field free case.

The $\langle n, n_1, n_2, m | n, l, m \rangle$ is the projection of initial Stark state on $|n, l, m\rangle$ and $\langle n, l, m | n, n_1, n_2, m \rangle$ represents the projection of the $|n, l, m\rangle$ state onto the $|n, n_1, n_2, m\rangle$. This implies the avoided crossing is due to the contribution from the orbitals with non-vanishing quantum defect. For low m, $|m| \ll n$, the energy gap at the avoided crossing between Stark states from neighboring n manifolds are large and approximately scales as $1/n^4$. Such behavior can be explained semi-classically as the electron orbit lying on the plane parallel to the electric field. The electron distribution is therefore pushed towards the core resulting in the large non-Coulombic field which in turn results in large quantum defect of the states. The large m states have an orbit perpendicular to the field. The electron distribution is not so much perturbed. Thus, the states of high m experiences a nearly Coulombic potential throughout, but the states of low m have a lot of core interaction and therefore exhibit larger energy gaps at avoided crossings than do states of high m [54].

(ii) The low-l states are well separated from the non-penetrating hydrogenic manifold of high l. These states are non degenerate and hence do not undergo a linear Stark

shift. But they have a quadratic Stark effect. The hydrogenic manifold fans out depending upon the strength of the electric field. The low l state and the red state of the high-l manifold approaches with increasing field and can couple [55] as shown in Fig. 25. Such stabilized high-n states hugging each other represents the l and m mixed states and can be thought as the magic island of stability called the ZEKE states.

II.6.4 Lifetime dependence on angular momentum quantum number

We can describe the lifetime for a Rydberg state of principal quantum number n by

$$\text{lifetime}(n) = \text{orbital period}(n)/p(n) \tag{167}$$

where $p(n)$ is interpreted as the probability of decay per orbit [56]. This relation provides the basis for understanding of the enhancement of the lifetime of the ZEKE states produced because of the presence of stray or intentionally applied electric fields. When the electron has fixed low l, the electron can get near the ionic core and autoionize with a probability $\simeq 1$ if we assume the probability to decay whenever the electron gets near the core is 1.

Because of the distribution of l for ZEKE states, it is only occasionally that the electron approaches the core. Thus, the inclusion of more than simply low-l states of the Rydberg electron reduces the probability to get near the core which in turn reduces the probability of ionizing by $1/n$ if l is changing from the 0 to $n - 1$. In addition, m-mixing is also possible if the cylindrical symmetry of the system is broken. The high m states do not contain the low l components, hence further preventing the electron from approaching the core even if the angular momentum l is precessing in a field. The probability is further reduced by $1/n$. Therefore, the total probability for the electron to approach the core is reduced by $1/n^2$ if we consider the complete l and m-mixing of the states, increasing the lifetime of these states by a factor of n^2.

CHAPTER III

EXPERIMENTAL TECHNIQUE

III.1 INTRODUCTION

This chapter discusses the design and the operation of the various components of the experiments performed, including details of the magneto-optical trap used for the production of ultracold argon atoms in the metastable state. Since argon is a noble gas, it does not have a trapping transition from the ground state which is easily accessible using a commercially available laser source. However, there is a trapping transition accessible using commercial laser sources once the atoms are excited to the metastable state. The starting point for such an experiment, therefore, is the metastable atom source. Sec. III.2.1 discusses the preparation of the atoms in the metastable state. The exiting velocity of the atoms is $\sim 400\text{ms}^{-1}$ which is much higher than the capture range of the velocity of the MOT which is around ~ 40 ms^{-1}. Thus the atoms must be slowed down before entering the MOT region. This is achieved by employing a Zeeman Slower in our experiments which exploits the Zeeman shift of the energy levels in the presence of the magnetic fields to counteract the Doppler shift due to the velocity of the atoms to maintain the resonance condition for the atom as it is slowed down by the counterpropagating slowing laser beam. The mechanism and working principle of a Zeeman slower is explained in Sec. III.2.2. The metastable argon atom is designated as $^{40}\text{Ar}^*$.

After deceleration to the velocity suitable for cooling and trapping, the atoms enter the science chamber where they are cooled and trapped in the intersection of six counter-propagating laser beams along with additional magnetic fields from three shim coils to cancel the earth's B-field and a quadrupole B-field from a pair of anti-Helthomltz coils. The formation of the MOT can be visualized using the CCD camera connected to a monitor or a Photomultiplier Tube (PMT) connected to the oscilloscope. The ion detection system - channeltron and QMS/RGA are placed at the opposite ports in our experiment along with the home built ion optics discussed in detail in III.9. For an efficient trap a very high vacuum is maintained using turbo pumps and an ion pump.

The diode lasers we use are in a master-slave configuration (sometimes called injection-locked) utilized to derive the laser beams for the slowing and trapping of

the atoms. The laser beams are transported to the science chamber via optical fibers. This is explained in Sec. III.5. For ionization of the atoms or to produce high-lying Rydberg states, we use dye lasers pumped with the second and third harmonics of a Nd-YAG laser to produce the two laser frequencies we need for the two step excitation to the Rydberg or autoionizing states.

The study of time evolution dynamics of an ensemble of ultracold Rydberg atoms produced via two-color, two-photon excitation is one of the main components of the research reported in this dissertation. The production of such Rydberg atoms is elaborated in Sec. III.8. Since Rydberg atoms are very sensitive to the external electric fields, small stray or intentionally applied fields can completely change the internal dynamics of the Rydberg atom system by mixing of various l and m states of the same or neighboring manifolds. The ions born at the interaction region are collected using a detection system mentioned in Sec. III.9. The signal is read and analyzed via the data acquisition system. The data acquisition unit has various components working in tandem which is discussed in detail in Fig. 54.

III.2 SOURCE CHAMBER

The source chamber is divided into two sub regions

- ^{40}Ar* Source

- Zeeman Slower

III.2.1 ^{40}Ar* Source

The metastable argon source module uses an inductively coupled RF-discharge. The voltage controlled oscillator (VCO) provides the source for the radio frequency (RF). The RF discharge is formed in the atomic beam path, inside a quartz tube surrounded on the outside by an RF induction coil made up of copper. A high frequency alternating current flows through the solenoid resulting in the oscillating magnetic fields parallel to the axis of the coil which in turn induces an azimuthal electric field or vortex electric field. The electric lines of force are closed circles concentric with the turns of the solenoid. A schematic of the source is shown in Fig. 26. Electrons in the atomic beam are excited by the vortex electric field. They quickly acquire enough kinetic energy to form a plasma ionizing the gas particles. Atoms are excited from
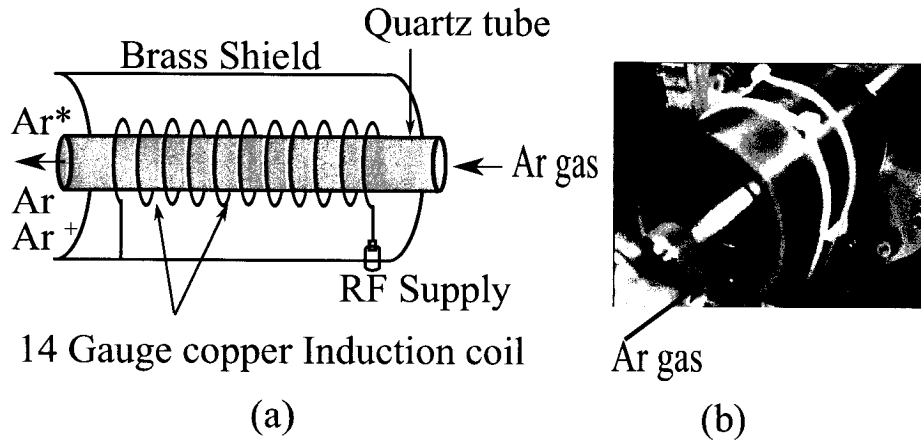
FIG. 26: (a) An inductively coupled RF driven discharge which prepares 1:1000 atoms in the metastable state, (b) picture taken with the argon discharge on.

the ground state to $4s[3/2]_2$ state along with the Ar and Ar^+ via electron impact excitation within the discharge. The metastable state of argon $4s[3/2]_2$ has a lifetime of 60 seconds.

Our coaxial resonator is made up of 1 cm quartz tube placed inside the 14 gauge copper solenoid. The number of turns and the diameter of the solenoid are respectively 11 turns and 3.2 cm diameter. The design detail is described in Hauke Busch's Ph.D. thesis [57].

The frequency of resonator is 155 MHz with an RF power of approximately 10-12 Watts. The circuit is assembled with the attenuators, amplifiers and impedance tuner to maximize the transmission as in Fig. 27. The RF-driven discharge produces a beam of metastable argon 1 : 1000 ground state atoms in the $4s[3/2]_2$ level and with a velocity of ~ 400 ms^{-1}. Thus, the atomic beam coming out of the discharge is the unequal mixture of Ar, Ar^+, and Ar*.

III.2.2 Zeeman slower

The velocity of the metastable source is approximately ~ 400 ms^{-1}. Therefore, the atoms produced with the velocity within the capture velocity below ~ 40 ms^{-1} is negligible. However the radiation pressure from a laser beam counter-propagating to the atomic beam can be used to slow down the atoms before they enter the MOT region. A Zeeman slower uses the Zeeman shift counteracting the Doppler shift in
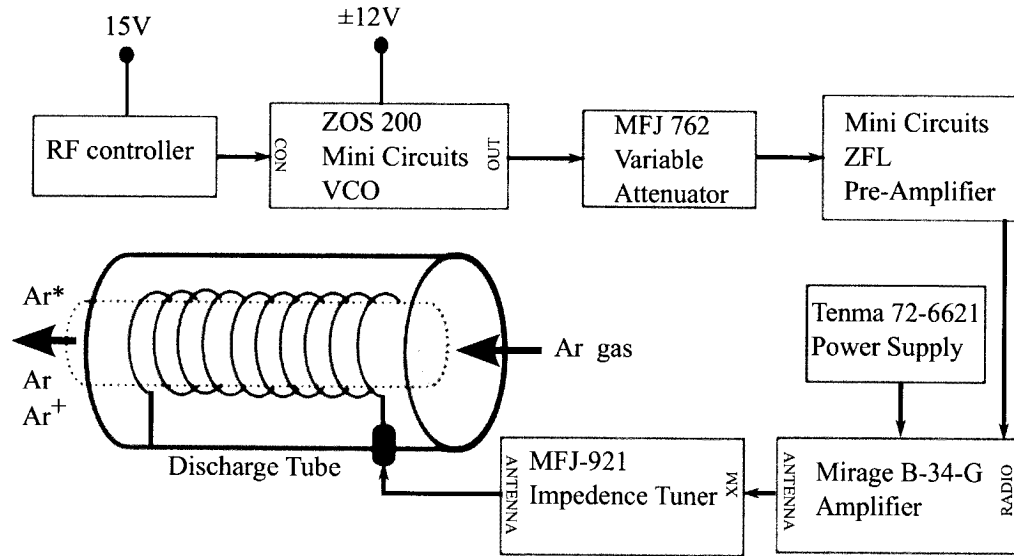
FIG. 27: A flow diagram for the impedance matched RF resonator.

order to slow down the atoms in the atomic beam. It consists of a tube inside which a magnetic field gradient is applied to shift the energy levels of the moving atoms in the presence of the counter-propagating laser beam. The laser is fixed and detuned below atomic resonances such that it is closer to the resonance for the fast atoms exiting from the discharge tube with the Doppler shift of $\omega_D = -\vec{k} \cdot \vec{v}$ due to the longitudinal velocity. As atoms slow down as a result of many optical transitions, the Doppler shift changes and they fall out of the resonance with the laser beam. The atoms can be brought back closer to the resonance either using (i) chirp pulse method which chirps the slowing laser frequency as the atoms slow down or (ii) Zeeman Slower method in which the magnetic field gradient compensates for the change in Doppler shift to maintain the resonance condition. This section explains the mechanism of the Zeeman Slower.

The atomic beam is passed through the ion deflection plate and the skimmer to remove ions and to allow for differential pumping of the vacuum system. The collimated atomic beam then enters the Zeeman slower with the velocity of approximately 400 ms^{-1} against the coaxial right circularly polarized beam. The counter-propagating σ^+ beam is detuned 150 MHz below the resonance such that it does not interfere with the atoms in the trap region. It pumps the atom to the $4s[3/2]_2 \leftrightarrow 4p[5/2]_3$ state. In the presence of the Doppler shift and the magnetic field the resonance condition

for an atom moving with longitudinal velocity $v(z)$ is

$$kv_z(z) + \delta_l - \frac{\mu_B}{\hbar}B_z(z) = 0 \tag{168}$$

where $kv(z)$ is the Doppler Shift, δ_l the detuning of the laser and the last term gives the Zeeman shift due to the magnetic field $B_z(z)$, and μ_B the Bohr magneton.

The distance atoms travel for the change in longitudinal velocity from v_i to v_f in the presence of a uniform acceleration of $a = \eta a_{max} = \eta\hbar k\Gamma/(2m)$ with a_{max}, the maximum deceleration and $\eta \leq 1$ is given by,

$$\Delta z = z_f - z_i = \frac{v_{iz}^2 - v_{fz}^2}{2a} \tag{169}$$

The longitudinal velocity as function of the position can be written as

$$v_z(z) = v_{iz}\sqrt{1 - \frac{z - z_i}{z_f - z_i}\left(1 - \frac{v_{fz}^2}{v_{iz}^2}\right)} \tag{170}$$

Eqs.170 and 168 gives the relation for the magnetic field as

$$B(z) = \frac{\hbar}{\mu_B}\delta_l + \frac{\hbar k}{\mu_B}v_{iz}\sqrt{1 - \frac{z - z_i}{z_f - z_i}\left(1 - \frac{v_{fz}^2}{v_{iz}^2}\right)} \tag{171}$$

The design of our Zeeman slower consists of two coaxial solenoids to produce magnetic fields in an opposite direction. Each solenoid consists of a single layer of 14 gauge insulated copper wire wound around the stainless steel tube with varying pitch as shown in Fig. 28.

The pitch is high at the beginning and becomes relaxed toward the end. These solenoids are wrapped with individual cooling jackets. The cold water from the process chiller flows through them in order to keep the solenoids from over-heating. The important advantages of the two solenoids are (i) the total change in the magnetic field is distributed over positive and negative values which significantly reduces the maximum field. This in turn reduces the power dissipation in the solenoid, (ii) the sharp change in the field gradient at the end of the solenoid causes the rapid decoupling of the atoms from the resonant slowing laser field which helps in the fine tuning of the velocity of the slowing atoms. The direction of travel of the atomic beam is assumed to be the z-axis. The field $B_z(z)$ decreases monotonically in the first solenoid. The magnetic field is zero in the region between the solenoids. The atoms attain the final velocity v_{fz1} in the first solenoid with the longitudinal dimension of
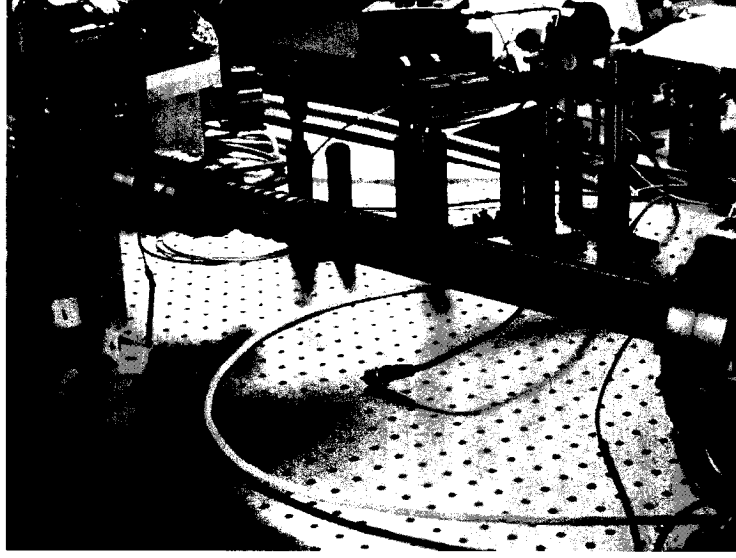
FIG. 28: The windings of the Zeeman slower for the generation of the magnetic profile to cool down the fast atoms entering from the discharge at right end (not shown in picture) [57].

$z_{1f} - z_{1i}$. The initial velocity of the atoms entering the Zeeman slower is v_{iz1}. The atoms travel the distance between the solenoid with the constant velocity of v_{fz1} and enters the second solenoid $v_{iz2} = v_{fz1}$ and further slow down to the velocity v_{f2z} in the longitudinal dimension of the second solenoid of $z_{2f} - z_{2i}$. In the second solenoid the magnetic field acts in the $-z$ direction or in other words it continuously decreases below zero.

Using the resonance condition in the region between the two solenoids where the magnetic field is assumed to be zero $\delta_l = -kv_{fz1}$, the magnetic fields inside two solenoids can be written as

$$B_z(z) = B_0 \left(1 - \frac{v_{i1z}}{v_{f1z}} \sqrt{1 - \frac{z - z_{i1z}}{z_{f1z} - z_{i1z}} \left(1 - \frac{v_{f1z}^2}{v_{i1z}^2} \right)} \right) \qquad z_{i1z} \leq z \leq z_{f1z} \qquad (172)$$

$$B_z(z) = B_0 \left(1 - \sqrt{1 - \frac{z - z_{i2z}}{z_{f2z} - z_{i2z}} \left(1 - \frac{v_{f2z}^2}{v_{f1z}^2} \right)} \right) \qquad z_{i2z} \leq z \leq z_{f2z} \qquad (173)$$
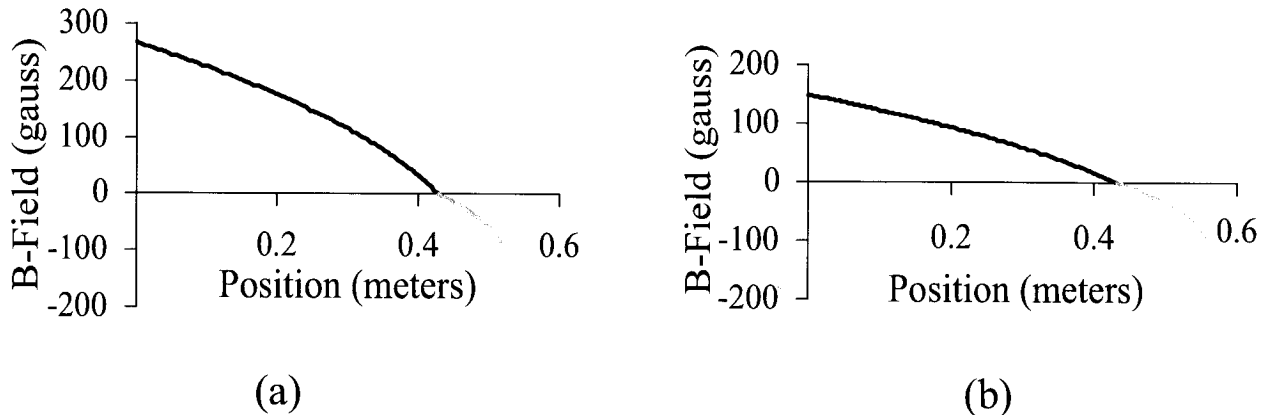
FIG. 29: Simulation of the magnetic field in our Zeeman Slower design for (a) argon and (b) krypton.

where $B_0 = \hbar\delta_l/\mu_B$ [58].

The magnetic field profile must be designed to maintain the resonance condition. This imposes the criterion on the steepness of the field along the slower. We have

$$a = \frac{dv_z(z)}{dt} = v_z(z)\frac{dv_z(z)}{dz} \tag{174}$$

which leads to the following relation obtained from Eq. (168) in order to maintain the resonance condition

$$\left|\frac{dB_z(z)}{dz}\right| \leq \frac{\hbar k a}{\mu_B v_z(z)} = \frac{\hbar k}{\mu_B v_z(z)}\frac{\eta\hbar k\Gamma}{2m} \tag{175}$$

The magnetic field profile for Ar* and Kr* in our Zeeman Slower design are respectively shown in Figs. 29(a) and 29(b).

III.3 VACUUM SYSTEM

The research grade argon is fed to the system through a dual stage brass regulator and Granville Phillips 5097 leak valve controlled by the 216 Servo Driver. The argon gas flows through a flexible stainless steel tube torr-sealed to a 1 cm quartz tube which is provided with the assembly for RF-resonators explained in III.2.1.

The vacuum system consists of three sub-regions: denoted as the source region, intermediate region, and MOT region. An integrated differential pumping scheme is employed to have different pressure in the source region and the MOT region as shown in Fig. 30. The apparatus consists of a series of stainless steel vacuum chambers sealed with conflat flanges or viewports using copper gaskets. The metastable argon is produced in a RF discharge tube at the pressure of $\sim 10^{-3}$ Torr. The atoms and atomic ions then enter the first pumping region provided with the skimmer made up of a 1 cm stainless steel tube (with a tapered end towards the RF discharge) and a Pfeiffer TMU262P model turbo pump that has the pumping capacity of 210 ls^{-1}. There is also a deflection field plates assembly here. The atomic beam contains the unwanted ions from the discharge. These ions are deflected by allowing the atomic beam through a pair of parallel field plates 2.5 cm apart with one plate at 100 V and the other grounded. The atomic beam is then passed through the skimmer where the rough collimation of the atomic beam takes place and the rejected atoms are pumped out by the turbo pump. The pressure in this region in monitored with an ionization gauge. The optimal source pressure is found in the range of 1×10^{-5} Torr to 5×10^{-5} Torr.

The atoms then enter the second pumping region called the intermediate region. This region is assembled with another skimmer and a turbo pump of model Pfeiffer TPH050 50 ls^{-1} and UHV-nude ionization gauge implanted in the system. The optimal operational pressure in this region is found to be $\sim 10^{-5}$ with the atomic discharge on. The atomic beam then enters the first solenoid of the Zeeman slower followed by the Pfeiffer TPH050 50 ls^{-1} pump. The last skimmer nipple is assembled along with a MDC gate valve that separates the intermediate chamber from the science chamber where the MOT forms. The MOT region is provided with a turbo pump Pfeiffer TPU071-60 ls^{-1} and an Ultek D I-11 ls^{-1} ion pump and Ti-sublimation pump. The pressure in the MOT region is monitored by the ion pump current. The pressure is maintained at roughly 10^{-9} Torr with the atomic beam running at low pressure mode where the intermediate chamber pressure is at 10^{-5} Torr.

All the turbo molecular pumps and ion pump are backed by a roughing pump which can evacuate to the pressure of 10^{-3} Torr. The backing pressure in the science and source chambers are monitored by Duniway DST-531 thermocouples located at the back of Pfeiffer TPU071-60 ls^{-1} and turbo Pfeiffer TMU262P-210 ls^{-1} respectively. In order to evacuate from the atmospheric pressure, a standard procedure
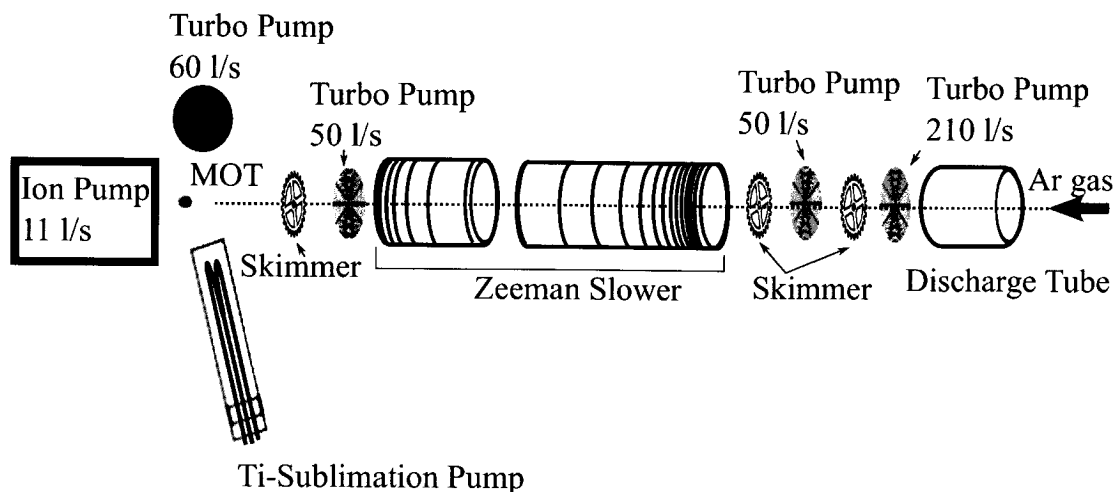
FIG. 30: Schematic of the vacuum chamber.

follows the backing out of the vacuum chamber with the rough pump until the pressure gets below 10^{-1} Torr followed by activation of the turbo pump. Typically the evacuation takes several days to a week to reach the operating vacuum of $\sim 10^{-9}$ Torr. The Ti-sublimation pump is used occasionally with a current of 50 A for 1 min to accelerate the pumping process. Alternately, baking of the system is also possible to boil off the contaminants of the chamber walls that impair the vacuum. The baking is done by gradually heating the wire wrapped around the chamber in steps until a temperature of 150^0 C is achieved.

III.4 SCIENCE CHAMBER

The science chamber (MOT chamber) is made up of a stainless steel cylinder with diameter of $8''$ and height of $2 - 2/3''$ provided with 14 conflat vacuum flange ports with outer diameter of $2 - 3/4''$. Twelve of these ports are on the cylindrical surface of the chamber. These ports are aligned horizontally and are at 30^0 from each other whereas two ports on the top and bottom surface. One of these flanges is connected to the end of Zeeman slower Conflat flange sealed with a copper gasket while the opposite port is assembled with a tee and the viewport which serves as an entrance for the Zeeman slower beam. The other flange of the tee is connected to the ion pump. The remaining eight ports are assembled with the optical windows directly to the flanges on the chamber while one port has a tee with the optical window and

Ti-sublimation pump. The glass of the optical windows are $1 - 1/2''$ in diameter and are antireflection (AR coated) while one of the remaining three ports is used for connecting a Pfeiffer TPU071-60 ls^{-1} turbo pump and the other two opposite ports are respectively used for a channeltron and a QMS/RGA along with the ion optics on them. These viewports are used for six counter-propagating cooling and trapping beams intersecting at the center of the chamber. Each pair of the counter-propagating beam has opposite helicity. And, the remaining viewport is used for the fluorescence detection and the pulsed dye laser beams.

III.5   LASER SETUPS AND OPTICAL METHODS

The schematic of the experimental set ups of the optical system is shown in Fig. 31. It consists of three separate lasers in master-slave configuration with one being master and two are the slaves. The master laser is a tunable external cavity diode laser (ECDL) as shown in Fig. 32(a). It is comprised of a Sanyo DL-LS-2031 150 mW laser diode mounted inside a Thorlabs CT110TM-B collimation tube which is held firmly in a homebuilt aluminum mount carefully engineered so as to have the capabilities of maintaining the temperature by the use of a Marlow DT12-6-01 Thermoelectric cooler (TEC) placed in between the mount and the large aluminum base using thermal grease to insure good thermal contact. The thermistor sensor is positioned inside a hole drilled in the aluminum bezel near the laser diode recess to monitor the temperature and send the feedback to the TEC. The large aluminum base acts as a heat sink. The whole assembly is mounted on aluminum base-plate as shown in Fig. 32.

A current of ~ 134 mA is supplied to the laser by a home built power supply and the temperature is stabilized to 9.65V (as read on the controller monitor) which corresponds to 20^0 Celsius using a home built temperature controller. The collimation tube can be fine adjusted for the collimation of the laser beam exiting the diode. The Littman-Metcalf configuration has been employed. The 1200 lines/mm (Edmund Optics NT43-848) diffraction grating is held on a fixed mount with post tied to the base-plate using clamping forks. And, the base-plate is tied down on the floating TMC optical table to dampen the possible vibrations. The tuning IR-mirror on a kinematic mirror mount is tightly secured on the base-plate so as to close the cavity by reflecting the first-order beam back to the laser while the zeroth order or the specular reflection is taken as an output. The wavelength can be tuned by rotating
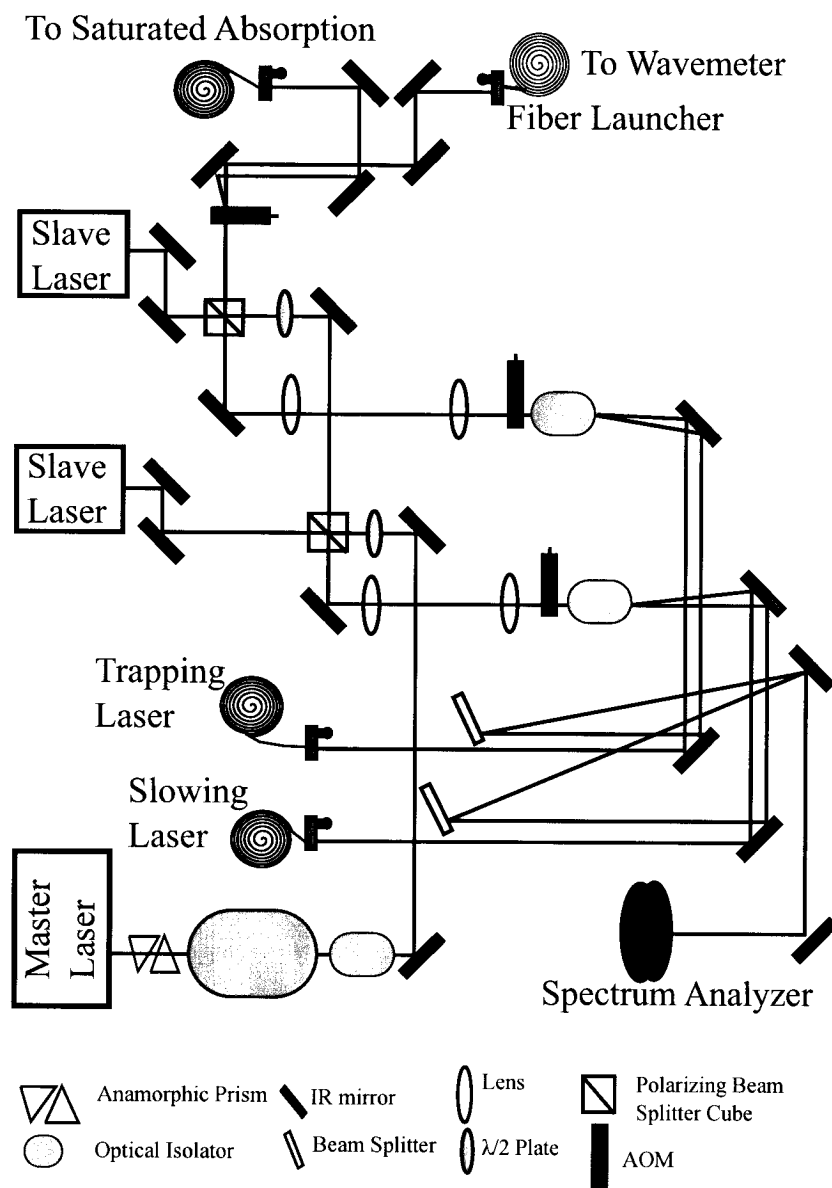
FIG. 31: Experimental set up of the diode lasers and the optical components for laser cooling and trapping of metastable argon.

the mirror. The PZT (peizo-electric transducer) is a Thorlabs AE0203D04 and is placed in the groove for the horizontal adjustment screw, carefully so as not to crush the wire connection to PZT. The cavity is tweaked to obtain the stabilized wavelength of $\sim$ 811.755 nm. The laser runs single mode with the spectral line width of < 1 MHz and is capable of being scanned $500 - 700$ MHz before mode hopping takes place. The complete ECDL setups are enclosed in an aluminum enclosure with the holes milled for the laser beam output and the access to the vertical and horizontal mirror adjustment screws. The output beam has vertical polarization and is elliptical, therefore, it is passed through a pair of anamorphic prisms in order to make the beam circular with gaussian profile. The nearly circular and gaussian beam is then passed through optical isolators IO-5-810-IP/VPL-Z and OFR-IO-30-780-VPL which act like an optical diode by blocking any beam towards the laser. This helps maintain the stability of the laser against unwanted feedback. The laser is then split into s-and p- polarized states by directing it though the $\lambda/2$ waveplate followed by a polarizing beam splitter cube (PBS). However, transmission and reflection intensity can be controlled by rotating (the orientation of the fast axis) the waveplate. The p-polarization beam is transmitted and s-polarization component gets reflected. The s-polarization beam is further passed through the $\lambda/2$ waveplate and a PBS to split the beam into two more s-and p-component beams. The s-component is then passed through an acoustic optic modulator (AOM) driven by RF at 80 MHz. The first diffracted order is aligned and sent to the saturated absorption system and the zeroth order is sent to the wavemeter for the wavelength monitoring. The p-polarization beam from the first PBS cube is injected into the slave laser via two aligning IR-mirrors.

A slave laser has a simpler design and less optical components as depicted in Fig. 32(b). A Sanyo DL-LS-2031 150 mW laser diode is carefully placed in the collimation tube CT110TM-B. The whole assembly is kept in the aluminum bezel provided with the capabilities of maintaining the temperature like in the master laser. The beam from the the master laser is injected into the slave laser itself. This makes the slave laser mode follow that of the master and the procedure is termed injection locking. The output of the slave laser also has vertical polarization, the beam gets reflected by a large amount while a small amount is transmitted on the beamsplitter cube. The reflected slave beam is then passed through a telescope to reduce the beam waist so as to make it a more compatible waist to pass through the acoustic optic modulators

Diffration Grating   Mirror   Laser Diode

(a)   (b)
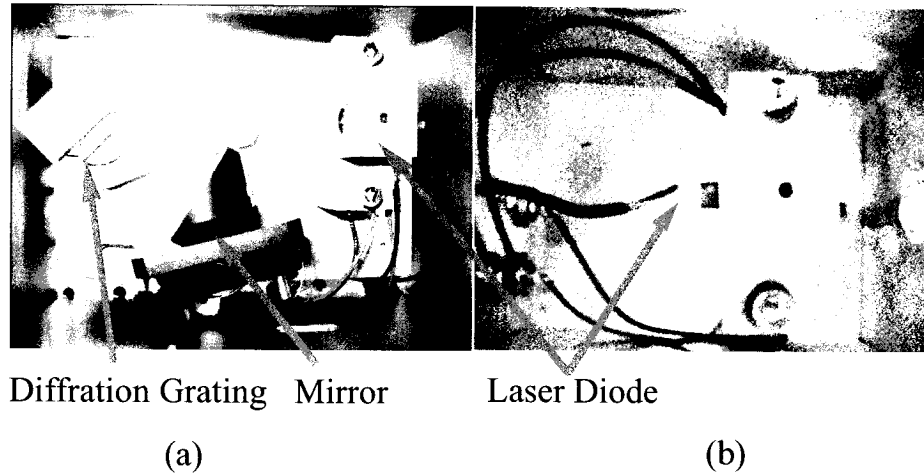
FIG. 32: (a) External cavity diode laser in Littman-Metcalf configuration for master laser and (b) bare diode laser with collimation in the laser housing for slave laser.

(AOM) driven by radio frequency (RF) at 80 MHz. The negative first order (now 160 MHz red detuned from the atomic resonance) is aligned to the fiber launcher provided with a Thorlabs C110 lens and transmitted to the fiber de-launcher for the Zeeman slowing beam via non-polarization maintaining optical fiber (Thorlabs FS-SN-3224 FC/APC). The zeroth order is aligned to the spectrum analyzer. The p-polarization beam from the second PBS is used to pull or injection lock the slave laser (for the MOT). The out-coming beam undergoes the similar alignment except for it passes through the AOM driven by RF at $\sim$ 69 MHz. Now, the first order is $2\Gamma \sim 11$ MHz red detuned from the atomic resonance and is aligned to the fiber launcher for trapping of Ar*, following the same system like in the slowing beam and the second order is coupled with the zeroth order from the other AOM to send in to the spectrum analyzer.

III.5.1   Doppler free saturated absorption spectrometer

The arrangement for saturated absorption spectroscopy is depicted in Fig. 33. The laser beam is reflected off of the thick glass beam splitter into two beams. The two beams are then aligned to travel through the discharge. These beams are called the probe beams. The transmmited beam is routed around to overlap with the stronger one of the probe beams. The overlapping laser beam propagating in the opposite

TABLE III: Properties of optical transitions for laser cooling and trapping of ^{40}Ar*

Optical transition $3p^5(^2P^0_{3/2})4s^2[3/2]^0_2 \leftrightarrow 3p^5(^2P^0_{3/2})4p^2[5/2]_3$	λ_{vacuum}	811.754 nm
Satutation Intensity	I_{sat}	1.29mw/cm^2
Doppler limit	T_D	127μ K
Recoil limit	T_R	361 nK
Optical transition $3p^5(^2P_3/2^0)4s^2[3/2]^0_2 \leftrightarrow 3p^5(^2P_1/2^0)4p^2[1/2]_1$	λ_{vacuum}	696.735 nm
Satutation Intensity	I_{sat}	0.393mw/cm^2
Optical transition $3p^5(^2P_3/2^0)4s^2[3/2]^0_2 \leftrightarrow 3p^5(^2P_1/2^0)4p^2[3/2]_2$	λ_{vacuum}	706.917 nm
Saturation Intensity	I_{sat}	0.224mw/cm^2
Optical transition $3p^5(^2P_3/2^0)4s^2[3/2]^0_2 \leftrightarrow 3p^5(^2P_1/2^0)4p^2[3/2]_1$	λ_{vacuum}	714.0111 nm
Saturation Intensity	I_{sat}	0.357mw/cm^2

direction to the probe beams is called the pump beam. The probe beams are reflected at 45^0 from 50/50 beam splitter and directed to two photodiodes respectively.

III.5.2 Laser stabilization

The number of atoms in the trap is nearly proportional to the amount of trapping laser power. The trapping of an atom requires a laser must be absolutely stabilized down to an accuracy of few MHz. This requires an elimination of any fluctuations in laser frequency. The frequency of the laser depends on three factors (i) the driving current and (ii) the temperature of the laser and environment, and (iii) feedback. With current and the temperature fixed, the wavelength changes with the effective cavity length. This can be accomplished by using the PZT on the back of the mirror mount. The laser is tuned to 811.755 nm with the driving current of ~ -130.6 mA and set point of temperature at 9.498 V. The reference signal with the frequency ~ 10 kHz is added to the laser driving current through a bias-T. The PZT is ramped at a frequency ~ 10 Hz over a few volts and the horizontal alignment of the tuning mirror of the ECDL (PZT offset control) is scanned until the absorption peak as shown in Fig. 34 is obtained [59].

The absorption signal is fed to the lock-in amplifier through the signal input. The
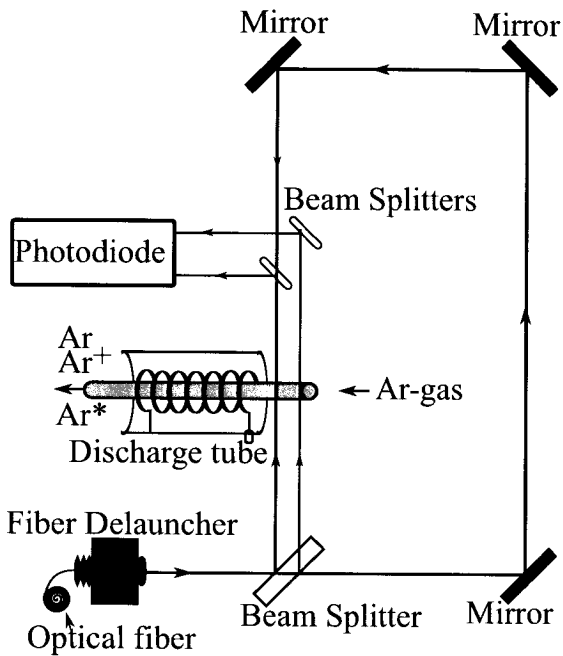
FIG. 33: Doppler free saturated absorption spectroscopy.

(a)

(b)
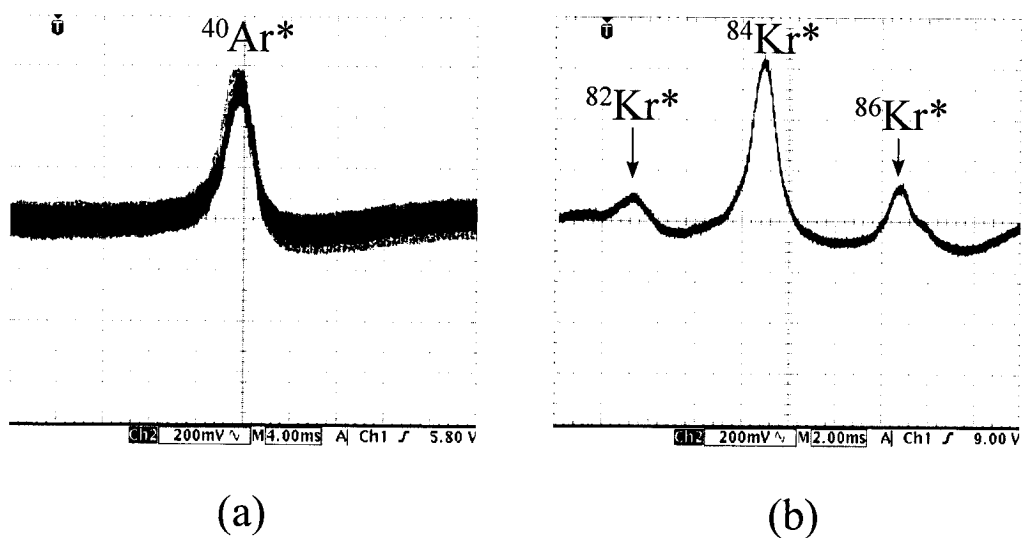
FIG. 34: (a) Doppler free saturated absorption signals for ^{40}Ar* and (b) the saturated absorption signals for Krypton for ^{80}Kr*, ^{84}Kr and ^{86}Kr respectively.
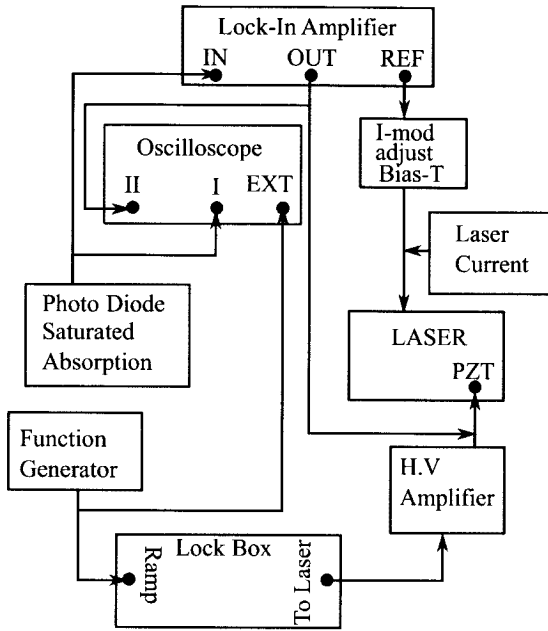
FIG. 35: Laser stabilization and locking scheme.

signal is then demodulated to give an error signal which appears to be a derivative of the saturated absorption signal. The sensitivity, the time constant and the phase is adjusted. By slowly decreasing the gain and tuning the horizontal position of the mirror, the laser frequency is locked to the zero crossing of the error signal corresponding to the resonant frequency. This technique is known as a phase sensitive detection. The error signal is then fed back to the PZT to keep the laser frequency on the peak. The detailed schematic of the locking is illustrated in Fig. 35.

III.5.3 Optical system geometry

The optical power for the slowing and the trapping laser in front of the respective launchers are $\sim$ 39 mW and $\sim$ 36 mW respectively. The maximum efficiency of transmission of the optical fiber is about $\sim$ 50% giving the output power in front of the respective de-launcher of $\sim$ 18 mW and $\sim$ 21 mW for trapping and slowing lasers, respectively. Both the slowing laser beam and the trapping laser beam are decoupled from their respective fiber de-launchers with a C110TMB lens. The beams are then passed through a $\lambda/4$ plate to correct for some possible birefringence in the beams and then passed through a $\lambda/2$ waveplate followed by the PBS cube for the

absolute confirmation of the orientation of the polarization of the beams. The slower beam is magnified by sending it through a telescope. The expanded slower beam is then reflected off of a set of IR-coated mirrors and then aligned along the Zeeman slower. The trap laser beam is de-launched the same way as the slower beam and passed through the $\lambda/4$, $\lambda/2$ waveplates and PBS cube in series. The beam is then passed through a cage assembly of the $\lambda/2$ waveplate and the telescope for the magnification of the beam. The beam is then split into three nearly equal intensity beams along three orthogonal directions using two PBS cubes. The intensity of the beams can be adjusted by rotating the $\lambda/2$ waveplate on the cage assembly. All three beams are aligned to launch into the chamber after the $\lambda/4$ waveplate in front of the viewports in three orthogonal directions with two of the three beams in the horizontal plane and one in a vertical plane. The incident beams are then retro-reflected in the presence of the $\lambda/2$ waveplate in between the retro-reflecting IR mirrors and viewports. Finally, the helicity of the incident beams are set by rotating the $\lambda/4$ waveplates as the orientations of the helicity depend on the orientation of the magnetic field gradients provided by an anti-Helmoltz coil. Our anti-Helmoltz coil is a pair of coils made by winding 14 gauge copper wire around a conflat flange with full nipples connected to the top and bottom. The two beams on a horizontal plane must have the same helicity, while the beam that propagates along the coil axis must have opposite helicity. The geometry of optical setups in the science chamber region is shown in Fig. 36.

III.5.4   MOT detection

Fluorescence imaging is used as a standard procedure to detect and to determine the number of atoms in the MOT. The atoms in the MOT scatter photons and these scattered photons are typically detected using either a charged coupled device (CCD) camera or photomultiplier tube (PMT). A standard video camera is used to get the spatial information but it does not give accurate information about the number of atoms whereas a PMT can provide the photon counts which can be related back to the number of atoms in the trap. An assembly for the PMT outside the viewport as shown in Fig. 37 [57, 60].
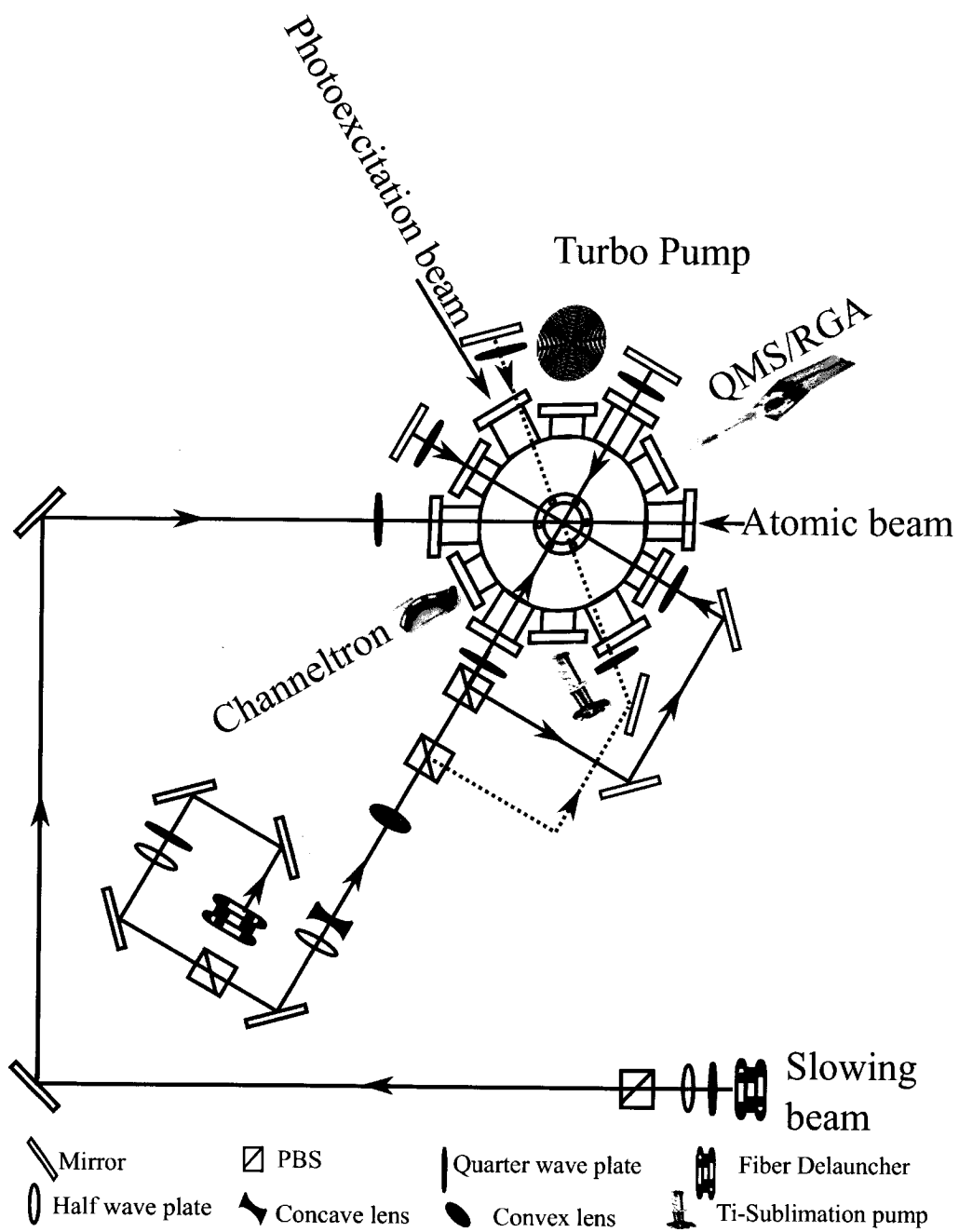
FIG. 36: The geometry of optical setups in the science chamber.
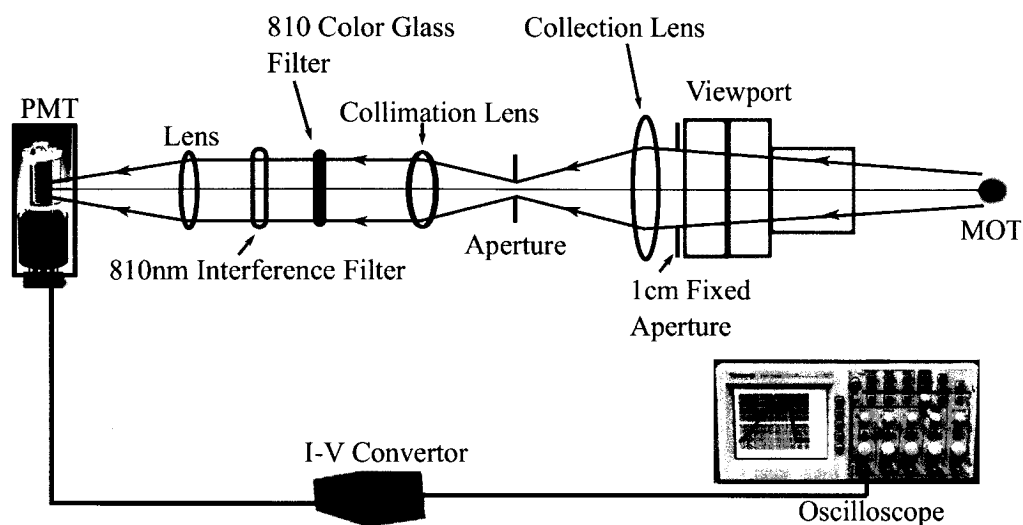
FIG. 37: An assembly of optical setups for the fluorescence detection.

III.6   PULSED Nd-YAG LASER

A compact Q-Switched Nd-YAG (Quantel Brillant) is used as the pumping source for the dye laser. The laser is custom assembled and includes optional attenuation of the fundamental beam of 1064 nm to enable low power output without modifying the Q-switch timing. Our Nd-YAG (yttrium aluminum garnet) laser system has second and third harmonics. The non-linear crystals and dichoric mirrors are assembled in compact modules. Phase matching for the second and third harmonics is obtained by mechanical adjustment of the crystals. The second harmonics module is provided with the side exit option as well. The laser is tightly secured on the optical table. In the experiment, both the fundamental plus second harmonics and third harmonics are taken out from the front two exits respectively. The maximum output powers are 83 mJ/pulse and 60 mJ/pulse for second and third harmonics respectively. The polarization of the third harmonics is changed to vertical polarization after reflection through a periscope and routed to pump a Coumarin-460 dye in a Continuum pulsed dye laser. The second harmonic is separated from the fundamental using a 532 nm dichroic mirror and aligned to pump a home-built LDS-720 dye laser.
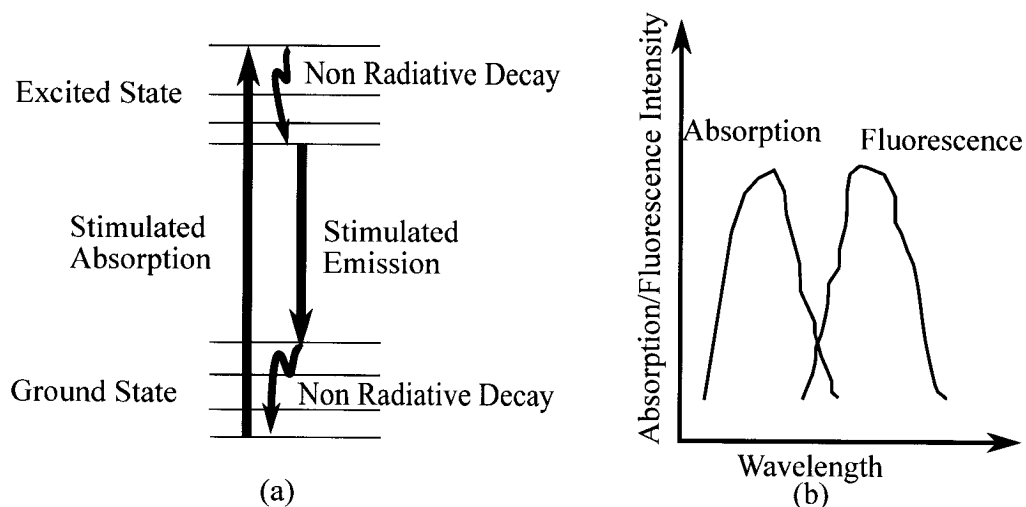
FIG. 38: (a) Schematic of energy levels of a generic laser dye. The non-radiative, instantaneous decay to the lower metastable excited levels causes the population inversion required for the lasing action, (b) the absorption and fluorescence wavelength [64].

III.7 PULSED DYE LASER SETUPS

Dye lasers are the unique source of tunable coherent radiation ranging from near ultraviolet to near infrared facilitated by the use of various dye molecular species. The dye laser uses a solution of organic dye molecules as the gain medium. A dye laser is a passive device hence it requires optical pumping sources like a ruby laser or Nd-YAG laser. This was first introduced in 1966 by three groups independently [61], [62] and [63]. The key principle behind the laser action is stimulated emission. The operation of a dye laser involves the excitation of organic dye molecules dissolved in the proper solvent at suitable concentration. The optical properties of the gain medium significantly depend on the solvent used to prepare the dye solution. The molecules are excited to higher energy levels within the excited energy band by the pumping laser as in Fig. 38 followed by the instantaneous non-radiative decay to the lower level within the energy band. The molecules spontaneously decay to the ground state. Thus the absorption energy is always greater than the fluorescence energy shown in Fig. 38(b).

III.7.1 Commercial dye laser

The dye laser is made up of three stages (i) oscillator, (ii) pre-amplifier and (iii) amplifier. The optical arrangements are as shown in Fig. 39. The oscillator stage forms the main cavity for lasing consisting of a gain medium, diffraction grating together with a prism beam expander, and mirror on one side and an output coupler on the other end. The dye flows through a rectangular cuvette with the openings at the top and the bottom connected to the dye circulator through a teflon tube. The opposite faces of the cuvette are wedged to avoid lasing action within the cuvette. The oscillator is transversely pumped with 8% of the total input power of Nd:YAG laser ($\sim$ 60 mJ per pulse at 355 nm, 10 Hz, 5 ns). The beam is sent through the cylindrical lens with proper orientation placed at suitable distance from the cuvette in order to avoid the tight focussing and overdriving the dye. The transverse pumping is comparatively easier than longitudinal pumping in terms of alignment however there is a trade off with the beam quality. The lasing action takes place very close to the front face of the cuvette since the pump beam travels only a short distance due to the high absorption in the dye. The significant amount of edge effects are inevitable in the beam. A procedure for the alignment of the oscillator, preamplifier and final amplifier was followed as in Continuum ND-5000 operating manual. The preamplifier is a single pass amplifier consisting of a parallelopiped cuvette with a dye flowing through it. It is also transversely pumped with the 20% of the remaining beam. The path difference between the pump beam and the dye beam from oscillator is such that the pump beam pumps the band of dye molecules to the excited state while the dye laser passes through and causes the stimulated emission and boosts the output power. The pre-amplified dye beam is then passed through the horizontally held cylindrical tube cuvette with a dye solution flowing through it. This is the last stage in the dye laser configuration. It is pumped with all the remaining power of third harmonics of the Nd-YAG laser. It is also pumped transversely with the beam expanded horizontally so as to excite greater number of molecules. Finally, the beam splitter and the orientations of the cylindrical lenses are tweaked carefully as mentioned in the manual of Continuum ND-5000 to maximize the dye beam power. When pumped with 620 mw of power at 355 nm and 5 ns pulsed length, the maximum power obtained with the fresh dye solution is 30 mw. The output is tunable and provides the second step photon for the experiment.
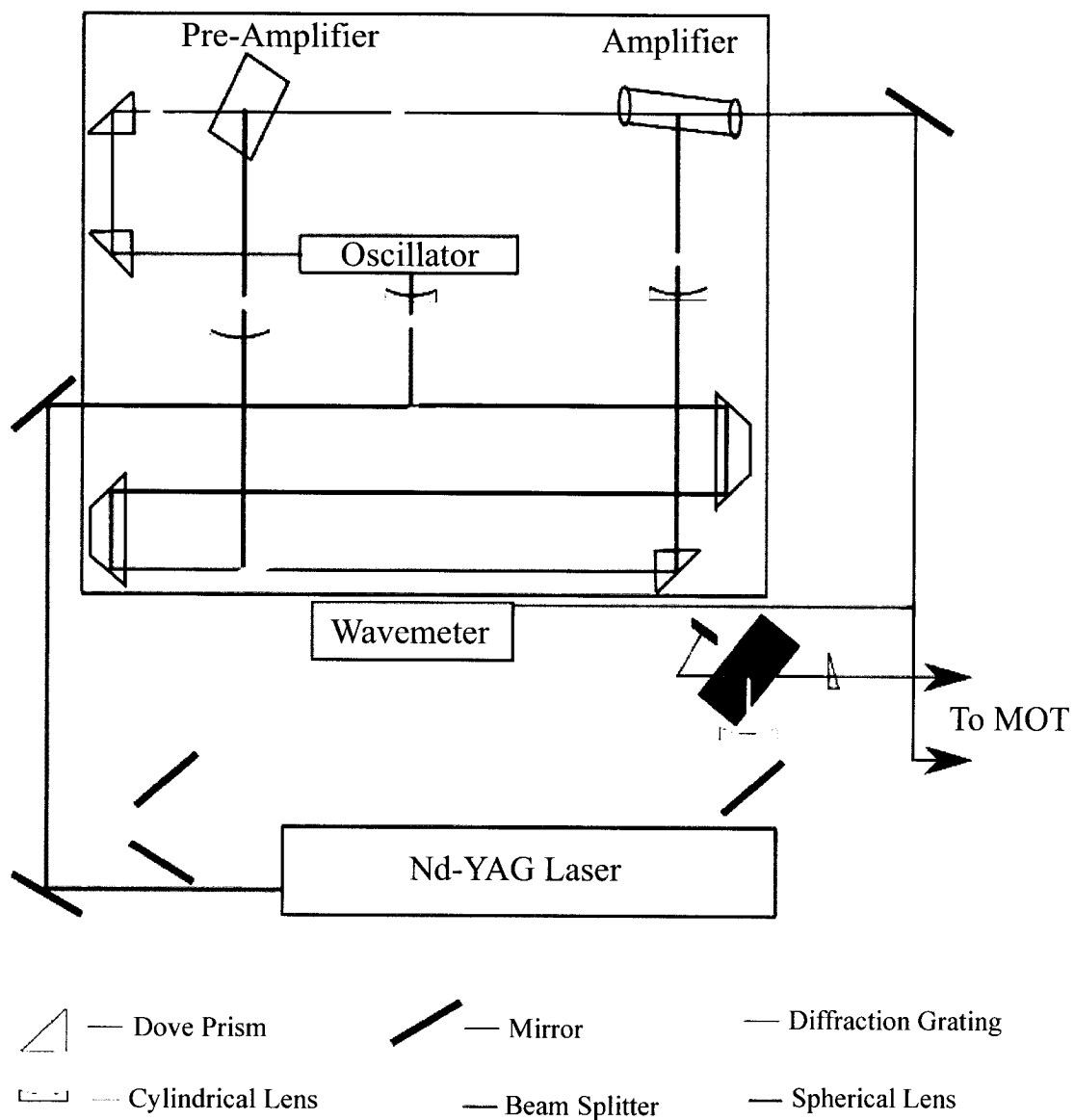
FIG. 39: Experimental setups for the dye laser for the generation of the first and second step dye beams.

tuning mirror   cuvette

wedge output
coupler

Diffration grating   cylindrical lens
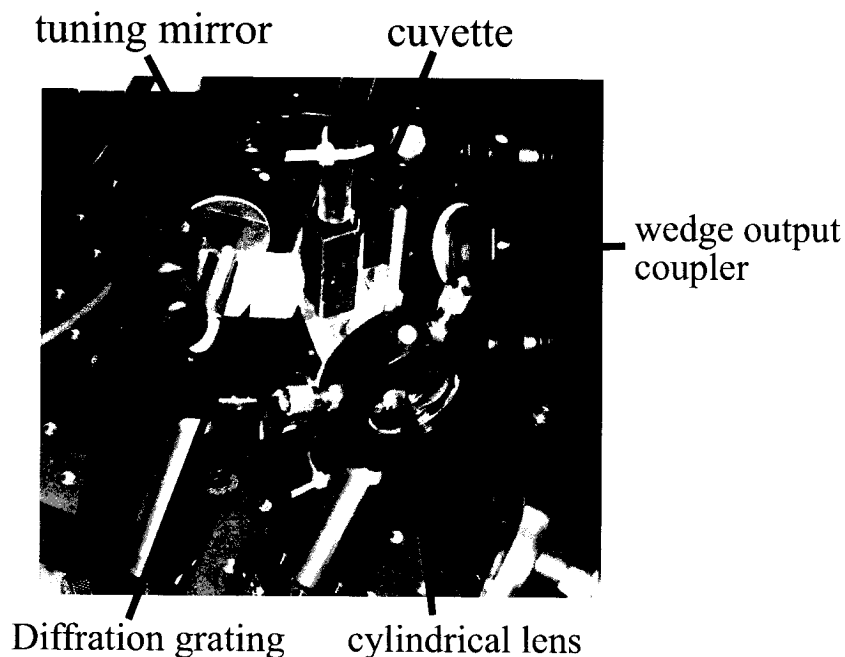
FIG. 40: The homebuilt dye laser system with a flowing LDS -720 dye solution.

III.7.2 Home-built flowing dye laser

The first step photon for the excitation is provided with the home-built dye laser. The home built dye laser consists of a flowing cell with the opening at the top and bottom. The LDS 720 dye mixed in methanol with the molar concentration of 2×10^{-4} flows through the cell through teflon tubing connected to the openings and powered by the Micropump MOD 000 − 415. The flowing dye in the cuvette is pumped by the second harmonic of the Nd-YAG (532 nm) with 8% of the total power of ~ 800 mw coming out of the Nd-YAG laser. The pump beam is focussed using a cylindrical lens such that the pump beam excites the horizontal band of dye molecules. The focussing of the pump beam has been carried out with great care so that it never reaches the damage threshold of the cuvette. The Littman configuration is employed with the diffraction grating of 1200 lines/mm mounted fixed so as to cover most of its grooves and the IR tuning mirror for selection of the wavelength on one side and the output coupler on the output dye side. No beam expanding optical components are used. The configuration is shown in Fig. 40.

TABLE IV: Dye laser table

Dye	Coumarin-460	LDS-720	Coumarin-480
molecular wt.(gm)	231.30	526	255.32
wavelength Range(nm)	442 − 480	680 − 775	459 − 508
max. wavelength (nm)	460	720	475
Solvent	Methanol	Methanol	Methanol
Concentration(molar)	1.6×10^{-3} (Osc.) 5.6×10^{-4} (Amp.)	2×10^{-4}	4.3×10^{-3} (Osc.) 1.8×10^{-3}(Amp.)

III.8 RYDBERG AND AUTO-IONIZING ATOMS PRODUCTION

Argon is a noble gas element with 99.6% natural abundance of $^{40}_{18}$Ar, a bosonic atom without nuclear spin and electronic hyperfine structure, since it has a closed shell with no net spin-orbit interaction contribution to the Hamiltonian. However, the excitation of an electron results in the open core. The core have total orbital angular momentum $L = 1$ and total spin angular momentum $S = \frac{1}{2}$. Thus, there are two possible spin orbit configurations with $j = \frac{3}{2}$ and $j = \frac{1}{2}$. The first ionization potential corresponding to $3p^5$ $^2P_{3/2}$ ionic state is 127109.9 cm^{-1}. The excited spin orbit ionic state $3p^5$ $^2P_{1/2}$ has the ionization threshold at 128541.3 cm^{-1}. There are two sets of energy states for each series converging to the two ionization thresholds depending upon the spin-orbit configurations of ionic core. This section deals with the photo-excitation of argon atoms to the states in between the ionization thresholds: these are auto-ionizing states. The autoionization was first discovered by Shenstone [65] and White [66] and extended to the alkaline-earths and noble gases. Beyond the series limit lies a continuum of possible energy states which is characterized by the same quantum numbers of L, S, J and parity. The set of discrete energy levels along with the continuum of the series is called a channel. In an independent particle model the electronic states of the atoms and molecules are classified as belonging to a single well defined configuration and a definite value of n and l can be assigned. However, there occurs some disagreement between the theoretical values of the energy levels. The energy levels of the same parity and J-values arising from two close or overlapping configurations perturb each other. Hence, the system is better described by the set of basis states, formed by the mixing of the original functions contributions from different configurations. Such a phenomenon is known as configuration interaction.

The interaction may produce either a resonance or broadening of the spectrum due to the redistribution of the oscillator strength from one spectral region to other. The configuration mixing of a bound state and an overlapping continuum gives rise to autoionization. The bound state has some probability to be found in a continuum. This process in known as autoionization.

Two-step photoexcitation and experimental scheme

An excitation scheme plays a crucial role in the experiment. The ground state of argon has the electronic configuration written as $1s^2 2s^2 2p^6 3s^2 3p^6$ and the term given by $^1S_0$. The ground state terms follows an L-S coupling scheme $^{2s+1}L_J$. However, the excited states are more appropriately designated in a jl-coupling scheme [67, 37]. In this representation, the core electron follows the LS coupling scheme. The total angular momentum of the core couples with the orbital angular momentum of excited electron to give $K = j_{core} + l_{exc}$ with j_{core} is the total angular momentum of the core and l_{exc} is the orbital angular momentum of the excited electron. The K couples with the excited electron spin angular momentum s_{exc} to yield the total angular momentum quantum number $J = K = s_{exc}$. The levels are denoted by $nl^{2s_{exc}+1}[K]_J$. The propensity selection rule for the dipole transitions for one photon transitions are

$$\Delta l = \pm 1$$
$$\Delta K = 0, \pm 1 \tag{176}$$
$$\Delta J = 0, \pm 1$$

with $J = 0 \rightarrow J = 0$ is forbidden

The first excited state arises due to the excitation of one $3p$ electron to $4s$ states. The four possible states are $3p^5(^2P_{3/2})4s$ $^2[3/2]_2$, $3p^5(^2P_{3/2})4s$ $^2[3/2]_1$, $3p^5(^2P_{3/2})4s$ $^2[1/2]_1$ and $3p^5(^2P_{3/2})4s$ $^2[1/2]_0$. The first and the last states are two metastable states belonging to $P_{3/2}$ and $P_{1/2}$ spin-orbit configurations of the ionic cores respectively. We use primed and unprimed terms to represent the terms generated from $^2P_{1/2}$ and $^2P_{3/2}$, respectively. The second excited states $3p^5 4p$ gives rise to ten possible states namely $3p^5 4p$ $^2[5/2]_{3,2}$, $3p^5 4p$ $^2[3/2]_{2,1}$, $3p^5 4p$ $^2[1/2]_{1,0}$, and $3p^5 4p$ $'$ $^2[3/2]_{2,1}$, $3p^5 4p$ $'$ $^2[1/2]_{1,0}$. We make use of one of the metastable states $3p^5 4s$ $^2[3/2]_2$ and $3p^5 4p$ $^2[5/2]_3$ for the purpose of cooling and trapping as this provides a closed transition with 811.755 nm laser light.

Timing of the experiments will be given in detail in the next chapter. Briefly, the
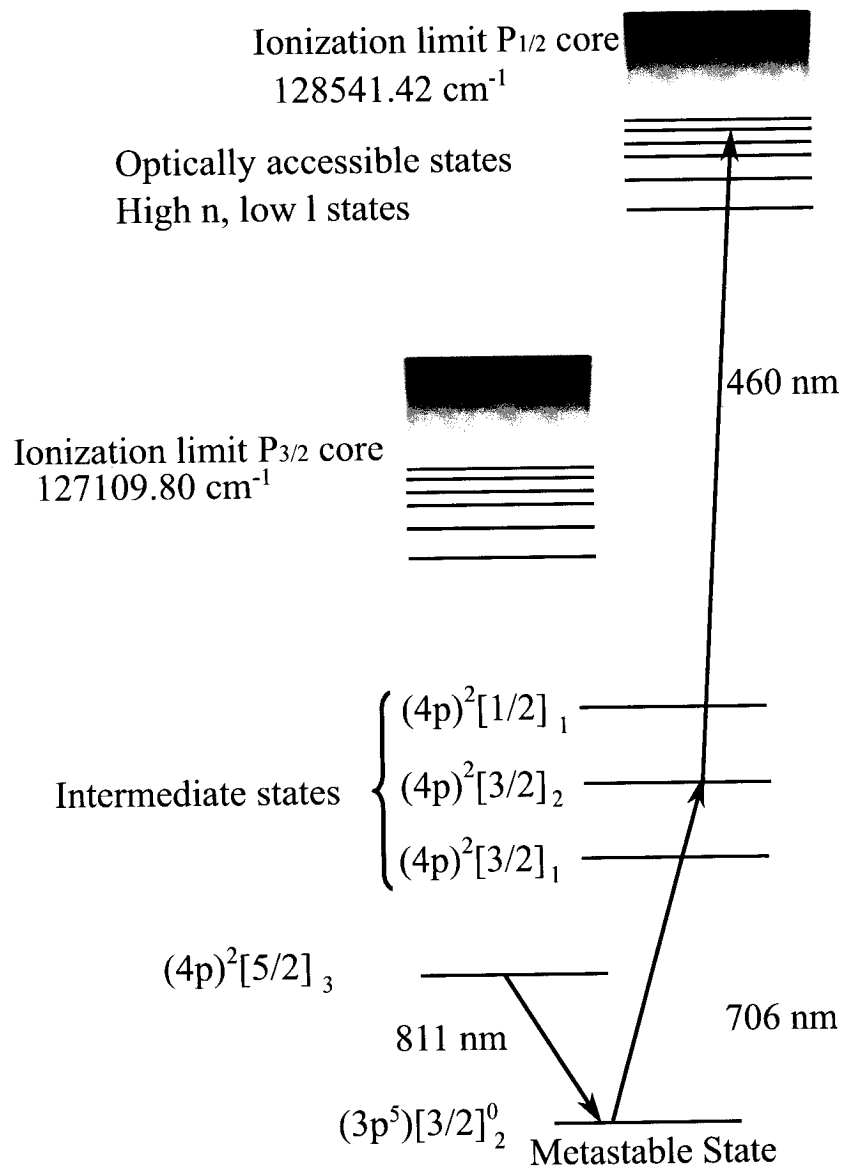
FIG. 41: Experimental procedure for two-color, two-photon excitation scheme for the production of auto-ionizing states of argon.

magneto-optical trap of ultracold atoms is created in the minimum magnetic field region at the intersection of six counter-propagating beams. Then, the experiment is triggered with the flash lamp sync out of the Nd-YAG laser. The slowing and trapping lights are turned off which brings all the excited atoms down to the metastable state $3p^54s^2[3/2]_2^0$. An atom absorbs two photons of two different colors (frequencies) via real states allowing an electron to make a transition to the state not accessible via single photon absorption. This scheme allows us to probe the high lying Rydberg states of an atom lying in single photon (from ground state) UV-XUV region. The atom is excited from the metastable state to any of three possible intermediate levels $3p^54p'^2[1/2]_1, 3p^54p'^2[3/2]_2$ and $3p^54p'^2[3/2]_1$. The atoms can then be excited to very high Rydberg levels corresponding to ns' and nd' autoionizing levels depending the wavelength of the second-step laser.

In our experiment, we excited a fraction of the atoms to the level $3p^54p'^2[3/2]_2$ using the first step laser of ~ 706 nm. The second step photons ≤ 470.55 nm takes the atoms to the high Rydberg states. The second laser is scanned to obtain the spectrum of the autoionization states and for the study of the time evolution of the very highly excited autoionization states, the second step laser wavelength is also kept fixed at values corresponding to the different states and the information about the system is obtained by the collection of the ions as a function of the time. The timing and detection sequence is described in Fig. 54.

III.9 DETECTION SYSTEM

The detection system consists of the ion optics and ion detector (channeltron). The system possesses a high signal to noise ratio hence, even a small signal can be detected. The ions produced in the ionization region are directed towards the channeltron by the home-built ion optics. Our ion optics simply consists of a pair of co-axial rings held by a set of four wires spot-welded symmetrically on the rings and perpendicular to the planes of the rings. The wires extended beyond one of the rings are then spot-welded on the mesh in front of the channeltron. The thickness of the wire is 0.012″ and the diameter of the rings is 10 mm. The similar assembly of the rings and the wires are spot welded on the cylindrical mesh extended from the repeller cage in the QMS/RGA. The ion optics is designed so as to minimize the blocking of the slowing and the trapping laser beams. The ion optics on the QMS/RGA and
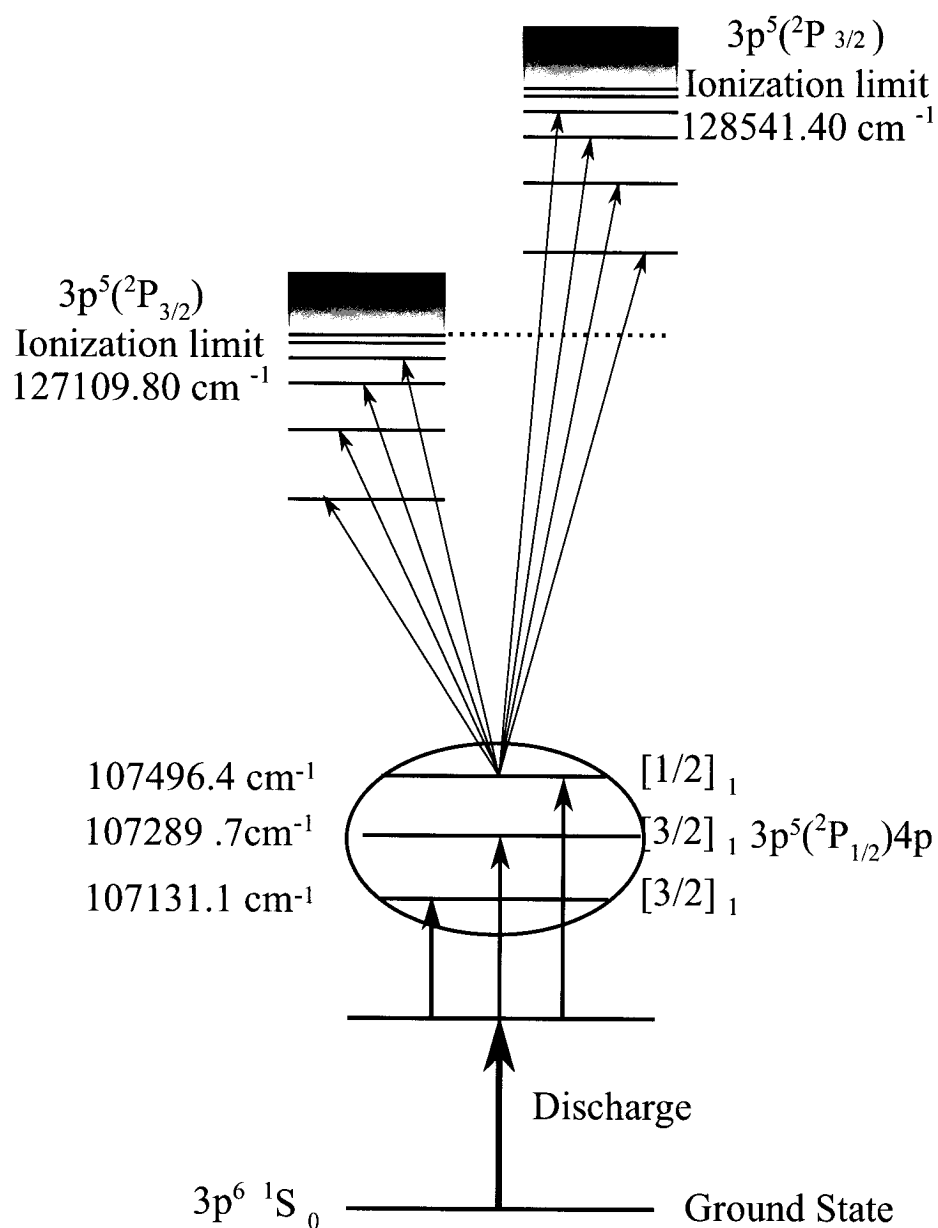
FIG. 42: Two-color, two-photon excitation scheme for the production of auto-ionizing states of argon.
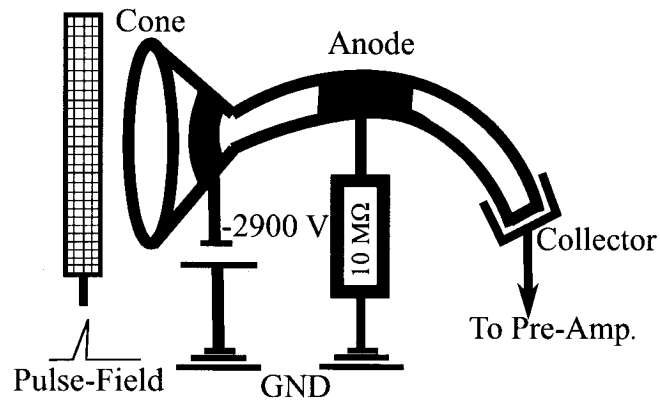
FIG. 43: A circuit diagram for ion counting mode of the channeltron.

channeltron are inserted on the two opposite ports and vacuum sealed with the copper gasket. The separation between the free end rings on the two sets of ion optics is ~ 10 mm.

The channeltron is a horn-shaped continuous dynode structure coated with the electron emissive material on the inside surface and has uniform electric resistance. It is often called continuous-dynode electron multiplier (CDEM). The channeltron (Galileo, 4870V) is operated in the ion counting mode. The circuit diagram is as shown in the Fig. 43.

The CEM is supplied with a high voltage (−2900 V) by an SRS PS350 power supply. With this voltage, the gain of the channeltron can be as high as ~ 10^8, the pulse width is 18 − 20 ns with rise time of 3 − 5 ns. All the connections in the channeltron have been made with high voltage, high vacuum wire via a conflat flange provided with high voltage ceramic insulated feedthroughs. A high voltage is applied between the two extremities of the channeltron to produce a continuous accelerating field along the length. An incident ion travels at high velocity and enters the mouth of the channeltron and impinges on the inner wall creating a shower of electrons. These electrons are then accelerated and collide with the wall again. Each electron causes a secondary shower of electrons. The process continues resulting in an avalanche effect. A metal anode at the other end finally collects the cascade of the electrons resulting in a electric pulse. The output at the collector is fed to the fast preamplifier (SRS-445A, 350 MHz). The pulse undergoes two stage amplification with each stage of gain equal to 5. The direction to the ions produced in the interaction region can
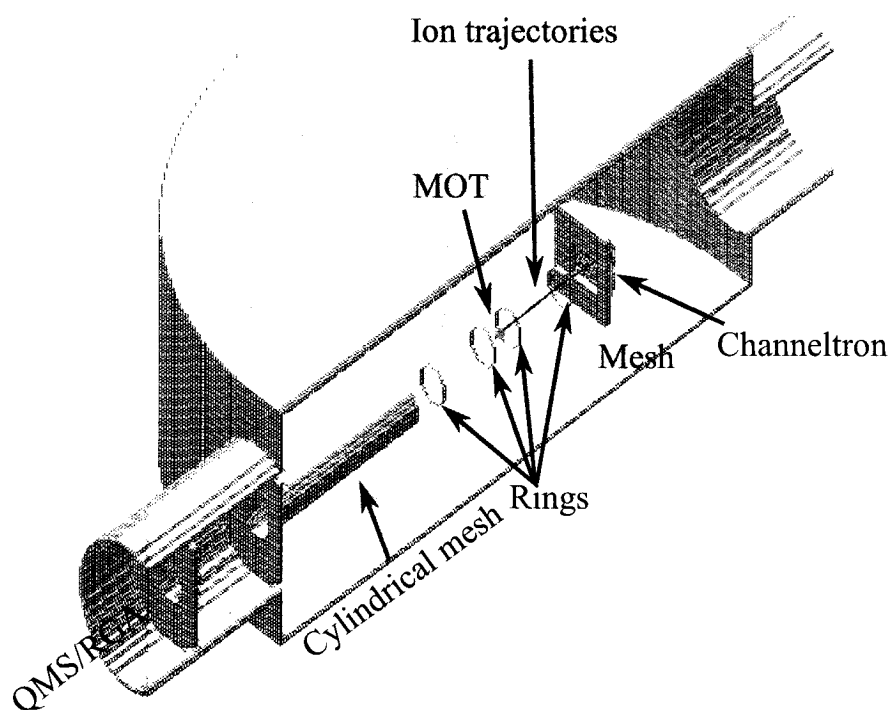
FIG. 44: Schematics of ion optics along with the simulation of the flying ions with zero potential on the ion optics components and -2900 V on channeltron.

be given by adjusting the voltages to the rings. The simulation of the flying ions with 0 V on the ion optics components (rings plus rods) and the channeltron at -2900 V is depicted in the Fig. 44.

CHAPTER IV

RESULTS AND ANALYSIS

IV.1   INTRODUCTION

In this section, we present the results of a set of experiments to explore the creation and survival of long-lived, highly excited Rydberg states, known as ZEKE states. ZEKE states are the long-lived Rydberg states which voilate the usual n^3 scaling law for lifetime due to the l and m-mixing. We have studied these states by exciting ultracold, metastable-state argon atoms confined in a magneto-optical trap to energy regions near an ionization limit of the atom. In the first part of the chapter, we present some additional experimental details specific to the detection of ions from which our signals are derived. We then discuss our first experiment which is a spectroscopic study of the Rydberg states of argon located between the $^2P_{3/2}$ and $^2P_{1/2}$ ionization limits, with particular attention to the effect of electric fields on the spectra. We then present results and discussion of the main part of this dissertation which is the characterization of the creation and survival of ZEKE Rydberg states, which we are able to produce via laser excitation to excited states within ~ 20 cm^{-1} of the second ionization threshold for the excited spin-orbit configuration of the ionic core $^2P_{1/2}$. We conclude the chapter with a discussion of future directions of the research, which include the use of tailored electric fields to study and control an ensemble of ultracold ZEKE state atoms. We present preliminary results for these studies as well as for a fluorescence measurement of Rydberg states in rubidium which sets the stage for future work in that species.

IV.1.1   Ion detection

During the course of the experiments, ions (Ar$^+$ or Ar$_2^+$) can be produced either through direct ionization from a laser, as a result of collisions of highly-excited neutral atoms, or through application of external electric fields in order to field ionize the atoms. The ion optics and channel electron multiplier used to detect these ions is shown in Fig. 45. The ion optics configuration, which consists of two ~ 1 cm rings, allows for the application of an electric field either to intentionally apply a bias or ionization field or to null a stray field. It also permits the rapid extraction of ions produced in the interaction region and directs them to the ion detector.
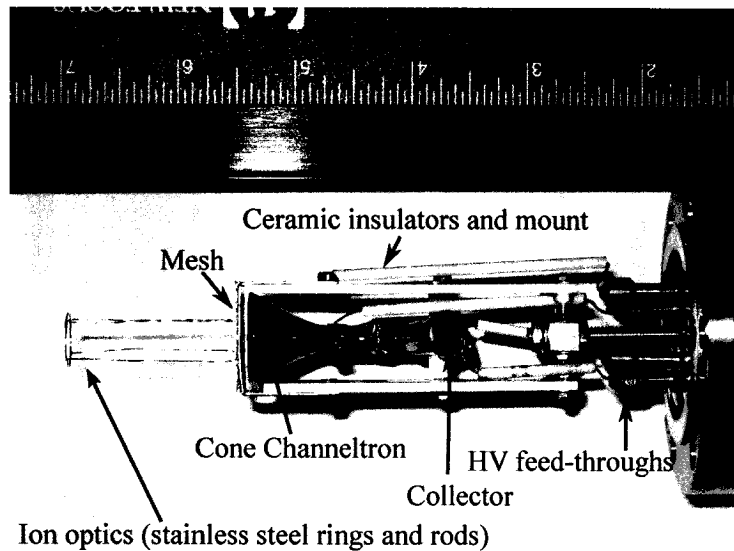
FIG. 45: The channeltron supported in the ceramic mount provided with the mesh and the ion optics in the front.

IV.2 SPECTROSCOPY

Spectroscopy has proved to be a powerful and widely applicable technique for studying physical systems. It has been used extensively as a probe of the energy levels of atoms and molecules. Often, the collection of photons is used as a signature probe, but ions and electrons can also provide valuable spectroscopic information. There are a number of variations of techniques which look at ions and electrons. These include: Photoelectron Spectroscopy (PES), Threshold Photoelectron Spectroscopy (TPES), Resonantly Enhanced Multi-photon Ionization Spectroscopy (REMPI), Pulsed Field Ionization-Zero Kinetic energy Photon spectroscopy (PFI-ZEKE Spectroscopy), and Mass Analyzed Threshold Ionization Spectroscopy (MATI Spectroscopy).

The spectroscopy performed here is done with a two step process. The choice of photon frequency depends on the desired final states. In the case of excitations to the states near the first ionization threshold (the $^2P_{3/2}$ threshold), we use photons at 811 nm and 461 nm to excite the atoms from the state $3p^5(^2P_{3/2})4s\ ^2[3/2]_2 \rightarrow$ $3p^5(^2P_{3/2})4p\ ^2[5/2]_3 \rightarrow$ Rydberg levels below $P_{3/2}$ ionization threshold. In experiments discussed later in this chapter, the first photon of the excitation is produced from a homebuilt pulsed dye laser. In this experiment, continuous-wave (cw) light
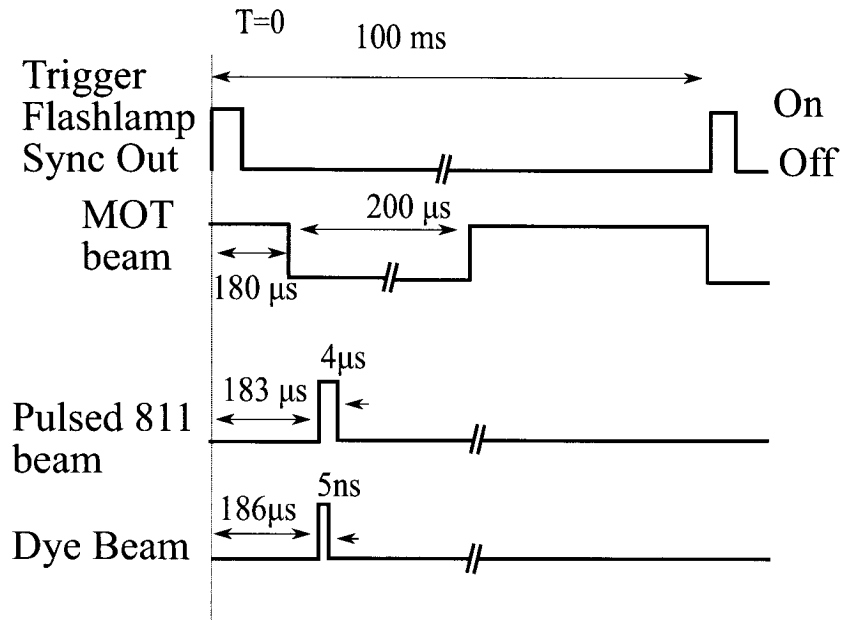
FIG. 46: The timing sequence of the events for the two color two photon spectroscopy of ^{40}Ar with the first step laser wavelength fixed at 811 nm and the scanning second step laser.

from the MOT laser was momentarily placed on resonance and "pulsed" on in the interaction region using an acousto-optic modulator (AOM).

In all of these experiments, timing of the experiment is critical. Spectra are obtained using the timing and detection scheme depicted in Fig. 46. The second step blue dye laser is scanned from 461.5 nm to 466 nm to obtain a spectrum as shown in Fig. 47. The resonances (energy levels) are well identified from $n = 25$ to $n = 42$. Furthermore, the fine-structure is clearly visible and well resolved as seen in Fig. 48. The fine structure is shown below.

$$3p^5(^2P_{3/2})\, 4p\, ^2[5/2]_3 \rightarrow \begin{cases} 3p^5(^2P_{3/2})nd\, ^2[7/2]_{4,\,3} \\ 3p^5(^2P_{3/2})nd\, ^2[5/2]_{3,\,2} \\ 3p^5(^2P_{3/2})ns\, ^2[3/2]_2 \end{cases}$$

IV.2.1   Spectroscopy of argon below $P_{3/2}$ ionization threshold

As a reminder, ultracold atoms of metastable argon are cooled and trapped at the intersection of six counter-propagating beams with a pair of counter-propagating

beams along each orthogonal axis in three dimensional space. An anti-Helmoltz coil provide an inhomogeneous magnetic field to give rise to a spatially dependent force on the atoms by Zeeman shifting the atom's magnetic sub-levels. Data is taken at 10 Hz which is the repetition rate of the pulsed laser source. For each data point, the cycle begins with the flashlamp trigger of the Nd-YAG laser (Quantel Brillant) which we call $t = 0$. The trapping and Zeeman slower light is turned off (using an AOM) 180 μs later, about the time that the laser is internally Q-switched. The atoms in the excited state decay back to the metastable state $3p^5(^2P_{3/2})4s\ ^2[3/2]_2$. The pulsed 811 nm light comes on at 183 μs for 4 μs to excite the maximum possible fraction of atoms to the intermediate state $3p^5(^2P_{3/2})4p\ ^2[5/2]_3$ (the transition is saturated). The Q-switch of the Nd-YAG laser arrives at 186 μs. A second and third harmonic crystal module converts the 1064 nm light to 355nm light. The fundamental wavelength is separated from the harmonics on a set of dichroic beam splitters. The 1064 nm fundamental is sent to a beam dump, whereas the 532 nm is directed to a homebuilt dye laser. The 355 nm light pumps Coumarin- 460 laser dye to produce the photon needed for the second step of the excitation. The blue dye beam $\sim$ 470 nm is focussed onto the MOT and optimized for the maximum ion count as monitored with the channeltron on a photon counter. The ions are sent to the channeltron by applying a pulsed electric field in the interaction region. This rise time of the electric field is 1.25 μs and the amplitude of the voltage applied to one of the rings is -62.8 V, giving a slew rate of 50.34 V/μs. The onset of the pulsed electric field is at 187 μs after the trigger and remains on for 1 ms. The signal is amplified 25 times using a fast pre-amplifier (Stanford Research SRS-445 A, 350 MHz). After optimization, the second step laser is scanned to yield the spectrum as shown in Fig. 47.

The scanning of the second step laser at slow speed produces the well resolved spectrum as shown in Fig. 48. The fine structure is well identified. Our results are found to be in excellent agreement with other groups and are summarized in Table. V, along with a comparison to previously published results. The quantum defects for the various s and d fine structure states are found to be independent of the principal quantum number and are strongly dependent upon the orbital angular momentum quantum number, as expected. Results are shown in Fig. 49. However, the pulsed electric field of ~ -45.8 V/cm, used for the ionization and extraction is not sufficient for the ionization of the low lying state of $n = 25$. The possible mechanism includes

FIG. 47: Rydberg spectrum of ^{40}Ar obtained via two color, two photon transitions using 811 nm and $\sim$ 461 nm as first and second step excitation laser.

FIG. 48: The resolved Rydberg spectrum of ^{40}Ar obtained via two color, two photon transitions using 811 nm and $\sim$ 461 nm as first and second step laser for excitation from $n = 25 - 30$.
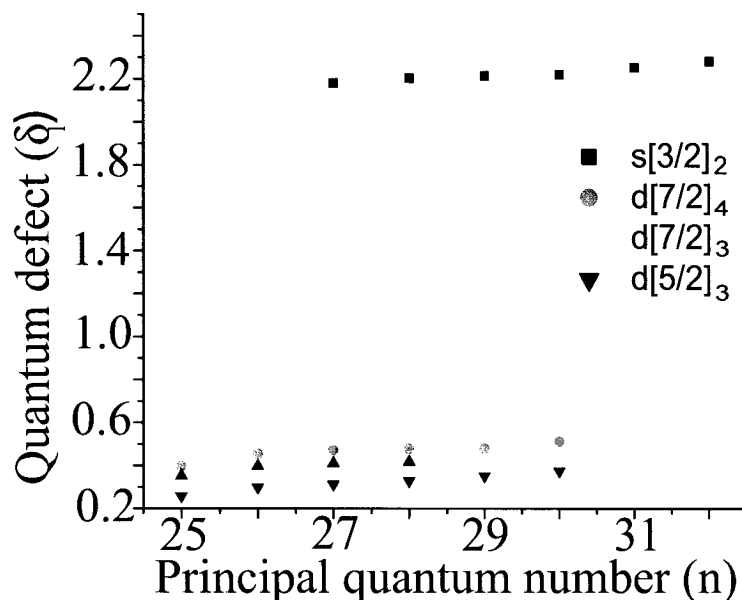
FIG. 49: The quantum defects calculated from the resonance obtained in the spectrum Fig. 48.

the multiphoton and BBR-ionization.

IV.2.2 Stark effect in Rydberg states

The simplest case of the Stark effect involves the investigation of the electric field in the alkali-metals and alkaline-earth atoms because of the single Rydberg electron and the isotropic ionic core. However, the study of such phenomenon in noble gases imposes a complex physical situation, since the ionic core does not remain isotropic after the excitation of a closed-core electron to a Rydberg state.

In order to observe the influence of the electric field present during the photo-excitation to the Rydberg states, one of the rings on our ion optics arrangement (the one attached to the channeltron assembly) is set to different potential offsets (applied voltages) while the ring on the other side is grounded. The electric field in the interaction region is a function of applied voltage and the ring geometry. We used the Simion 7 ion trajectory simulation to compute the trajectories of ions produced in the interaction region and to characterize our ion detection efficiency with respect to ion collection. Spectra for atoms excited in the presence of the bias fields of 0

TABLE V: Comparison of our data with the data form N. Piracha [68] and M. Aslam [69] for the states below $P_{3/2}$ ionization threshold with P and A indicating the data source for Piracha and Alsam, respectively.

n	source	$s[3/2]_2$	$d[7/2]_4$	$d[7/2]_3$	$d[5/2]_3$
25	our data		126928.4821	126929.1779	126930.5419
	P		126928.56	126929.36	126930.56
	A				126928.8
26	our data		126941.6315	126942.4019	126943.6616
	P		126942.36	126942.96	126944.16
	A				126942.6
27	our data	126931.689	126953.8871	126954.5892	126955.7116
	P	126932.16	126945.56	126955.16	126956.16
	A				126955.0
28	our data	126944.9213	126964.9314	126965.5649	126966.4758
	P	126945.56	126965.56		126966.96
	A				126965.9
29	our data	126956.8666	126974.8995		126976.0936
	P	126957.36	126975.36		126976.56
	A				126975.7
30	our data	126967.5995	126983.6078		126984.7657
	P	126967.96	1269784.16		126985.36
	A				126984.8
31	our data	126977.0054			
	P	126977.56			
	A				
32	our data	126985.5393			
	P	126986.36			
	A				

V/cm, -22 V/cm, -29 V/cm and -36 V/cm are obtained by the application of pulsed electric fields with slew rate of 50.34 V/μs and maximum amplitude of -62.8 V is shown shown in Fig. 50.

As can be seen from the figures, the presence of the electric field dramatically alters the spectra. Viewed from another angle, the spectroscopy can be used to probe electric fields in the interaction region. As we describe later in the chapter, the presence of electric fields is critically important for the production of long-lived Rydberg states, so the ability to characterize the electric field seen by the atoms - both from time-independent stray fields and time-dependent fields originating from nearby charged particles is very important. Spectroscopy of the Rydberg states provides that ability.

IV.2.3   Auto-ionizing regime

Next we turn our attention to the study of both the structure and the dynamical aspects of the highly excited Rydberg auto-ionizing levels of argon. We begin by presenting results from a spectroscopic study similar to the one described in the previous section. Whereas there, excitations were to levels just below $^2P_{3/2}$ ionization threshold, here excitations are to a region above the $^2P_{3/2}$ limit and just below the $^2P_{1/2}$ ionization limit.

In this experiment the first step photon excites the atoms from the metastable state to one of three dipole allowed intermediate states: $^2P_{1/2}4p[1/2]_1$ or $^2P_{1/2}4p[3/2]_1$ or $^2P_{1/2}4p[3/2]_2$. The second step photon excites to Rydberg levels in the region between the first $P_{3/2}$ and second $P_{1/2}$ ionization thresholds. We mainly focused our study on the Rydberg levels lying close to the second ionization threshold. Consequently, the Rydberg spectra built on each of the three intermediate levels have been separately observed. The first step laser is produced using a home-built flowing dye laser which is fixed for the excitation to the intermediate levels and the second step laser beam is produced using the continuum dye laser with just an oscillator and no amplifier. The linewidth of the second step laser, which is a commercial laser is estimated to be near the manufacturer's specification of ~ 0.1 cm^{-1}.

The flashlamp sync out from the Nd-YAG laser triggers a pulse generator (Quantum Composers) at $t = 0$. The trapping light and slowing light is turned off at $t = 0$. The ultracold atomic cloud expands ballistically and the density of the magneto-optical trap is slightly reduced. The Q-switch on the Nd-YAG laser is set to the
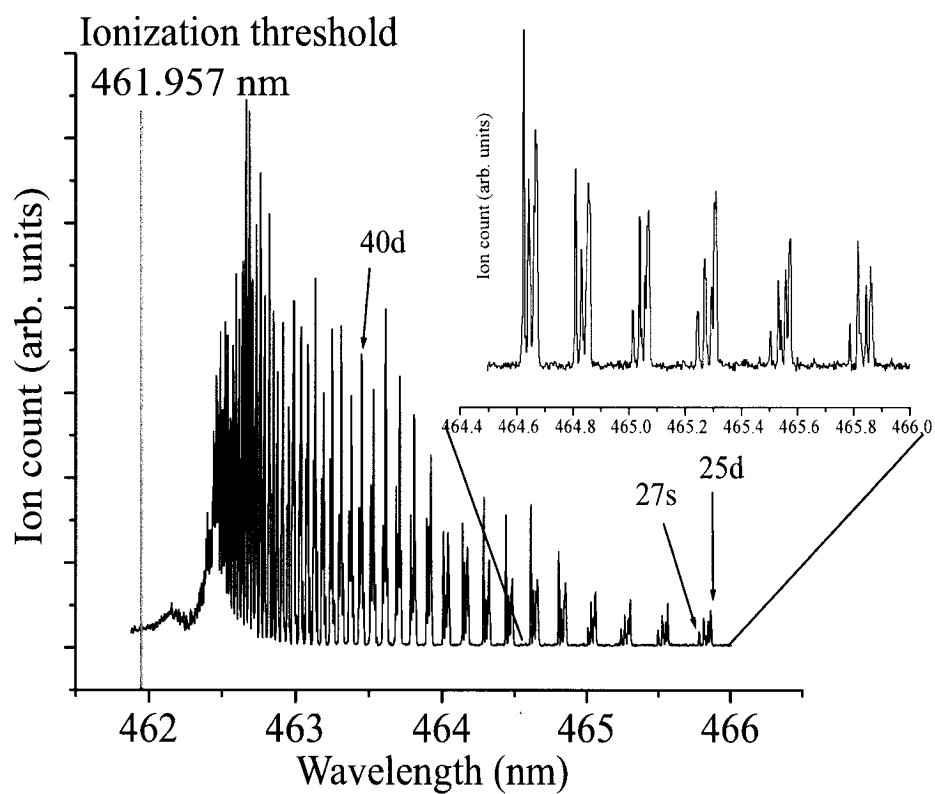
Ionization threshold
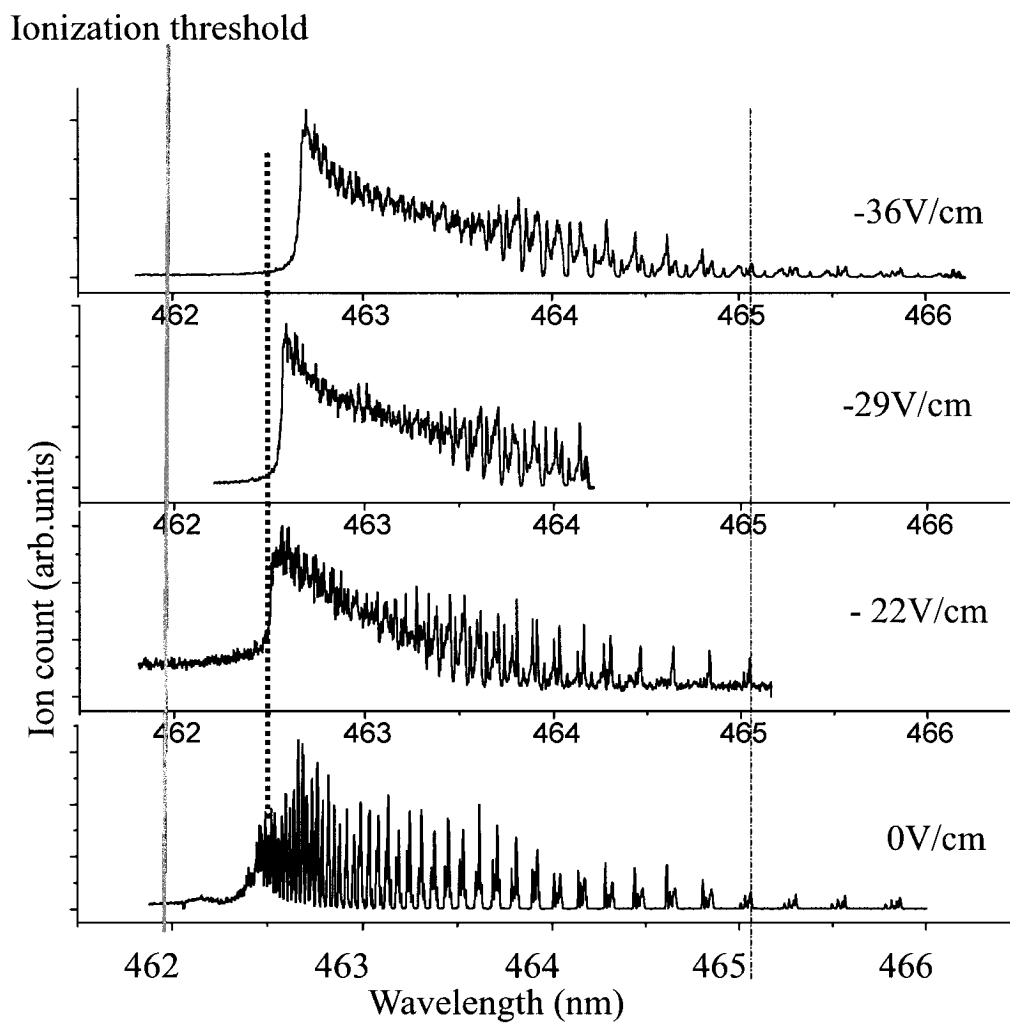
FIG. 50: Rydberg spectrum of ^{40}Ar obtained via two color, two photon transitions using 811 nm and $\sim$ 461 nm as first and second step excitation laser in various bias electric fields.
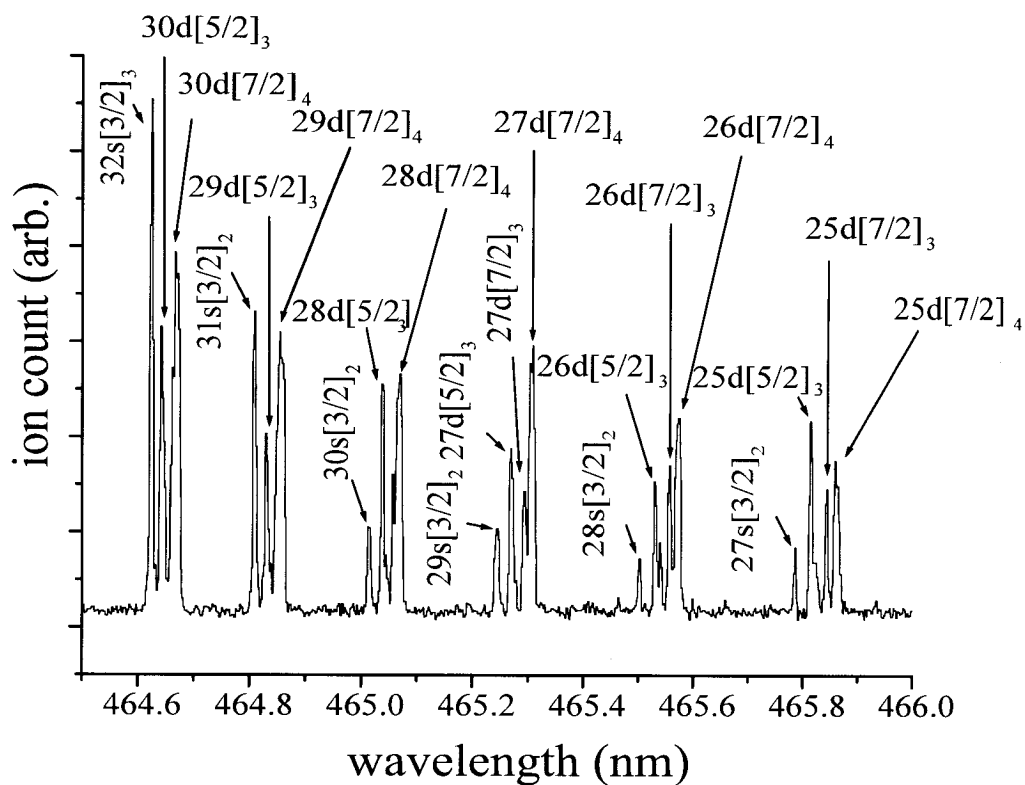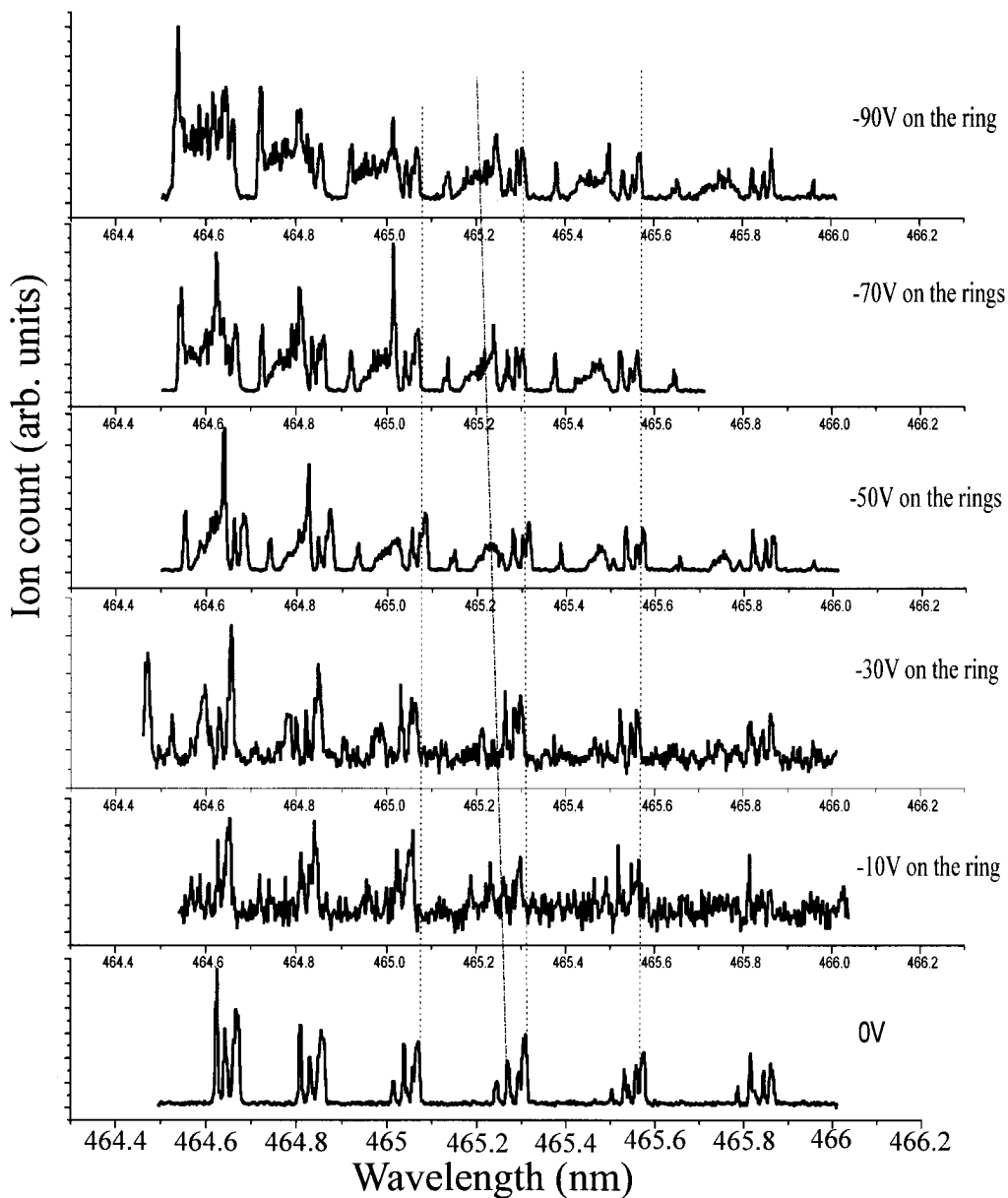
FIG. 51: Rydberg spectrum of ^{40}Ar obtained via two color, two photon transitions using 811 nm and $\sim$ 461 nm as first and second step excitation laser for n=25 to n=30 in the various bias electric fields.
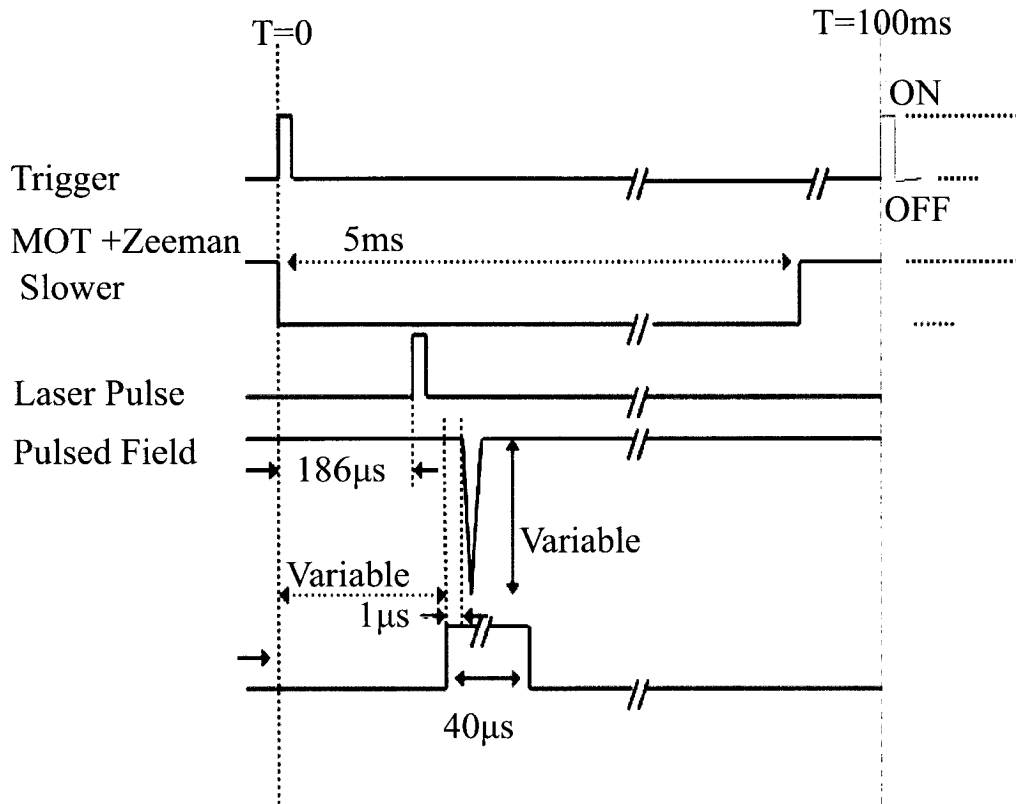
FIG. 52: The timing scheme for the data acquisitions.

delay of 186 μs and operates at a repetition rate of 10 Hz. The output pulse has a width of 5 ns. The second and third harmonics beams pumps the respective dye laser setups discussed in Secs. III.7.2 and III.7.1 respectively to produce the first and second step laser beams, respectively. The first and second dye laser beams have the energies of 100-200 μJ/pulse and $\sim$ 1.5 mJ/pulse respectively at the interaction region. This excites the atoms to the Rydberg states. A pulsed electric field with a slew rate and amplitude of 50.24 V/μs and -62.8 V is turned on 187 μs after the flashlamp (ie, 1 μs after the photo-excitation). The timing scheme of the events in the experiment is depicted in Fig. 52 and the schematic of the data acquisition is shown in Fig. 54. The spectra obtained by scanning the second step laser are shown in the Fig. 53.
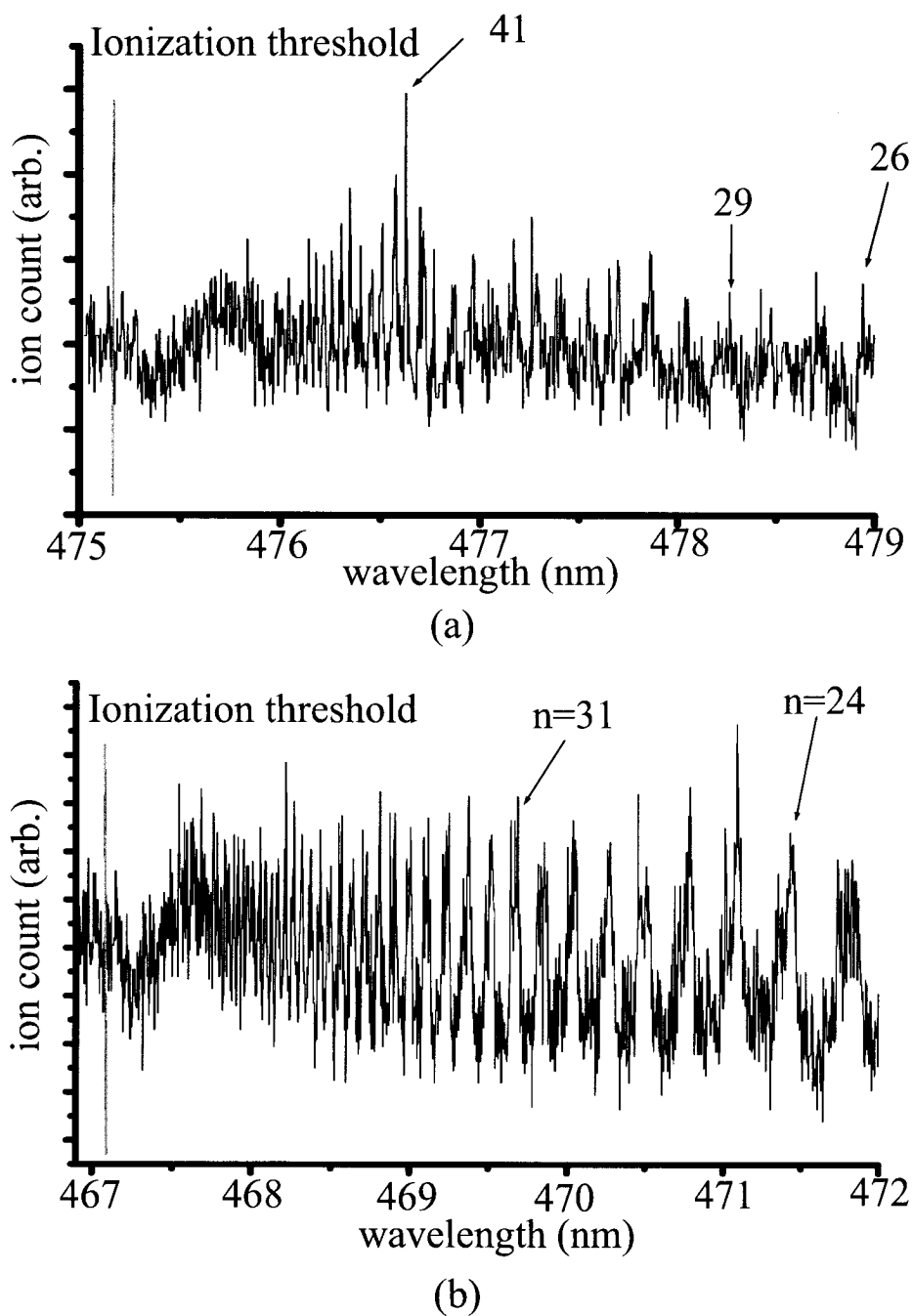
FIG. 53: The Rydberg spectrum of ^{40}Ar obtained via two color, two photon transitions using (a) $3p^5(^2P_{3/2})\ 4s\ ^2[3/2]_2 \rightarrow 3p^5(^2P_{1/2})\ 4p\ ^2[1/2]_1 \rightarrow$ *Rydberg state* using ~ 696 nm and ~ 475 nm as first and second step excitation laser and (b) $3p^5(^2P_{3/2})\ 4s\ ^2[3/2]_2 \rightarrow 3p^5(^2P_{1/2})\ 4p\ ^2[3/2]_1 \rightarrow$ *Rydberg state* using ~ 714 nm and ~ 467 nm as first and second step excitation laser respectively.

$$3p^5(^2P_{3/2})\,4s\,^2[3/2]_2 \longrightarrow \quad 3p^5(^2P_{1/2})\,4p\,^2[1/2]_1 \to \begin{cases} 3p^5(^2P_{1/2})nd\,^2[3/2]_{2,\,1} \\ 3p^5(^2P_{1/2})ns\,^2[1/2]_{1,\,0} \end{cases}$$
$$\sim 696nm$$

$$3p^5(^2P_{3/2})\,4s\,^2[3/2]_2 \longrightarrow \quad 3p^5(^2P_{1/2})\,4p\,^2[3/2]_1 \to \begin{cases} 3p^5(^2P_{1/2})nd\,^2[5/2]_{3,\,2} \\ 3p^5(^2P_{1/2})nd\,^2[3/2]_{2,\,1} \\ 3p^5(^2P_{1/2})ns\,^2[1/2]_{1,\,0} \end{cases}$$
$$\sim 714nm$$

$$3p^5(^2P_{3/2})\,4s\,^2[3/2]_2 \longrightarrow \quad 3p^5(^2P_{1/2})\,4p\,^2[3/2]_2 \to \begin{cases} 3p^5(^2P_{1/2})nd\,^2[5/2]_{3,\,2} \\ 3p^5(^2P_{1/2})ns\,^2[1/2]_1 \end{cases}$$
$$\sim 706nm$$

The relative intensities of transitions to the d-levels appears to be stronger than the intensities of transitions to the s-levels in Fig. 55. Our investigation begins with the identification of the auto-ionization resonances. The resonances are compared with the data from Piracha [68] and Aslam [69].

The pulsed electric field for the ionization and extraction of the ions has the maximum amplitude of -62.8 V which is equivalent to the ~ -45.8 V/cm at the interaction region. The field is not enough to field ionize the low lying levels of $n = 20$. However, the resonances still appears for such levels. The most likely mechanism is the rapid auto-ionization and the other possible mechanisms of the ionization include multi-photon ionization, collisional ionization and black-body radiation ionization. The spectrum provides the wavelength landmarks to set the wavelength of the second step photon for Rydberg transition to the defined quantum levels. Fine structures are not resolved in the spectrum of Fig. 55 as they fall close enough to each other and limited by the line width of the lasers ≥ 0.1 cm^{-1}.

IV.2.4   ZEKE spectroscopy and ZEKE-Zero Kinetic Energy states

The basic idea of the original ZEKE spectroscopy is to collect and detect only the emitted electrons with near zero kinetic energy. It provides a significantly high resolution spectroscopy. The key to the good resolution of ZEKE or ZEKE-PFI is its discrimination against electrons with non-zero kinetic energy. The technique has a number of forms, but in essence involves exciting atoms or molecules with a
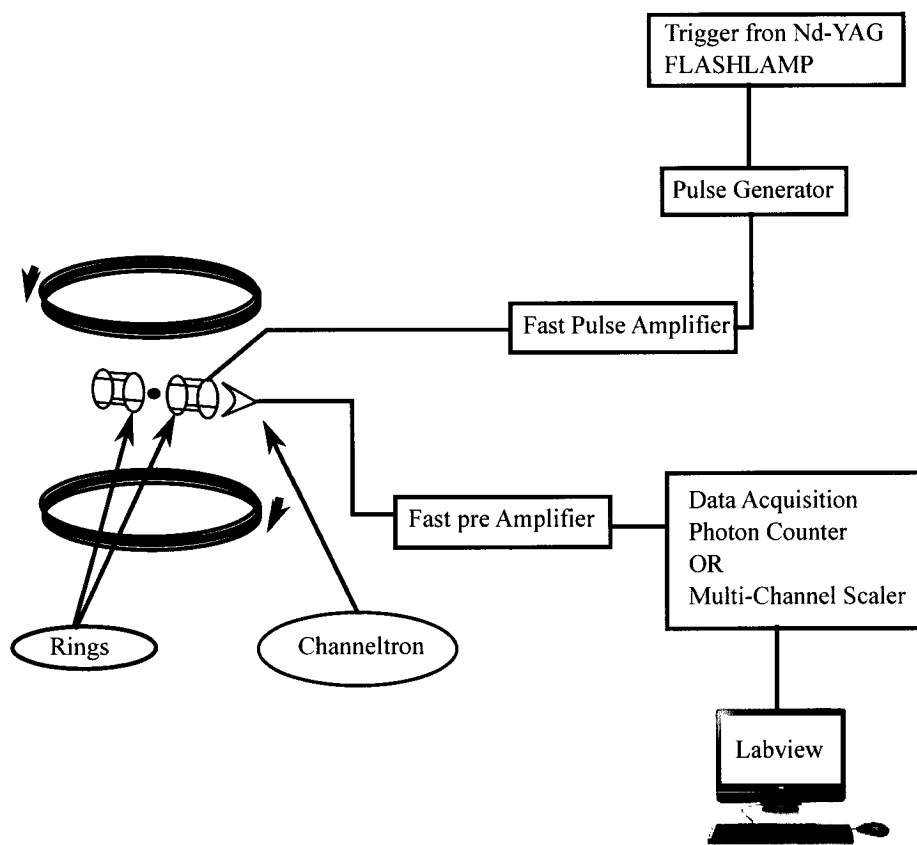
FIG. 54: The setup for data acquisition.

TABLE VI: Comparison of our data for the excitation with the data from N. Piracha [68] and M. Aslam [69] for the states below $P_{1/2}$ ionization threshold with P and A indicating the data source for Piracha and Alsam, respectively.

| n	source	$s'[1/2]_1$	$d'[3/2]_2$	$d'[5/2]_2$	$d'[5/2]_3$
	our data		128258.0434		
20	P		128256.865		
	A	128197.7	128256.9	128257.2	128258.3
	our data		128285.1137		
21	P				
	A	128233.4	128283.9	128283.6	128285.0
	our data	128263.4879	128308.0298		
22	P				
	A	128263.7	128307.0	128307.2	128308.0
	our data	128290.7432	128328.1673		
23	P				
	A	128289.5	128327.4	128327.5	128328.3
	our data	128311.9357	128345.7272		
24	P		128345.065		
	A	128311.7	128345.3	12844.9	128345.8
	our data	128331.4608	128361.6025		
25	P		128360.465		
	A	128331.6	128360.5	128361.1	128361.1
	our data	128348.9199	128375.5185		
26	P				
	A	128348.6	1283374.6	1283374.3	1283375.0
	our data	128364.3069	128387.9706		
27	P		128387.065		
	A	128364.0	128386.9	128386.7	1283386.9
	our data	128377.088	128398.9088		
28	P		128397.465		
	A	128377.4	128397.6	128397.9	128398.0
	our data	128390.0814	128408.7834		
29	P		128407.265		
	A	128389.3	128407.8	128407.7	128407.9
	our data	128400.733	128417.4754		
30	P				
	A	128400.0	128416.8	128416.8	128416.7
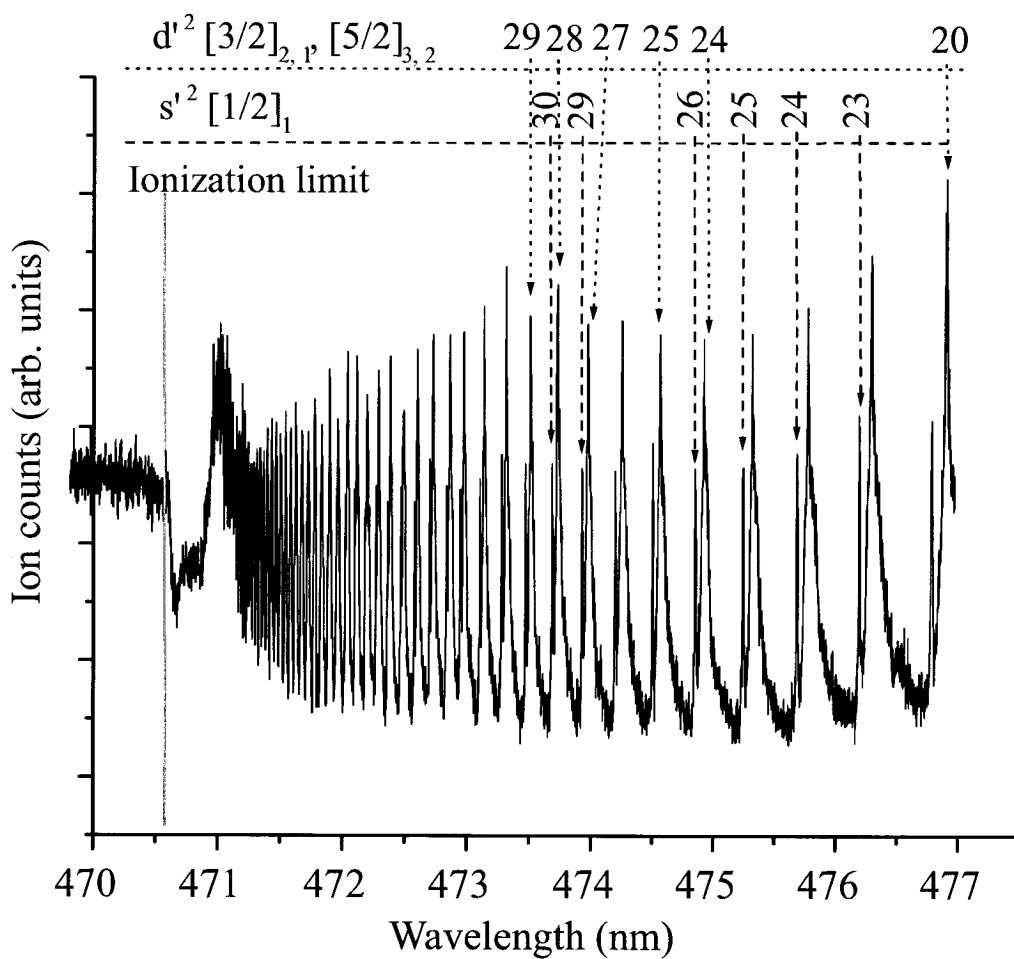
FIG. 55: The Rydberg spectrum of ^{40}Ar obtained via two color, two photon transitions using $3p^5(^2P_{3/2})$ $4s$ $^2[3/2]_2 \rightarrow 3p^5(^2P_{1/2})$ $4p$ $^2[3/2]_2 \rightarrow$ *Rydberg state* using ~ 706 nm and ~ 470 nm as first and second step excitation respectively.

pulsed source, waiting a delay time, and then applying an electric field to sweep any electrons (or ions) which remain in the interaction region after the delay time into a detector. If, for example, the laser used to photo-ionize the atoms is tuned significantly above the ionization threshold, then the excess energy will go mainly to the electrons which will quickly (as compared to the delay time) leave the interaction region. On the other hand, when the laser is tuned exactly at the ionization threshold limit, near zero kinetic energy electrons are produced and they do not leave the interaction region during the delay time. Therefore, the delayed pulsed field collects these electrons and reveals the location of the ionization threshold. Refinements of these techniques included excitations to just below the ionization limit followed by pulsed field ionization. When these Rydberg state excitation experiments were first done, however, several groups discovered that the high-n Rydberg states in a range of ~ 20 cm^{-1} below the ionization threshold had anomalously long lifetimes. In fact, lifetime of the order of several tens of microseconds were seen when lifetimes of less than 1ns were expected. These unusual states became known as "ZEKE Rydberg states." These high-n Rydberg states $\sim 10 - 20$ cm^{-1} below the ionization threshold possess some unique properties. The physical nature of the ZEKE states has been the subject of intense experimental and theoretical investigation.

We believe that ZEKE states could have an important and unique role in the dynamics of ultracold plasmas, and so we set out to study these states by creating them from atoms in the argon MOT. The work reported here represents the first investigation of the lifetimes of *ultracold* ZEKE Rydberg states.

IV.2.5 Ion transport

In a preliminary experiment to characterize the transport of ions produced through field ionization of ZEKE states, the following experiment was performed: ultracold argon atoms in the MOT are photo-excited using the same previously discussed two color, two photon transitions using the $3p^5(^2P_{1/2})$ $4p\,^2[3/2]_2$ state as an intermediate state. The second step photon wavelength is parked so as to excite the atoms to the $n = 90$ Rydberg state with a laser pulse energy of 1.35 mJ/pulse. 100 μs after the ZEKE states are created, a pulsed field with a of slew rate of -50.4 V/μs is applied. The arrival of ions at the channeltron is monitored on a multichannel scaler (Stanford Research SR430). The multichannel scalar is triggered with the delay of 180 μs after the flashlamp of the Nd-YAG laser. The results are shown in in Fig.
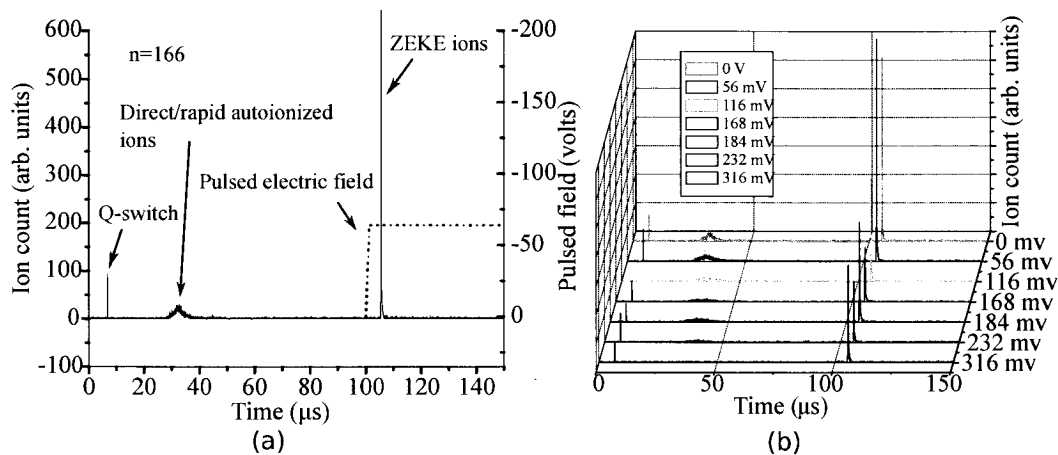
FIG. 56: (a) The fast ion signal due to direct and auto-ionization and the ZEKE signal at energy level n=90, after the application of pulsed electric field at 96 μs (b) the variation of the fast signal as a function of the bias field.

56(a).

Notice that at a delay time of $\sim$ 27 μs (with respect to the laser pulse) an ion signal appears on the detector. These ions are those which are produced during the laser pulse through excitation to Rydberg states which auto-ionize immediately and also possibly to a lesser extent a few from multi-photon ionization. The second peak is the result of ions which have been created from field-ionization (with -62.8 V placed on the ring) of the long-lived ZEKE Rydberg states.

The difference between the ionization thresholds is 1431.61 cm^{-1}. If a Rydberg atom auto-ionizes, this excess energy shows up as kinetic energy of the electron and ion. Due to the mass difference between the ions and the electrons, though, the ions only carry a very small fraction of the energy m_i/M with m_i and M being the masses of ions and the total mass of the atom respectively. To first approximation, the ions have a kinetic energy of 2.43×10^{-6} eV which gives an approximate speed of 3.429 m/s. The distance of the mesh in front of the channeltron is 40 mm from the interaction region and the freely flying ions should take $\sim$ 11.66 ms to reach the detector. However, the ions are arriving and are detected after a delay of 27 μs. This suggests that there may be a leakage field due to the potential of the channeltron cone and possibly some additional stray fields. To test this idea, a small bias voltage was placed on the ring closest to the channeltron. And indeed as a positive bias field

is applied, the ion signal starts to disappear. It seems to completely disappear at the applied potential of 316 mV as seen in Fig. 56(b).

IV.2.6 ZEKE Rydberg state lifetimes vs. n

In the next experiment, the wavelength of the second step laser beam is set for the transition to different highly excited auto-ionizing levels ranging from $n = 70$ to 10 cm^{-1} (wavenumbers) above the ionization threshold. For each excitation, the delay of the pulsed electric field for the ionization and extraction is scanned (along with the ion collection gate 700 μs wide). This allows us to map out the survival of the ZEKE states by counting the number of excited state atoms which remain after a given delay time.

Throughout this section we will refer to the ZEKE state "lifetime". What we are measuring is how long the ZEKE states survive after being created. Such survival depends on a number of factors. An isolated Rydberg atom will radiatively decay, but other mechanisms like collisions or interactions with photons or fields can also result in the destruction of the ZEKE state. The use of the word *lifetime* here refers to the survival lifetime of the ZEKE states under the environmental conditions in which they were created, not simply the radiative or natural lifetime.

The scanning step of the collection gate and the pulse field delay is 5 μs and 100 records/step. The scan range is a delay time of $0 - 200$ μs. Each of the repeated experimental runs have been performed using the photon counter with extreme care so as to keep the experimental conditions identical as much as possible. These parameters include the energies of the laser beams, the stray fields, the position of the MOT and the operating pressure of the Ar* discharge. The powers of the lasers are 200 μJ/pulse and 250 μJ/pulse for the first and second dye laser beams respectively operating at 10 Hz. The pulsed field delay is scanned from $t = 0$ μs to $t = 250$ μs in the scan step of 5 μs for the different wavelengths of the second step lasers corresponding to transitions to the different quantum levels is shown in the Fig. 57. The decay curves of these states clearly depends on the states.

IV.2.7 Analysis of the ZEKE Lifetime data

It is obvious in the close-up of Fig. 57 shown in Fig. 58, the plot starting from the lower onset of the ZEKE states region that the atoms are auto-ionized fast and then no signal appears at later times. As the principal quantum number of the excitation
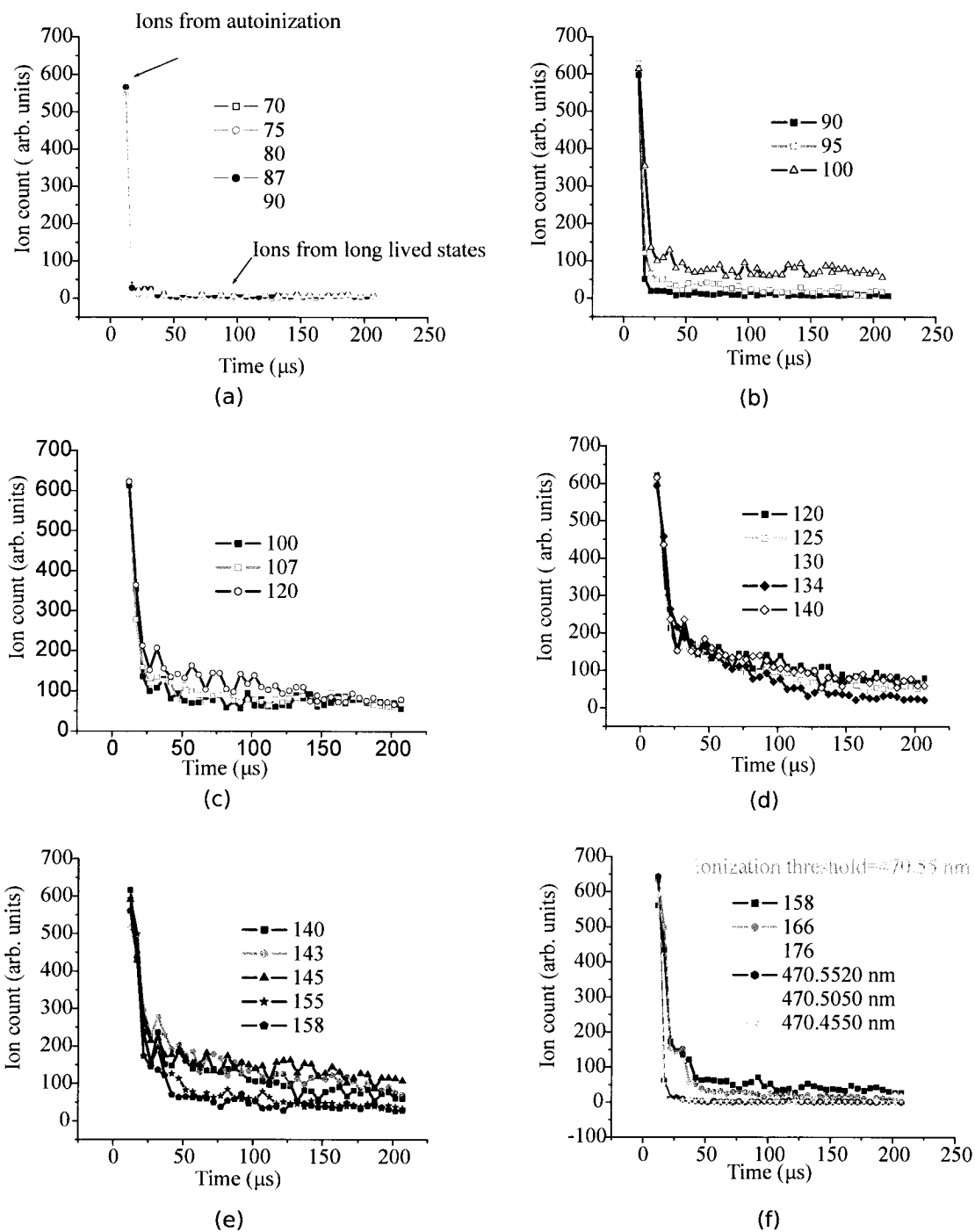
FIG. 57: The formation and survival of the ZEKE states when excited to different energy states.
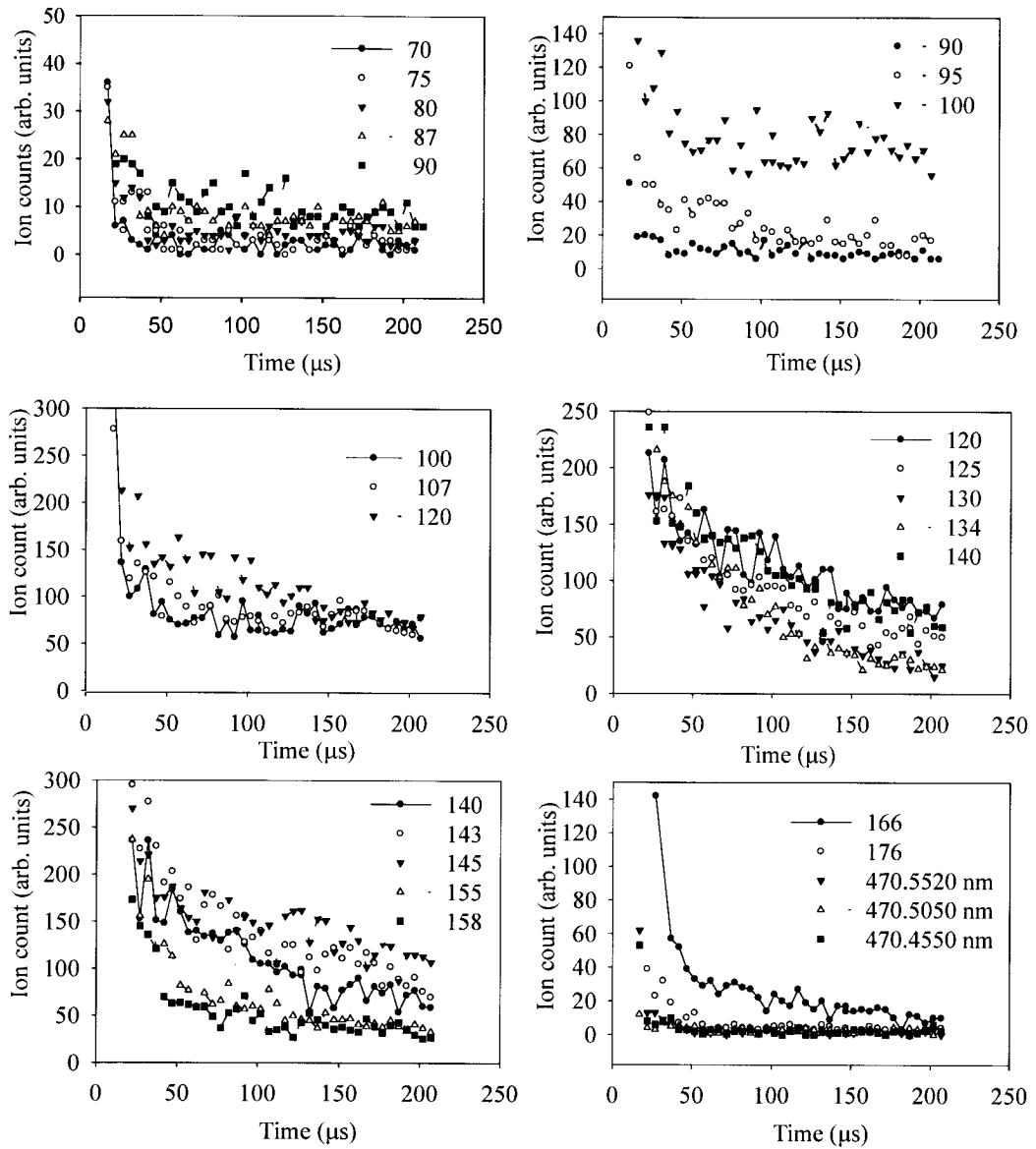
FIG. 58: Closeup view of the formation and survival of the ZEKE states when excited to different energy states.

is increased, however, more and more signal begins to appear at later times. In other words, the ZEKE Rydberg states are surviving longer. At some point, however, this trend reverses and the ZEKE state survival lifetime begins to *decrease*. Finally, at very high levels above $n = 179$, the ZEKE signal completely vanishes. As we discuss later, there is more than one mechanism which can cause the ZEKE Rydberg states to be destroyed. In an effort to provide a simple characterization of the ZEKE state lifetime as a function of the principal quantum number, we have fitted the lifetime curve with a simple exponential. We find, in fact, that a simple exponential does a good job of characterizing the ZEKE state survival as shown in the Fig. 59. Note that for the fit, we have removed the data points before 32 μs to get rid of the contribution from the direct or fast auto-ionized ions. The lifetimes obtained from the curve-fitting is plotted against the principal quantum number as shown in Fig. 60. For low lying states in the bottom of the ZEKE-region, very few or no ions are collected after the delay of 32 μs. While this could mean that such states are created then rapidly destroyed, it is more likely that this reflects a cutoff in the ZEKE state production.

IV.2.8   Physical explanation for ZEKE state production

The creation of the long-lived ZEKE Rydberg states observed in these experiments can be understood as follows: Rydberg atoms are being transferred from their optically accessible initial low angular momentum states ($l = 0$ or 2) into a statistical mixture of lm states. The mechanism for the transformation of the low- l and m states into the high-l and m states is the presence of any stray fields and the electric fields provided by charged particles originating from the fast auto-ionization of the low-l Rydberg states. Recall from Sec. II.6.2, that a uniform electric field will mix l states to create Stark states. If the field configuration does not possess cylindrical symmetry, then m is also no longer a good quantum number. Furthermore, any non-uniform time-dependent electric fields resulting from bypassing early electrons mix the low l states with the high l states [70]. The early electrons and ions are produced by the fast auto-ionization of the low-l Rydberg states which takes place within the order of 10^{-11} s for $n \geq 10$. The velocities of the early auto-ionized electrons are on the order of 10^4 m/s the maximum being 2.5×10^4 m/s. The early ions originating from the auto-ionization move only on the order of 10 nm in 5 ns in a field free region. Hence, the ion motion does not contribute to the m mixing of the levels. It should
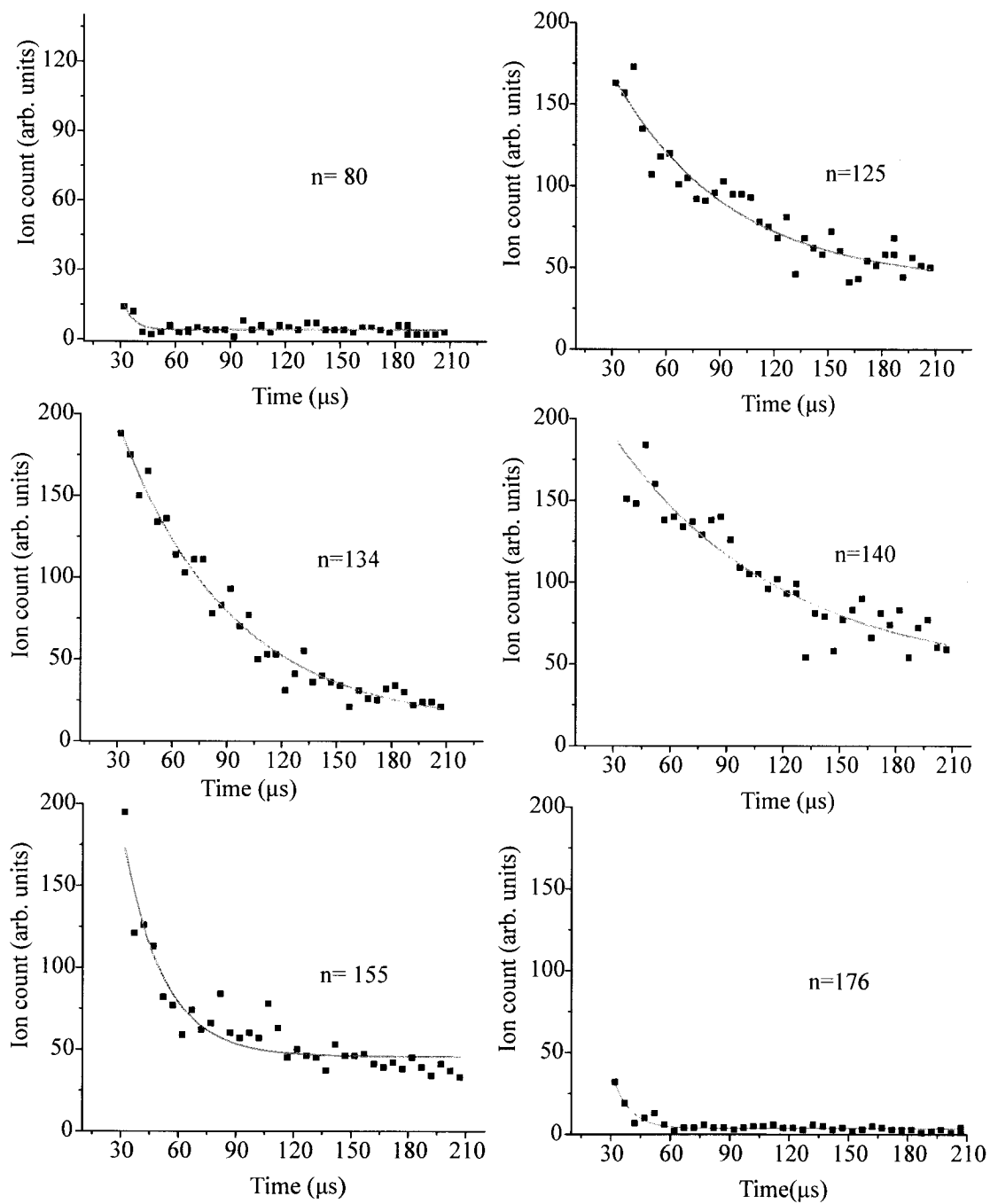
FIG. 59: Single exponential curve-fitting to the experimentally obtained data for the lifetimes of ZEKE states.
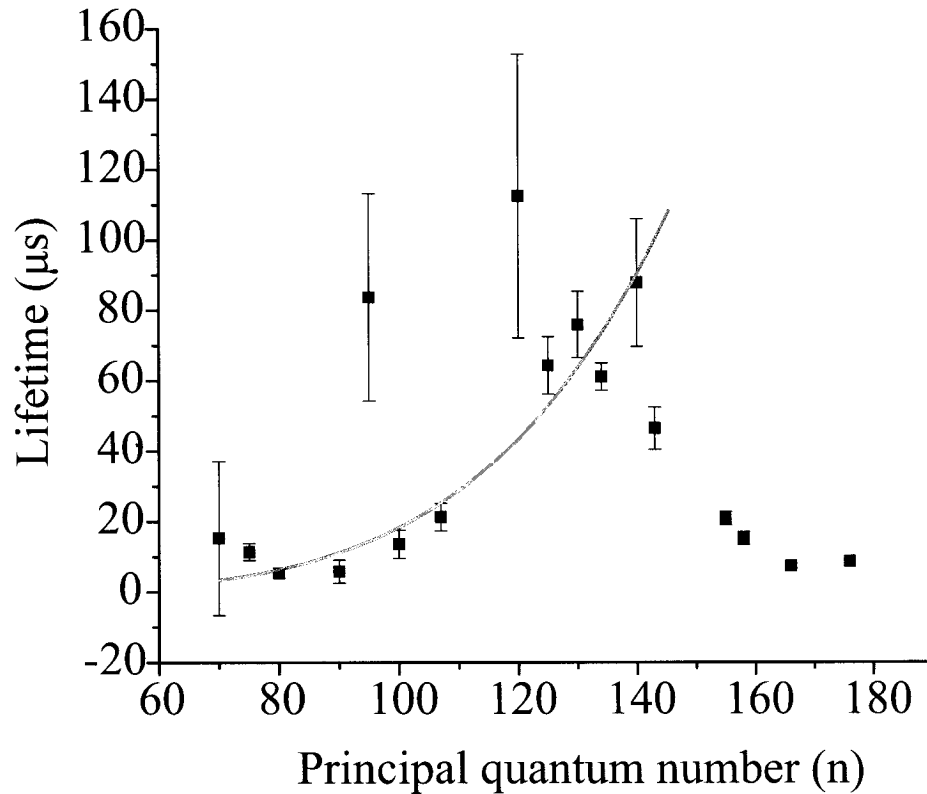
FIG. 60: The lifetime of the ZEKE states as a function of the principal quantum number (n).

be noted that apart from the effects of auto-ionization, the natural lifetime of low l states scales at n^3 while for the statistical mixture of lm states scales as $n^{4.5}$ [19].

The lifetime of the ZEKE states are plotted against the principal quantum number shown in Fig. 60. As a reminder by lifetime, we mean the survival lifetime of the states following excitation. Since these atoms can interact with each other, in for example a collision which destroys the state, the lifetime we measure is not necessarily the natural lifetime. Nonetheless, it is interesting to examine the scaling of our measured lifetimes, at least for part of the region we have explored. To do so, the function $y = ax^b$ was fitted onto the data for the upward slope from lower lying states. The point at $n = 120$ and $n = 95$ with the unusually large error bars was excluded from the fit.

The lifetime dependence obtained scales as the power of ~ 4.73 along with the uncertainity of ± 0.84 which interestingly is in good agreement with the theoretical
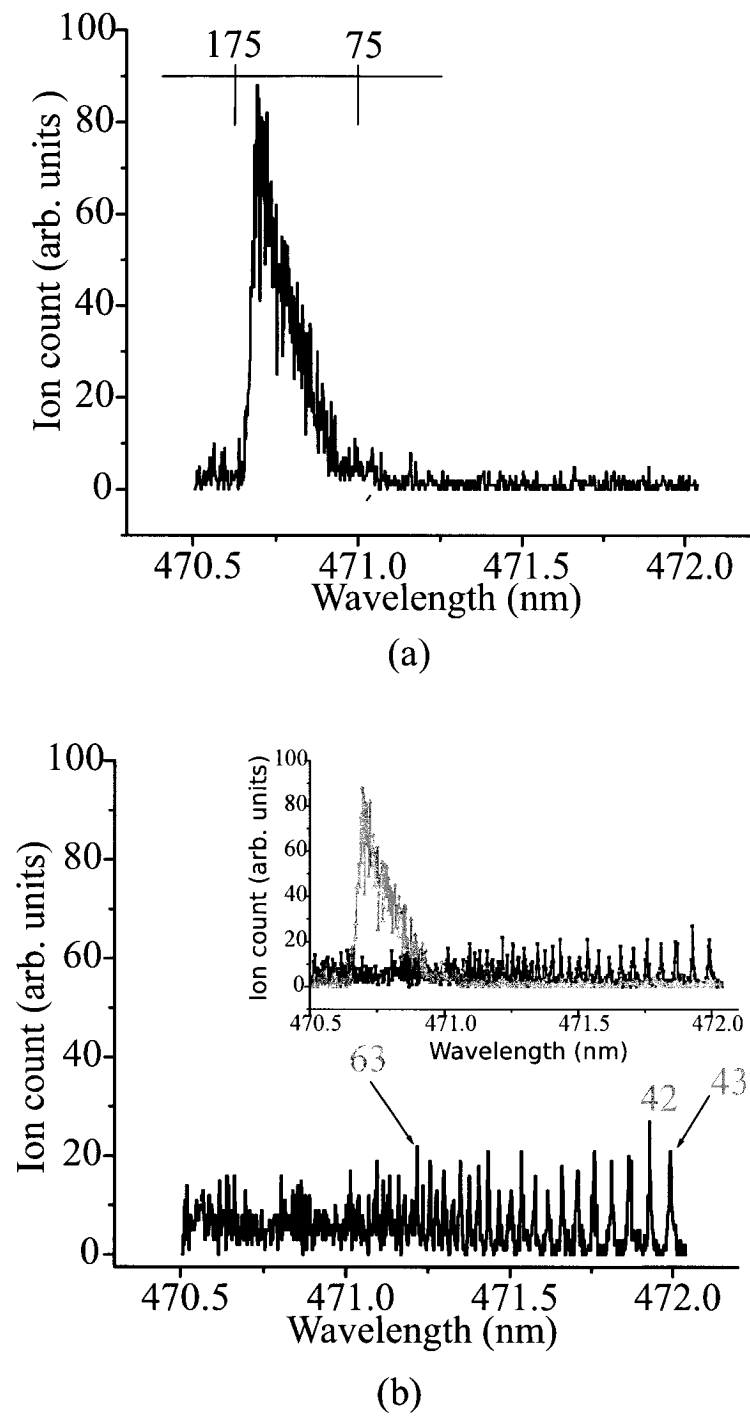
FIG. 61: (a) The general feature of ZEKE spectrum with the pulsed electric field and gate delays of 50 μs between the optical and electric field pulse within the gate width of of 40 μs, (b) the fast ions from auto-ionization and direct ions collected within the gate 40 μs wide and 1 μs delay from the optical pulse.

prediction for the scaling of the natural lifetime of the high l, high m states. If we assume that the lifetime of high lm states close to the $^2P_{1/2}$ ionization threshold is similar to those measured for high lm states close to the $^2P_{3/2}$ threshold, then even conservative scaling arguments would suggest that the natural lifetime of the ZEKE states is several times greater than the lifetimes observed here [71, 72]. If the ZEKE Rydberg atoms were isolated from each other and their environment, we would expect the lifetime curve to continue to increase. It does not.

While there is still some uncertainty of what extent the lifetime for lower n ZEKE states is due to the natural lifetime and what component is due to interactions, the reduction in the survival lifetime of higher n ZEKE states clearly demonstrates that there is an interaction of the ZEKE Rydberg atoms with other atoms or fields which is destroying the ZEKE states. There are several simple mechanisms which would explain the destruction of these states including field ionization from stray electric fields and collisions with other nearby ZEKE state Rydberg atoms. It is important to remember that these atoms are very large with classical orbit size scaling as n^2.

IV.2.9 Mapping the ZEKE state formation region

Another way to explore the production and survival of ZEKE Rydberg states is to fix the time delay at which the pulsed field is applied to field ionize the ZEKE states and collect the ions, and scan the exciting laser. Here, the atomic transitions follow the same pattern of $3p^5(^2P_{3/2})\, 4s\, ^2[3/2]_2 \longrightarrow 3p^5(^2P_{1/2})\, 4p\, ^2[3/2]_2 \longrightarrow auto-$ $ionizingstates$. The wavelength of the second step laser is now scanned from 470.5 nm to 472.0 nm with the two gates of width 40 μs set at the delays of 1 μs and 50 μs respectively. The pulsed electric field has a delay of 50μs and the slew rate of 50.4 V/μs and amplitude of$-$62.8 V or 45.8 V/cm at the ionization region which is sufficient to ionize the extreme red stark states with the principal quantum $n \sim 60$ according to the relation $F = 1/9n^{*4}$. However, the classical critical field required for the ionization of the stanes with $n = 60$ is approximately 25.1 V/cm. The ions collected in the first gate at 1 μs delay is presented in Fig. 61(b). This is the ion contribution from the direct or rapid auto-ionization. These ions are collected naturally without the application of a pulsed electric field. The ion signal in the first gate appears for the high lying states as well and increases as we go to the low-lying states which are prone to the fast auto-ionization. The delayed ion signal in the second gate is obtained by the pulsed electric field. The onset of the ion

signal is at $n \sim 175$ and increases rapidly as the energy level decreases. It turns around and the ion signal starts to fall as the energy level further decreases after the turning point. The ion signal completely disappears after $n \sim 75$. The ions signals in the fast and delayed gates are superimposed as shown in the inset Fig. 61.b. The signal in the delayed gate provides the evidence of the occurrence of ZEKE or long lived states only in the small region below the ionization threshold. This is in complete agreement with the findings of other groups who have investigated ZEKE state production in both atoms and molecules (though not in the ultracold regime). We expect the cutoff is at least partially explained by the changing timescale for auto-ionization, but future studies will be required to fully understand the dynamics resulting in the cutoff in production of ultracold ZEKE states around this value of n.

IV.3 ADDITIONAL ZEKE-STATE STUDIES

IV.3.1 ZEKE signal as a function of slew-rate

There are a number of effects which will require further investigation to fully understand the ultracold ZEKE Rydberg state system. One of these is the effect of the field ionization pulse on the ensemble of ZEKE state atoms. In a preliminary experiment in this direction, we have looked at the ion signal when simple tailored electric field pulses are applied. We began by looking at ion signal as a function of field ionization slew rate.

In this experiment, atoms in the magneto optical trap are photo-ionized via a two step, two-color, two photon transition as in the previous experiments with the same intermediate state. The MOT and Zeeman slower beams follow the same timing scheme as in the previous experiment. The field ionization or extraction pulse is applied at the delay time of 56 μs from photoionization. A fast operational amplifier (OPA-453 TA) is triggered with the continuous ramp generated by an arbitrary function generator (SRS DS-345) such that the maximum amplitude at the output of the amplifier is -62.8 V. The slew rate is set to 20 μs and 80 μs respectively. The output signal at the collector is sent to the multichannel scaler. The multichannel scaler is triggered at 180 μs after the flashlamp from Nd-YAG laser. Since the pulse field for ionization is delayed after the collection of the fast ions represented by 'D' in the Fig. 62. The pulsed field ionizes and accelerates atoms between the two rings.

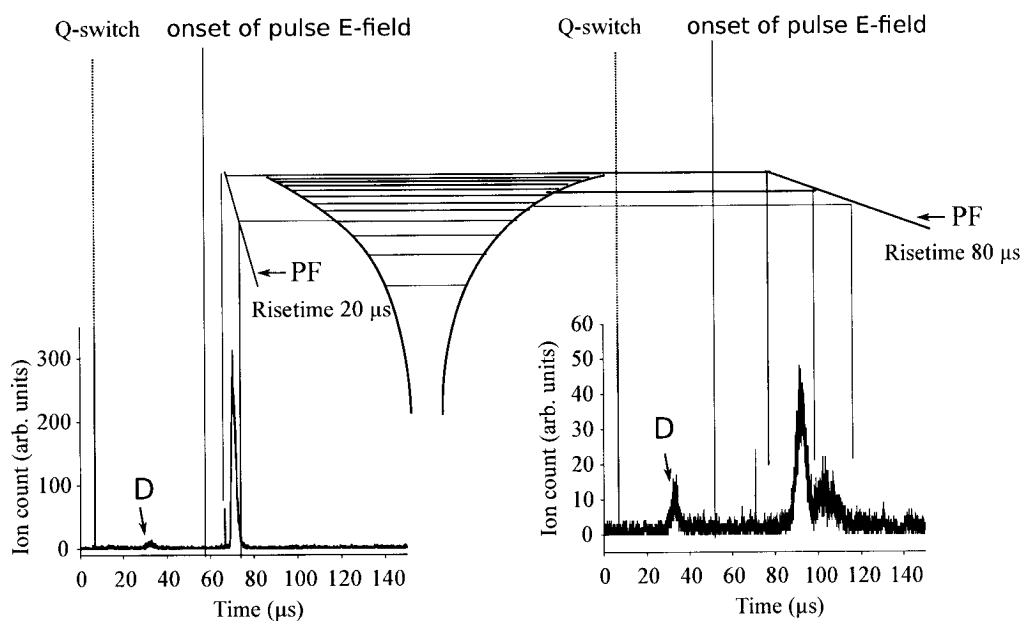FIG. 62: The ion detection for two different slew rates with a rise time of 20 μs and 80 μs depicted on left and right of the Coulombic potential respectively. D denotes the ions collected at the detector due to rapid auto-ionization. The onset of the pulsed field is shown however the field is shifted since there is certain $\sim$ 6 μs of delay between the pulsed field and the signal acquisition.

The acceleration stops after atoms enter the region between the ring and the mesh in front of the channeltron. The slow ramping field ensures that ions created at earlier times do not overtake ions created at later times on their way to the detector.

The second step laser is set to excite the atoms to a highly excited auto-ionizing state principal quantum number of $n = 100$ located below the second ionization threshold. The model of the pulsed field ionization is shown in the Fig. 62. The onset of pulsed field is shifted to make the concept clear since there is the delay between the application of the field pulse and the signal acquisition. The time resolved differences between two slew rates can be directly compared. For fast slew rate, the atoms within the big slice of the energy levels are ionized and accelerated and are all collected within the small time gate. However, for the slow slew rate different slices of the energy levels are ionized and accelerated successively. In this case the ion signal is spread and different peaks start to appear. This technique can be used to probe the Rydberg level distribution as the possible mechanisms for the apperance of the later peak are likely the distribution of the atoms among the different Rydberg states following the ZEKE-ZEKE Rydberg atoms collisions and the mixing of the different states in the presence of the field.

IV.3.2 Application of a "step" electric field pulse

We have also performed a preliminary investigation on the modification of the lifetime of the ZEKE-states using specially tailored electric field pulsed steps. In this experiment, after photo-excitation to various high lying ZEKE Rydberg states or to a region above ionization, a 9-step pulsed field with varying maximum value is applied and the ion signal is monitored in the multichannel scaler, triggered at 180 μs after the flashlamp of the Nd-YAG laser. The resulting ion signal is shown in Fig. 63.

The ions due to the later part of the pulsed field are absent both in the cases of a low lying state $n = 25$ and above ionization. However, a collection of significant peaks appear correlated to the steps of the pulsed field indicating the presence of the ZEKE-states. Despite the fact that the field required for the ionization of the state corresponding to $n = 96$ is approximately 7 V/cm, the ion signal appears at each rising steps. This either implies low ionization and collection of the ZEKE states in the previous field step or that the atoms redistribute themselves to the low lying states or non ionizing states during the steps of the pulsed field. This effect of
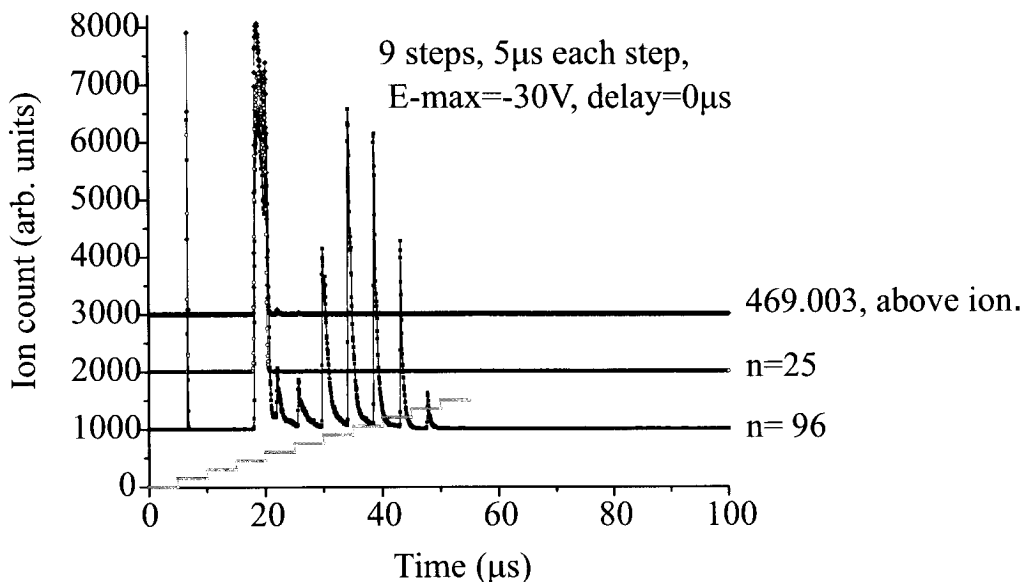
FIG. 63: Ion detection with a 9-step pulsed electric field with amplitude of -30 V; each step size is 5 μs. The ion signals are added with different offsets for a clear view.

redistribution whereby a set of ion peaks appears even when a series of identical pulses is applied has been observed in related work [73], but there the electric field returned to zero between pulses. In the following experiment, the Rydberg photo-excitation follows the same scheme of $3p^5(^2P_{3/2})\ 4s\ ^2[3/2]_2 \longrightarrow 3p^5(^2P_{1/2})\ 4p\ ^2[3/2]_2 \longrightarrow auto-ionizingstates$ with $n = 98$, which requires the classical field for ionization of a low l state equal to ~ 7 V/cm. The 9-step pulse is without delay after the photo-excitation with each step 5 μs long. The successive ion counts increases with the increase in the step size as shown in Fig. 64 (a) and (b). As the ionization and extraction pulsed electric field is increased further the pattern of ion collection is obtained which reaches a maximum for a certain field strength in the range of $18 - 25$ V/cm corresponding to $\sim 25 - 30$ V on the rings and mesh in front of the channeltron while the ring on the other side is grounded.

While it would be appealing to explain the results in terms of redistribution of the states during each step, it is important to realize that the Inglis-Teller limit, where the neighboring electronic quantum states intersect scales as $F = 1/3n^5$ and is equal to 0.192 V/cm for this n which is much less than the field strength even after the first step. Further careful investigation is necessary to explain these results,

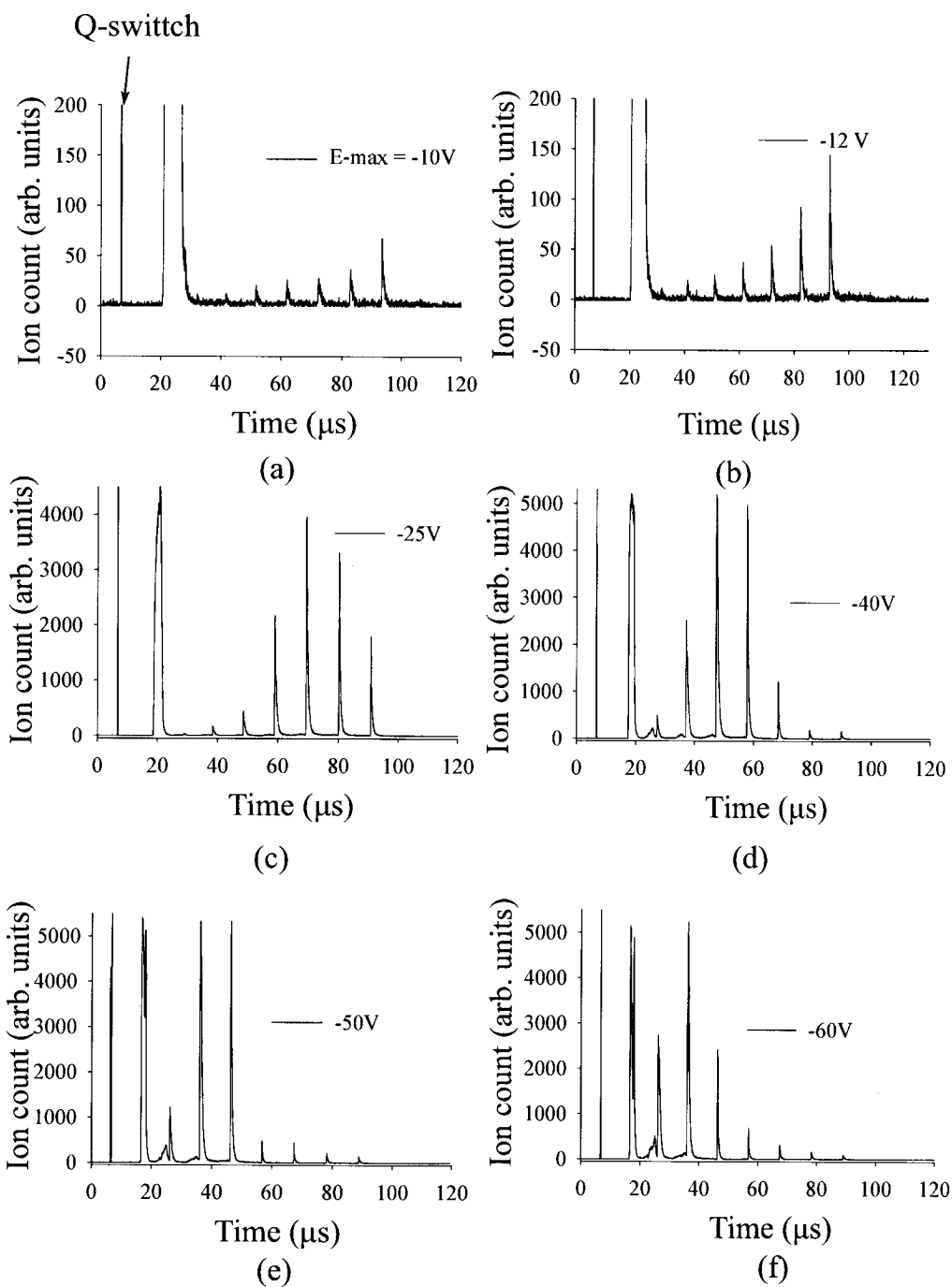FIG. 64: Ion detection with a 10-step pulsed electric field with the amplitudes of −10 V, −12 V, −25 V, −40 V, −50 V and −60 V, respectively from top left and bottom right; each step size is 5 μs.
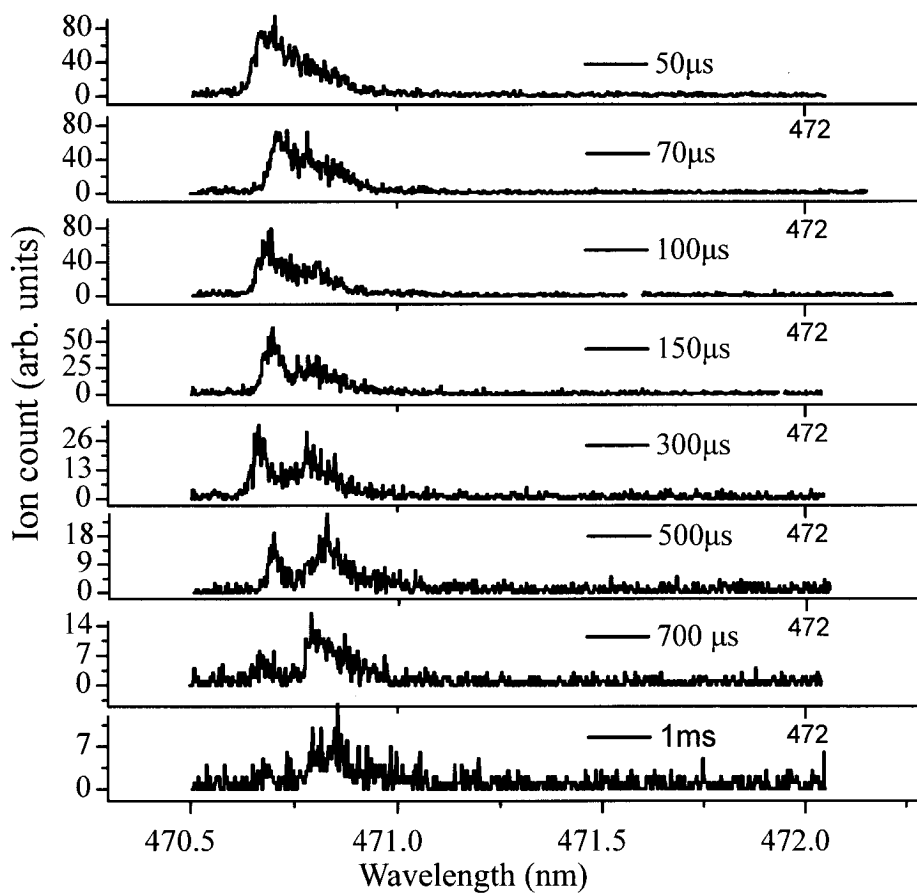
FIG. 65: ZEKE-ion spectrum in the different pulsed field and collection gate delays.
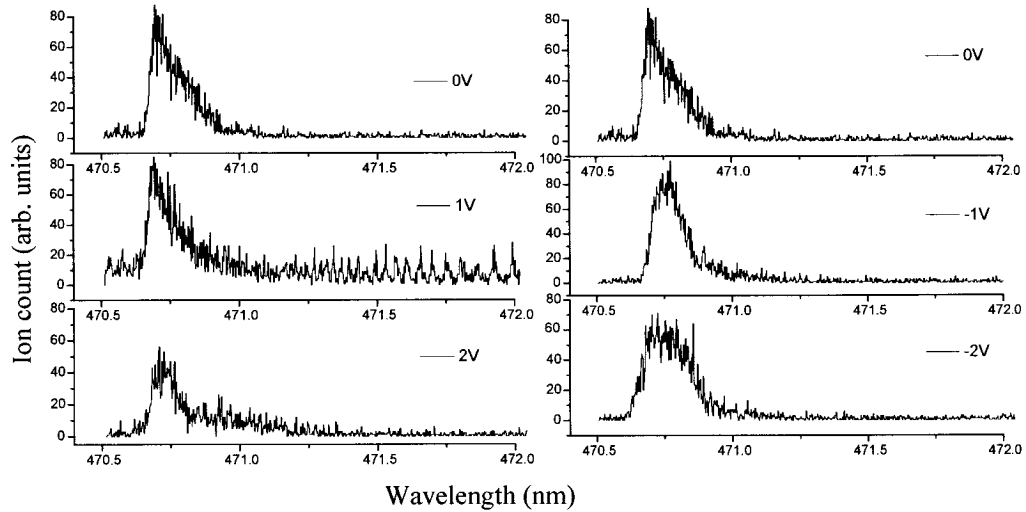
FIG. 66: The ZEKE-ion spectrum with different bias field put on the ring of the channeltron while the ring on the other side is grounded. The pulsed field and the collection gate have delays of 50 μs.

including better characterization of the ion collection during the later part of the step pulses.

Finally, in a set of experiments again similar to the one described above, we have used the same atomic excitation to ionizing levels below the second ionization threshold via a two-color, two-photon path. As a reminder, the first step laser wavelength is fixed for the excitation of the atom from the metastable state of $3p^5(^2P_{3/2})\ 4s\ ^2[3/2]_2$ to the intermediate state of $3p^5(^2P_{1/2})\ 4p\ ^2[3/2]_2$ and the second step laser is scanned slowly across the second ionization limit. The electric pulsed field with a slew rate of -58.34 V/μs and an amplitude of -62.8 V on the ring is applied after various delays from 50 μs, 70 μs, 100 μs, 150 μs, 300 μs, 500 μs, 700 μs and 1 ms respectively as seen from top to bottom of the plot in Fig. 65. The gate delay is synchronous with the pulsed field delays and the gate width is 40 μs. In the plot the overall ion collection decreases with an increase in the delays of the pulsed field and the gate which is obvious as the ions reach the detector before the gate opens. Hence, they are not collected. There appears a dip for a long delays between 100 μs and 1 ms. This is likely understood as a convolution of the formation of the ZEKE-states and the survivial of the ZEKE-states, both of which depend diffrently on n.

IV.3.3 ZEKE state formation vs. bias field

Finally, the ZEKE spectrum is obtained using the the same scheme of two-color, two-photon excitation. The pulsed electric field and collection window have the delays of 50 μs and the collection gate has the width of 50 μs. The atoms are excited in the presence of the different bias fields in order to investigate the formation and the survival of the ZEKE states when excited in the field. Results are displayed in Fig. 66.

IV.3.4 Discussion of ZEKE-state destruction

As we discussed in Chapter II, the dynamics of ultracold plasmas and Rydberg gases are very rich, with different, sometimes competing processes resulting from multiple interactions determining the time evolution of the system. In this ultracold ZEKE Rydberg state system, we have the added complexity that the Rydberg atoms reside in an auto-ionizing continuum and are only stabilized because of their high angular momentum character. Recall that the core-electron interaction for low l is diluted by the presence of the uniform dc electric field which is further diluted due to m-mixing as a result of the moving electrons during the laser pulse. While electric fields have been shown in some experiments to stabilize ZEKE states, they are capable of destruction of ZEKE-states as well. In fact, for high n states, the appearance of a very modest electric field is all that is needed to cause field ionization. Another likely mechanism for the destruction of ZEKE-states is collision-induced as the size of the ZEKE-state is relatively large (and the radius of Rydberg electron cloud scales as n^2 for large l) and these atoms can interact via van der Waals and dipole-dipole interactions. But other mechanisms exist as well including BBR-ionization and, for lower n, as we have discussed, radiative decay. However, radiative decay follows the electric dipole selection rules of $\Delta l = \pm 1$ and $\Delta m = 0$ or ± 1 so it takes a long time to decay below the ZEKE-regime if the atoms are in both high l and m states

It is expected that the lifetime results we have obtained and presented in this chapter reflect a combination of the physical mechanisms noted above with the most dominant mechanism a function of the excitation level n. Future work on this system will be directed at precisely differentiating the actual physical mechanisms responsible for ZEKE state production and destruction from the potential ones we have elucidated here.

IV.4 FLUORESCENCE DETECTION

While we have focussed in this dissertation on using ions to probe Rydberg states, fluorescence spectroscopy can also be used for the determination of the energy levels of atoms. We have done this for ultracold rubidium atoms (^{85}Rb) in the MOT as shown in Fig. 69. In addition to the ability to map out structure, fluorescence measurements in general also provide for a real-time, minimally-invasive technique for probing of the different dynamics in the magneto-optical trap. In this spectroscopic experiment, the Rb atoms are first prepared in the MOT. Our setup is capable of cooling and trapping of ^{40}Ar, ^{84}Kr and ^{85}Rb. In this study, only the Rb was cooled and trapped. The Rb for the MOT is provided by a dispenser (SAES Getters) in the science chamber [60]. The Rb atoms are cooled and trapped at the intersection of six counter-propagating beams. The total power of the cooling and trapping beam used for experiment is about 9.76 mW. It includes $\sim 1\%$ of this power at the repumper frequency. Unlike ^{40}Ar, ^{85}Rb has non-zero nuclear spin $I = 5/2$ which contributes to the hyperfine structure of the ground state. About 1 out of 1000 transitions to the upper state ends up going to the $F = 3$ upper hyperfine level which can then decay to the lower hyperfine state of the ground state $5s\,^2S_{1/2}$, $F = 2$ which results in the atom being optically dark for the cooling and trapping laser beam. The repumper laser frequency excites the atom to the excited state $5p\,^2P_{3/2}^0$ where it can then decay to the upper hyperfine level of the ground state. Further details of experimental and optical setups are in [60].

A partial energy level digram showing those states used for cooling and trapping of ^{85}Rb is shown in Fig. 67(a). The experiment is triggered with the Flashlamp sync out our Nd-YAG laser, this we call time $t = 0$. The MOT and repumper beam is turned off for 200 μs, starting 180 μs after the trigger. This ensures all atoms initially in the excited state $^2P_{3/2}^0$ are in the ground state. The pulsed 780 nm beam (pulsed with an AOM) is focused into the MOT cloud and programmed to turn on after 182 μs for 5 μs to excite the atoms to the $5p\,^2P_{3/2}^0$. At 186 μs, the third harmonics of Nd-YAG laser pumps Coumarin-480 to produce the dye laser beam tunable around 480 nm. The dye laser has the linewidth of 0.1 cm^{-1}. This beam is aligned and sent inside the chamber through the focussing lens in front of the window.
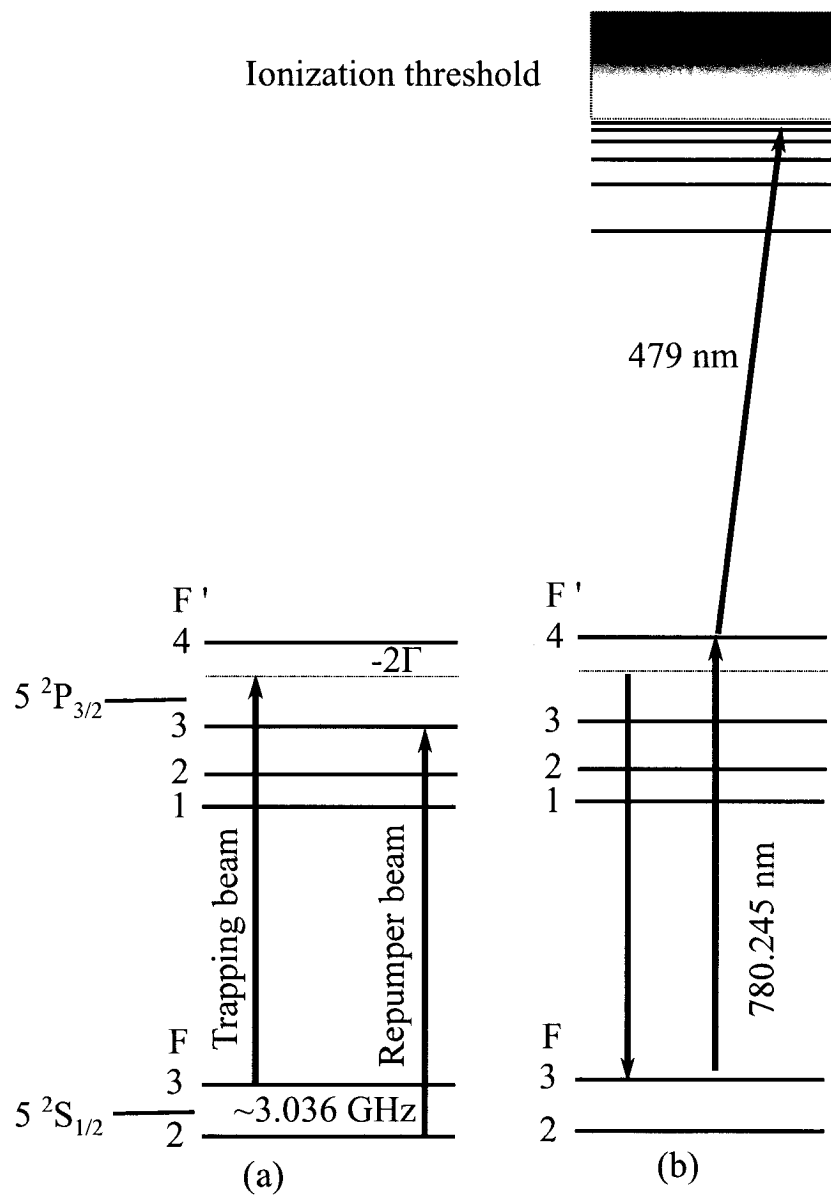
FIG. 67: (a) A partial energy levels used for the purpose of cooling and trapping of ^{85}Rb, (b) the atomic states during the experimental sequence corresponding the timing scheme.
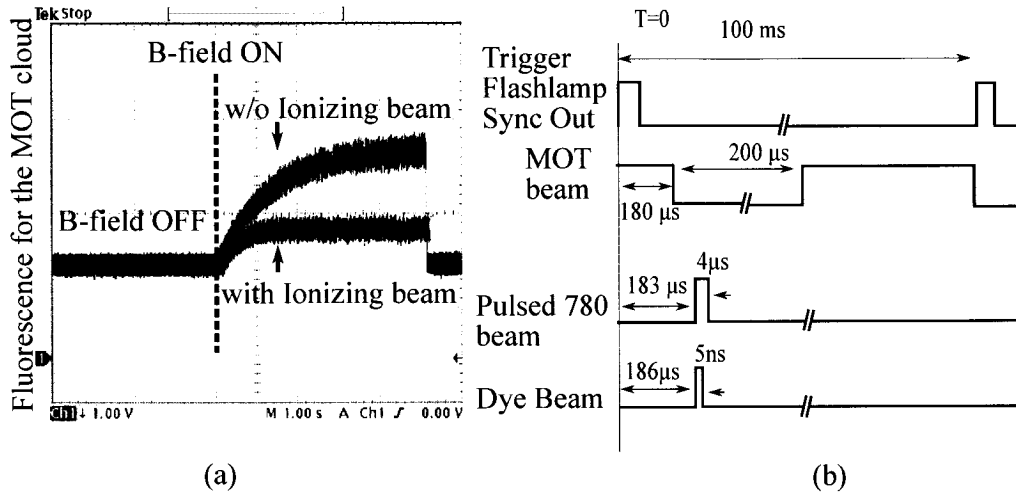
FIG. 68: (a) The loading curves for Rubidium atoms in the MOT in the absence and in the presence of the ionizing beam, (b) the timing sequence for the experiment.

IV.4.1 Fluorescence detection and trap loss spectroscopy

In this work, Rydberg atoms are detected by probing the fluorescence of the atomic cloud. A steady-state signal due to the continuous scattering of photons from the atomic cloud is registered by a photomultiplier tube (PMT), the output of which is fed to a two stage amplification via a fast pre-amplifier and connected to the input of our photon counter. The photon counter is carefully adjusted for the appropriate signal discrimination levels, and scan parameters like scans per record are set to 24.5 mV and 100 respectively. As the second step laser is scanned, the atom is excited to a Rydberg state whenever the second step laser is resonant. Before taking data both the timing sequence of the experiment and the alignment of the laser beams is adjusted by comparison of the loading curve of the MOT in the presence and in the absence of an ionizing laser beam as shown in Fig. 68.

For our atom number densities, to good approximation, the total number of atoms in the trap is proportional to the fluorescence from the atomic cloud detected with the PMT. The total number of photons scattered per sec is given by [74]

$$\eta = N_{atoms} \times R_{scat} \tag{177}$$

with R_{scat}, the scattering rate given by the relation

$$R_{scat} = \frac{\Gamma}{2} \frac{\frac{I}{I_s}}{1 + \frac{I}{I_s} + 2\left(\frac{\Delta}{\Gamma}\right)^2} \tag{178}$$

In the work reported here, the values are $I = 4.49$ mW/cm^2 for each incident beam while the total power is 9.75 mW and the beam waist is 0.96 cm, $\Delta = -2\Gamma$, $\Gamma \sim 6$ MHz and $I_s = 1.66$ mW/cm. The total intensity at the center or the chamber is ~ 26.94 mW/cm^2. The scattering rate becomes $R = 9.20 \times 10^6$ s^{-1}. The current registered by the PMT is given by

$$I = N_{photon} \times Q \times e \times G \tag{179}$$

with N_{photon} the number of photons entering the PMT, Q is quantum efficiency, e is electronic charge and G is the gain. The gain of the PMT is $\sim 10^5$. and the signal is read on digital oscilloscope with 1 MΩ input impedance.

$$N_{photon} = \frac{V}{Q \times e \times G \times 10^6} \tag{180}$$

The number of atoms in the atomic cloud is then

$$N_{atom} = \frac{V}{Q \times e \times G \times 10^6 \times 9.20 \times 10^6 \times \Omega_s} \tag{181}$$

where $\Omega_s = \pi r^2 / 4\pi R^2$ is the solid angle for photon collection, r is the radius of the effective region of the collection lens which can be considered to be 1.28 cm and R is the distance of the collection lens from the MOT which is ~ 16 cm. The number of atoms in the ^{85}Rb MOT is then roughly estimated to be $424592 \times V$.

We may also consider the effect of any incident probe on the excitation and ionization of the atoms. Photoionization of a neutral atom is a transition from a bound state $|i\rangle$ to the continuum state defined by the state vector $|f\rangle$ in the presence of the incident photon with the energy $E_{ph} \geq E_f - E_i$. The transition rate $\Gamma_{i \to f}$ is given by Fermi's Golden Rule:

$$\Gamma_{i \to f} = \frac{2\pi}{\hbar} \left| \langle f | \hat{H}_{if} | i \rangle \right|^2 \rho(E_i + E_{ph}) \tag{182}$$

The photoionization rate is proportional to the photoionization cross-section $\sigma(\omega_p)$. The photon flux is given by

$$\Phi_{ph} = \frac{I_p}{\hbar \omega_p} \tag{183}$$

where I_p an ω_p are the intensity and the frequency of the ionizing laser. The transition rate can be expressed as

$$\Gamma_{i \to f} = \sigma_p(\omega)\Phi_{ph} \tag{184}$$

The ionization fraction is given by

$$\frac{\eta_{ion}}{\eta_{Int}} = 1 - \exp(-\sigma\Phi_{ph}) \tag{185}$$

where η_{ion} and η_{Int} are the densities of ions and the doorway state respectively.

In the presence of the second step blue laser tuned above the ionization threshold of ^{85}Rb, ionization takes place. Since we are essentially making an ultracold plasma by doing this, recombination within the trap volume is also a possibility, though we neglect the process now for the simplicity. The additional loss contributes to total one-body loss. The fraction of atoms ionized from the trap in a single shot is quite small and the ionization occurs in the excited state or doorway state. Thus, the loss rate is given by,

$$\gamma_{ph} = \Gamma_{i \to f}\rho_{ee} \tag{186}$$

with ρ_{ee} is the excited state fraction.

The loading rate of the atoms in the MOT is governed by the rate equation

$$\frac{dN}{dt} = L - \alpha N - \beta_{Rb} \int_v n dv - \beta_{Rb-Rb} \int_v n^2 dv - \gamma_{ph} f N \tag{187}$$

where α, β_{Rb}, β_{Rb-Rb} and γ_{ph} are the trap loss rate coefficients and f is the duty cycle of the ionizing beam. The loading process of the Rb-MOT is documented in Fig. 68(a). The measurement has been performed here with and without the photoionizing 480 nm beam under otherwise identical conditions.

After the optimization of the timing scheme and alignment for the maximum number of atoms in the MOT in the absence of the ionizing beam and minimum number atoms in the presence of ionizing beam, the second step laser is scanned slowly in the range from 478.6 nm to 482 nm. The second step laser is scanned to yield the spectrum shown in the Fig. 69. A small amount of light is reflected from a beam splitter in the path of the laser beam and sent it to a high accuracy 621 series Bristol Instruments wavemeter for the continuous monitoring of the wavelength with an accuracy of the order of ± 0.0001 nm. The resonance peaks observed are in good agreement with the Rydberg atomic states outlined in NIST atomic spectra database.
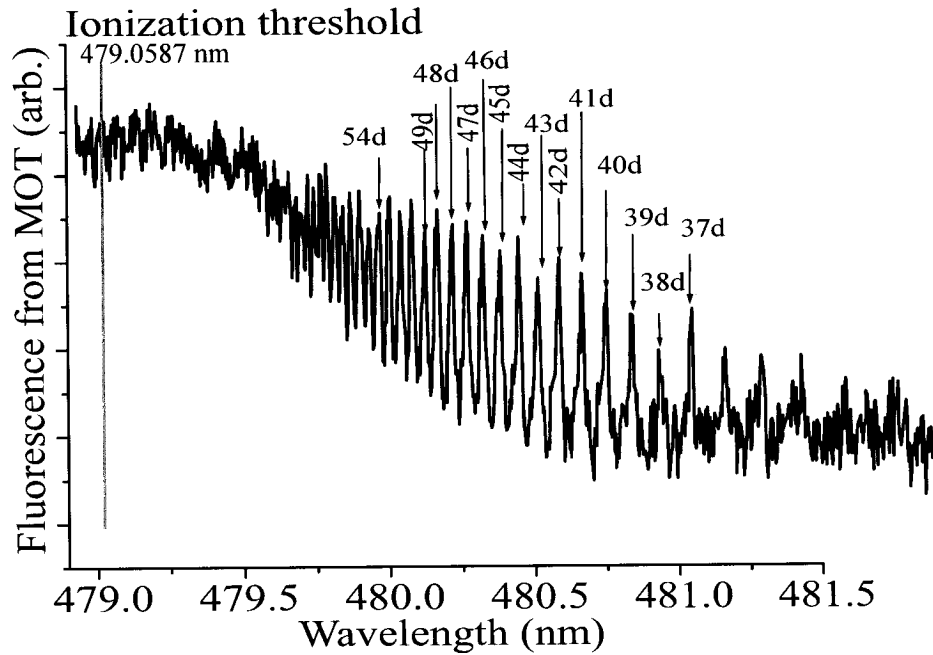
FIG. 69: (a) A partial ^{85}Rb Rydberg spectrum obtained via photo-detection with photo-multiplier tube (PMT).

IV.4.2 Results and discussion

The spectrum is obtained as a result of the trap loss due to the absorption of the second step laser and excitation to the highly excited states which do not contribute to the scattering of 780 nm photons from the MOT cloud. Some of these Rydberg excitations also result in ionization. This gives rise to an additional channel of the trap loss. An atom excited to a Rydberg level can be ionized by one of the following mechanisms:

$$A^* + B \rightarrow A^+ + e^- + B$$
$$A^* + A \rightarrow A^+ + A^-$$
$$A^* + A \rightarrow (A_2)^+ + e^- \tag{188}$$
$$A^* + A^* \rightarrow A + A^+ + e^-$$
$$A^* + A^* \rightarrow (A_2)^+ + e^-$$
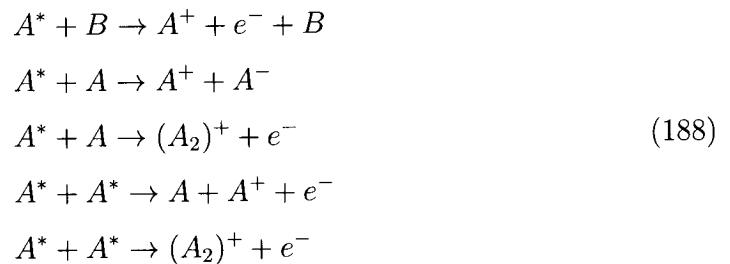
The last two mechanisms of ionization can be neglected in our case since the cross-section of Rydberg-Rydberg collisions is negligible here. However, the excited atom

can decay back to the ground state and be recaptured in the MOT. But, it is obvious that the fraction of recapture is non-significant in the time scale of the experiment. Further study of recapture and the recombination in ^{85}Rb is already in progress in our lab.

IV.5 SUMMARY OF RESULTS

The main objective of the research was to investigate the time evolution dynamics of the long-lived ZEKE-states created by two-color, two-photon excitation in an ensemble of ultracold Ar* atoms in a magneto-optical trap. Argon is an inert gas and has two ionization thresholds ~ 1431 cm $^{-1}$ apart, corresponding to the two spin-orbit configurations of ionic cores. We have investigated the creation and survival of ZEKE Rydberg states by photo-excitation followed by pulsed field ionization and ion detection.

The size of the Rydberg atoms is macroscopic which contributes to the huge geometrical collision cross-section. This investigation arises out of an interest to understand how the ZEKE dynamics evolve in ultracold systems. Spectroscopy was performed as the first set of experiment for identifying Rydberg levels based on $P_{3/2}$ ionic core, lying below the first ionization threshold and the Rydberg levels based on $P_{1/2}$ lying below but close to the second ionization threshold. The different low lying "s" and "d" states are identified and compared with the data from other groups and found to be in excellent agreement. The spectrum was taken in the presence of known electric fields in order to demonstrate that Stark spectroscopy can be used to characterize the conditions in which ultracold atoms find themselves in our system. Such characterization is critical for understanding the dynamics of ZEKE state formation and survival.

The existence and formation of ZEKE-states are confirmed and the time dependence of the survival of the ZEKE states are investigated which we found to have an interesting scaling law of $\sim n^{4.5}$ for the lower n side of the ZEKE region. On the higher n side of the ZEKE region, the lifetime was observed to rapidly decrease with n. We have also presented data on several preliminary experiments which use tailored electric fields to interrogate the ensemble of ZEKE state atoms. These experiments are the first step in a program to use shaped electric field pulses to control ZEKE states and thereby control ultracold plasma dynamics.

CHAPTER V

CONCLUSION AND PROSPECTS FOR THE FUTURE

This dissertation presents our study of long-lived ZEKE Rydberg states in an ultracold atomic cloud when atoms are excited to energy levels which reside in an auto-ionizing continuum. These states occur within a "magical" region just below the second ionization threshold in argon. The creation of such states can be understood as arising from collisions or from optical excitation of atoms in the presence of inhomegeneous fields. Such fields occur at the beginning of a photo-exciting laser pulse as a result of charged particles resulting from auto-ionization of low-l optically accessible states. The resulting lm mixing gives rise to the creation of high lm states which have little interaction with the core, suppressing auto-ionization.

We found that within the ZEKE state region, the survival lifetime first increased with principal quantum number n similar to a $n^{4.5}$ scaling, then began to decrease above n~130, likely due to collisions and field ionization from stray fields. Different survival times illustrate the different dynamical interactions that the Rydberg electron undergoes with the ionic core and the varied role of collisions.

As for the future, the next generation of experiments will employ several improvements and new techniques to better understand the various underlying physical mechanisms during the creation and time evolution of the ZEKE states. The present study uses two rings supported on four rods in front of the detectors which produce nonuniform fields at the interaction region. The applied electric field can be made uniform in the interaction region using the fine mesh. In this experiment the magnetic field hasn't been nulled, which might influence the production and destruction of the ZEKE-states. We have ignored the magnetic field in this study although its presence might exhibit some interesting effects on the evolution behavior. In the next generation experiment the effects of the magnetic fields will be studied. The slew rate of the electric field pulse seems to have an impact on the signal we detect as seen in Fig. 62. The experiments can be performed with the different slew rates in order to better understand this effect and for better resolution of the states in the ZEKE-region. We studied the dynamics with the collection of ions. However, the detection of the electron instead of ions can provide more accurate measurement with a greater efficiency as electrons are lighter than the ions and can be collected with small fields with much smaller delays between the pulse electric field and the

collection of electrons. Other interesting research will include study of the underlying physics of the redistribution and randomization of the states during the application of the step pulsed fields.

Since this work is very much related to ultracold plasma research, future experiments will move in that direction. Atoms can be excited just above the second ionization threshold and a study of the evolution dynamics of the plasma will be exciting as there is the additional phenomena of auto-ionization of low-l recombined states and the formation of ZEKE-states following three-body recombination. Of note is the liberation of additional energy as compared to conventional ultracold plasmas because of the auto-ionizing continuum. Finally, the control of ZEKE-states with programmed pulsed electric fields should prove very interesting in controlling ultracold plasma dynamics.

BIBLIOGRAPHY

[1] M. Mitsunaga, T. Mukai, K. Watanabe, and T. Mukai. *Dressed-atom spectroscopy of cold Cs atoms.* *JOSA*, **13**(12):2696, (1996).

[2] M. H. Anderson, J. R. Ensher, M. R. Matthews, C. E. Wieman, and E. Cornell. *Observation of Bose-Einstein condensation in a dilute atomic vapor.* *Science (Washington)*, **269**(5221):198, (1995).

[3] S. Chu. Nobel Lecture: *The manipulation of neutral particles.* *Rev. Mod. Phys.*, **70**(3):685, (1998).

[4] T. W. Hansen and A. L. Schawlow. *Cooling of gases by laser radiation.* *Opt. Comm.*, **13**:68, (1975).

[5] V.S. Letokhov, V. G. Minogin, and B. D. Pavlik. *Cooling and trapping of atoms and molecules by resonant laser field.* *Opt. Comm.*, **19**(1), (1976).

[6] A. L. Migdall, J. V. Prodan, W. D. Phillips, T. H. Bergeman, and H. J. Metcalf. *First Observation of Magnetically Trapped Neutral Atoms.* *Phys. Rev. Lett.*, **54**(24):2596, (1985).

[7] S. Chu, L. Hollberg, J. E. Bjorkholm, A. Cable, and A. Ashkin. *Three-dimensional viscous confinement and cooling of atoms by resonance radiation pressure.* *Phys. Rev. Lett.*, **55**(1):48, (1985).

[8] A. Ashkin and J. P. Gordon. *Stability of radiation-pressure particle traps: an optical Earnshaw theorem.* *Opt. Lett.*, **8**(10):511, (1983).

[9] K. B. Davis, M. O. Mewes, M. R. Andrews, N. J. Van Druten, D. S. Durfee, D. M. Kurn, and W. Ketterle. *Bose-Einstein condensation in a gas of sodium atoms.* *Phys. Rev. Lett.*, **75**(22):3969, (1995).

[10] T. C. Killian, S. Kulin, S. D. Bergeson, L. A. Orozco, C. Orzel, and S. L Rolston. *Creation of an Ultracold Neutral Plasma.* *Phys. Rev. Lett.*, **83**(23):4776, (1999).

[11] T. Pohl, T. Pattard, and J. M. Rost. *Influence of electron–ion collisions on Coulomb crystallization of ultracold neutral plasmas.* *J. Phys. B: At. Mol. Opt. Phys.*, **38**(2):S343, (2005).

[12] M. S. Murillo. *Using Fermi statistics to create strongly coupled ion plasmas in atom traps.* Phys. Rev. Lett., **87**(11):115003, (2001).

[13] S. Kulin, T. C. Killian, S. D. Bergeson, and S. L. Rolston. *Plasma oscillations and expansion of an ultracold neutral plasma.* Phys. Rev. Lett., **85**(2):318, (2000).

[14] T. C. Killian, M. J. Lim, S. Kulin, R. Dumke, S. D. Bergeson, and S. L. Rolston. *Formation of Rydberg atoms in an expanding ultracold neutral plasma.* Phys. Rev. Lett., **86**(17):3759, (2001).

[15] R. S. Fletcher, X. L. Zhang, and S. L. Rolston. *Using three-body recombination to extract electron temperatures of ultracold plasmas.* Phys. Rev. Lett., **99**(14):145001, (2007).

[16] F. Robicheaux and J. D. Hanson. *Simulation of the expansion of an ultracold neutral plasma.* Phys. Rev. Lett., **88**(5):55002, (2002).

[17] M. P Robinson, B. L. Tolra, M. W. Noel, T. F. Gallagher, and P. Pillet. *Spontaneous evolution of Rydberg atoms into an ultracold plasma.* Phys. Rev. Lett., **85**(21):4466, (2000).

[18] T. F. Gallagher, P. Pillet, M. P. Robinson, B. Laburthe-Tolra, and M.W. Noel. *Back and forth between Rydberg atoms and ultracold plasmas.* JOSA, **20**(5):1091, (2003).

[19] T. F. Gallaghar. *Rydberg Atoms.* Cambridge University Press, Cambridge, (1994).

[20] M. D. Lukin, M. Fleischhauer, R. Cote, L. M. Duan, D. Jaksch, J. I. Cirac, and P. Zoller. *Dipole blockade and quantum information processing in mesoscopic atomic ensembles.* Phys. Rev. Lett., **87**(3):37901, (2001).

[21] A. Gaetan, Y. Miroshnychenko, T. Wilk, A. Chotia, M. Viteau, D. Comparat, P. Pillet, A. Browaeys, and P. Grangier. *Observation of collective excitation of two individual atoms in the Rydberg blockade regime.* Nat. Phys., **5**:115, (2009).

[22] E. Urban, T. A. Johnson, T. Henage, L. Isenhower, D. D. Yavuz, T. G. Walker, and M. Saffman. *Observation of Rydberg blockade between two atoms.* Nature Physics, **5**(2):110, (2009).

[23] A. Walz-Flannigan, J. R. Guest, J. H. Choi, and G. Raithel. *Cold-Rydberg-gas dynamics. Phys. Rev. A*, **69**(6):63405, (2004).

[24] W. Chupka. *Factors affecting lifetimes and resolution of Rydberg states observed in zero-electron-kinetic-energy spectroscopy. J. Chem. Phys.*, **98**:4520, (1993).

[25] H. J. Dietrich, K. Müller-Dethlefs, and L. Ya. Baranov. *Fractional Stark state selective electric field ionization of very high-n Rydberg states of molecules. Phys. Rev. Lett.*, **76**(19):3530, (1996).

[26] R. Signorell, H. Palm, and F. Merkt. *Structure of the ammonium radical from a rotationally resolved photoelectron spectrum. J. Chem. Phys.*, **106**:6523, (1997).

[27] E. W. Schlag. *ZEKE spectroscopy*. Cambridge University Press, Cambridge, (1998).

[28] K. Müller-Dethlefs, M. Sander, and E. W. Schlag. *Two-colour photoionization resonance spectroscopy of NO: Complete separation of rotational levels of NO+ at the ionization threshold. Chem. Phys. Lett.*, **112**(4):291, (1984).

[29] C. Cohen-Tannudji, J. Dupont-Roc, and G. Arynberg. *Atom-Photon Interactions: Basic processes and applications*. John Wiley & Sons, New York, (1992).

[30] H. J. Metcalf and P. Van der Straten. *Laser cooling and Trapping : Graduate Texts in Contemporary Physics*. Springer, New York, (1999).

[31] C. Cohen-Tannoudji. *Atoms in electromagnetic fields*, volume **3** of *World Scientific Series on Atomic, Molecular and Optical Physics*. World Scientific Publishing, Singapore, (2004).

[32] C. J. Foot. *Atomic Physics*. Oxford Master Series in Atomic, Optical and Laser Physics. Oxford University Press, New York, (2005).

[33] D. E. Pritchard, E. L. Raab, V. Bagnato, C. E. Wieman, and R. N. Watts. *Light traps using spontaneous forces. Phys. Rev. Lett.*, **57**(3):310, (1986).

[34] E. L. Raab, M. Prentiss, A. Cable, S. Chu, and D. E. Pritchard. *Trapping of neutral sodium atoms with radiation pressure. Phys. Rev. Lett.*, **59**(23):2631, (1987).

[35] Thomas Jefferson Laboratory. The periodic table, 2010. http://education.jlab.org/itselemental/index.html.

[36] G. Racah. *Theory of Comples Spectra II. Phys. Rev.*, **62**:438, (1942).

[37] R. D. Cowan. *The theory of atomic structure and spectra.* University of California Press, California, (1981).

[38] W. N Hartley. *On Homologous Spectra. J. Chem. Soc*, **43**:390, (1883).

[39] C. E. Burkhardt and J. L. Jacob. *Topics in atomic physics.* Springer Science Business Media, Inc., New York, (2006).

[40] A. Dalgarno. *In Rydberg states of atoms and molecules.* Cambridge University Press, Cambridge, (1983).

[41] R. R. Freeman and D. Kleppner. *Core polarization and quantum defects in high-angular-momentum states of alkali atoms. Phys. Rev. A*, **14**:1614, (1976).

[42] H. A. Bethe and E. Salpeter. *Quantum mechanics of One and Two Electron Atoms.* Academic Press, New York, (1967).

[43] M. G. Littman, M. M. Kash, and D. Kleppner. *Field-ionization processes in excited atoms. Phys. Rev. Lett.*, **41**(2):103, (1978).

[44] D. Kleppner, M. G. Littman, and M. L. Zimmerman. *Rydberg states of atoms and molecules, Stennings and Dunning.* Cambridge University Press, Cambridge, (1983).

[45] E. Schrödinger. *An Undulatory Theory of the Mechanics of Atoms and Molecules. Phys. Rev.*, **28**:1049, (1926).

[46] P. Epistein. *The Stark Effect from the Point of View of Schröedinger's Quantum Theory. Phys. Rev.*, **28**:965, (1926).

[47] S. Doi, Y. Ishida, and S. Hiyama. *Sci. Papers Inst. Phys. Chem. Res.*, **9**:1, (1928).

[48] Y. C. Chem, C. E. Simien, Laha S., P. Gupta, Y. N. Martinez, P. G Mickelson, S. B. Nagel, and T. C. Killian. *Electron screening and kinetic energy oscillations inn a strongly coupled plasma. Phys. Rev. Lett.*, **93**(265003), (2004).

[49] Y. C. Chen, P. Gupta, S. Laha, Y. N. Martiniz, P. G. Mickelson, S. B. Nagel, A. D. Saenz, and C. E. Simien. *Ultracold Neutral Plasmas. Plasma Phys. Control. Fusion*, **47**(A297), (2005).

[50] A. Held, U. Aigner, L. Ya. Baranov, H. L. Selzle, and E. W. Schlag. *Lifetime control in Rydberg states. An application to the autoionizing series below the P1/2 ionization limit of xenon. Chem. Phys. Lett.*, **299**, (1999).

[51] K. R. Jennings. *Fundamentals and applications of gas phase ion chemistry.* kluwer Academic Publishers, Netherlands, (1999).

[52] E. Rabani, L. Ya. Baranov, R. D. Levine, and U. Even. *Dynamics of high molecular Rydberg states in the presence of a weak dc field. Chem. Phys. Lett.*, **221**:473, (1994).

[53] M. L. Zimmerman, M. G. Littman, M. M. Kash, and D. Kleppner. *Stark structure of the Rydberg states of alkali-metal atoms. Phys. Rev. A*, **20**(6):2251, (1979).

[54] T. F. Jyes. PhD thesis, Rice University, USA, (1982).

[55] F. Merkt. *Molecules in high Rydberg states. Annu. Rev. Phys. Chem.*, **48**:675, (1997).

[56] F. Remacle, R. D. Levine, E. W. Schlag, H. L. Selzle, and A. Held. *Electric Field Effects on Long Living ZEKE States. J. Phys. Chem.*, **100**:15320, (1996).

[57] H. C. Busch. *Experimental Investigation of A Rubidium-Argon Dual Species Magneto-Optical Trap.* PhD thesis, Old Dominion University, USA, (2004).

[58] J. G. C. Tempelaars. *Trapping Metastable Neon Atoms.* PhD thesis, University of Amsterdam, Netherlands, (2001).

[59] K. B. MacAdam, A. Steinbach, and C. E. Wieman. *A narrow-band tunable diode laser system with grating feedback, and a saturated absorption spectrometer for Cs and Rb. Phys. Rev. Lett.*, **54**:735, (1985).

[60] M. K. Shaffer. *Photoassociative Spectroscopy of Ultracold metastable Argon and Study of Dual Species Trap Loss in a Rubidium metastable Argon MOT.* PhD thesis, Old Dominion University, USA, (2008).

[61] P. P. Sorokin and J. R. Lankard. *Stimulated emission observed from an organic dye, chloro-aluminum phthalocyanine. IBM Journal of Research and Development*, **10**(2):162, (1966).

[62] F. P. Schafer, W. Schmidt, and J. Volze. *Organic dye solution laser. App. Phys. Lett.*, **9**(8):306, (1966).

[63] M. L. Spaeth and D. P Bortfeld. *Stimulated emission from polymethine dyes. App. Phys. Lett.*, **9**:179, (1966).

[64] P. Gupta. *Pulsed Dye Laser For Excitation of Strontium.* MS thesis, Rice University, USA, (2004).

[65] A. G. Shenstone. *Ultra-ionization potentials in mercury vapor. Phys. Rev.*, **38**(5):873, (1931).

[66] H. E. White. *Auto-Ionization in the Noble Gases and Alkaline Earths. Phys. Rev.*, **38**(9):1786, (1931).

[67] G. Racah. *On a new type of vector coupling in complex spectra. Phys. Rev.*, **61**(7-8):537, (1942).

[68] N. K. Piracha. *Two-Photon Laser Optogalvanic Studies of Helium, Neon and Argon.* PhD thesis, Quaid-i-Azam University, Pakistan, (1997).

[69] M. Aslam. *Two-step Laser Excitation Spectra of Neon, Argon and Krypton.* PhD thesis, Quaid-i-Azam University, Pakistan, (2000).

[70] S. K. Dutta, D. Feldbaum, A. Walz-Flannigan, J. R. Guest, and G. Raithel. *High-angular-momentum states in cold Rydberg gases. Phys. Rev. Lett.*, **86**(18):3993, (2001).

[71] E. Vliegen, H. J. Wörner, T. P. Softley, and F. Merkt. *Nonhydrogenic effects in the deceleration of Rydberg atoms in inhomogeneous electric fields. Phys. Rev. Lett.*, **92**(3):33005, (2004).

[72] E. Vliegen and F. Merkt. *On the electrostatic deceleration of argon atoms in high Rydberg states by time-dependent inhomogeneous electric fields. JOSA*, **38**:1623, (2005).

[73] F. Merkt, R. J. Rednall, S. R. Mackenzie, and T. P. Softley. *Electric field ionization of high Rydberg states of Ar with sequences of identical pulses. Phys. Rev. Lett.*, **76**(19):3526, (1996).

[74] M. Minarni. *Investigation of ultracold Rb atoms in a pulsed far off resonance trap.* PhD thesis, Old Dominion University, USA, 2006.
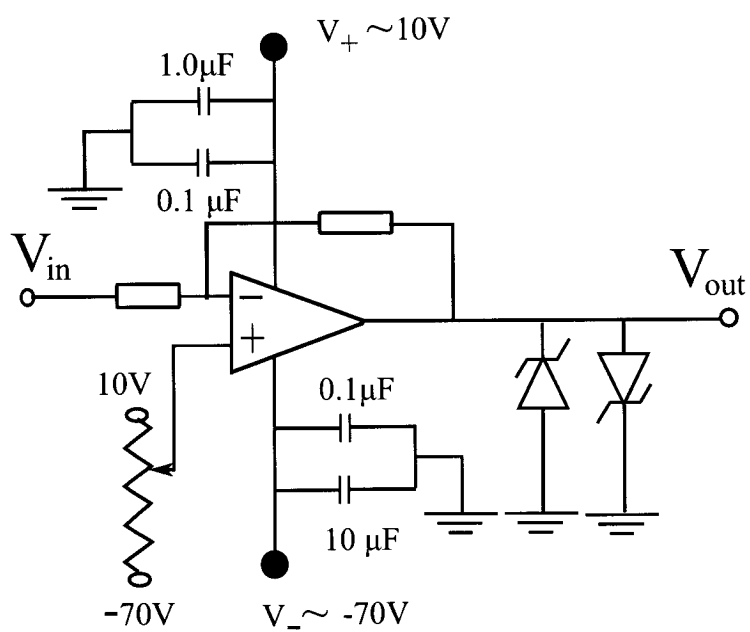
APPENDIX A

FIELD PULSER FOR IONIZATION

FIG. 70: A circuit used for the fast amplification of the pulse field using an OPA453 TA chip.
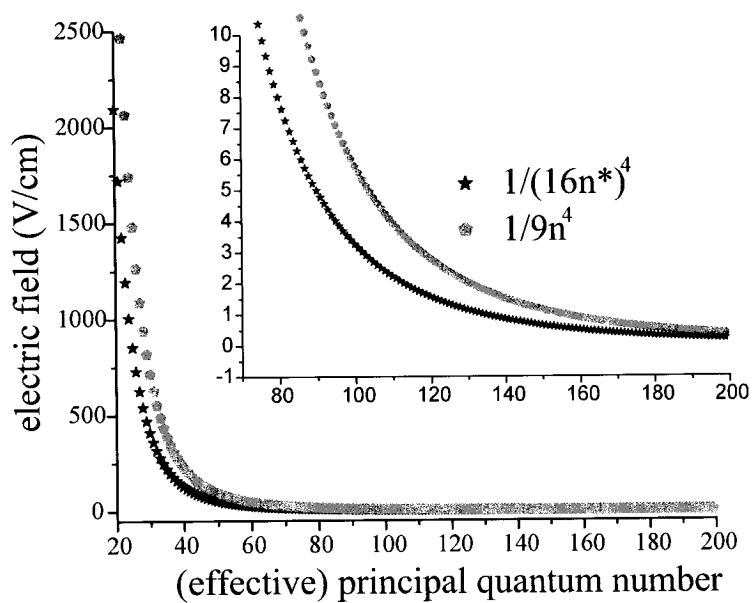
FIG. 71: Classical field required for ionization of d-levels in Argon and the field required for the extreme red-state to ionize.
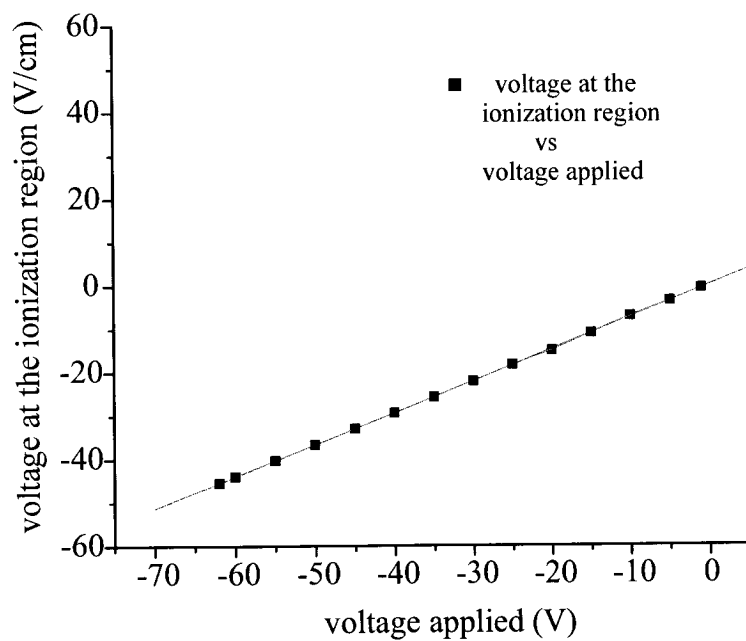

FIG. 72: Electric field at the ionization region as a function of the applied field.

VITA

Gambhir Ranjit

Department of Physics

Old Dominion University

Norfolk, VA 23529

Education:

Ph.D. Physics, Old Dominion University, expected December 2010.

Dissertation Title: Experimental Investigation of Long-lived "ZEKE" Rydberg states in Ultracold Argon

Advisor: Dr. Charles I. Sukenik

M.S. Physics, Old Dominion University, May 2006.

M.Sc. Physics, Tribhuvan University, Nepal, 2000.

B.Sc. Tri-chandra College, Nepal, 1998, *(Physics, Mathematics, Meteorology)*

Work Experience:

Graduate Research Assistant (ODU), AMO Research, Summer 2005-present.

Teaching Assistant (ODU), Astronomy lab, Fall 2004-Summer 2005.

St. Mary's Higher Secondary School, Nepal, Physics Instructor and Lab Supervisor, Summer 2001–Summer 2003. *Courses Taught: Mechanics, Heat and Thermodynamics, Modern Physics.*

Publications:

"Extended tuning of an injection-locked diode laser", M. K. Shaffer, G. Ranjit, and C. I. Sukenik, Review of Scientific Instruments 79, 046102 (2008).

"Photoassociative spectroscopy of ultracold metastable argon," M. K. Shaffer, G. Ranjit, C. I. Sukenik, M. Walhout, in preparation.

"Investigation of Long-lived "ZEKE" Rydberg states in Ultracold Argon," G Ranjit and C. I. Sukenik, in preparation.

Typeset using LaTeX.